sciendo

Slovak natural zeolites as a suitable medium for antibiotics elimination from wastewater

Petra Szabová, Michaela Plekancová, Nikolas Gróf, Igor Bodík

Department of Environmental Engineering, Faculty of Chemical and Food Technology,
Slovak University of Technology, Radlinského 9, 812 37 Bratislava, Slovak Republic
petaszabova@gmail.com, igor.bodik@stuba.sk

Abstract: Pharmaceuticals are one of the most used compounds present in various environmental compartments. Due to their high consumption and possible unhealthy effect on ecosystems, pharmaceuticals have been identified as "emerging organic contaminants". Since these compounds have medium to high polarity, they end up in the water compartment after being used. This work deals with the sorption of three pharmaceutical substances from the therapeutic group of antibiotics. Specifically we have focused on Azithromycin, Clarithromycin and Erythromycin. Three fractions of the natural Slovak zeolites (200 μm, 0.5—1 mm and 1.5—2 mm) were used as the sorption medium. Experimental results have proven very effective sorption of antibiotics by zeolites. Azithromycin removal of over 99 % for all three zeolite fractions from wastewater treatment plant Stupava and wastewater treatment plant Devínska Nová Ves was achieved. Clarithromycin removal of 79 % for fraction 1—2.5 mm, 87.3 % for fraction 0.5—1 mm and of 99.8 % for fraction 200 μm from the effluent of wastewater treatment plant Stupava was observed. Erythromycin removal of 31.3 % for fraction 1—2.5 mm, 66.9 % for fraction 0.5—1mm and of 94.7 % for fraction 200 μm from effluent of wastewater treatment plant Stupava was measured. More than 95 % of Clarithromycin and Erythromycin were eliminated from the effluent of wastewater treatment plant Devínska Nová Ves. The highest elimination percentage was observed for the smallest zeolite fraction due to the highest specific surface area.

Keywords: antibiotics, pharmaceuticals, wastewater, zeolites.

Introduction

Intensive research on pharmaceuticals in the environment started about 25 years ago. Since then, a vast amount of literature has been published. The input and presence of active pharmaceutical ingredients and their fate in the environment have been of high interest (Kümmerer, 2009). The release of antibiotics is becoming of considerable concern due to their negative effects not only on the environment but also on human health (Lu et al., 2014). Antibiotics are antimicrobial agents of different chemical structures characterized by selective toxicity to certain types of bacteria. Antibiotics as pharmaceuticals are among the most prescribed medicines by general practitioners not only in Slovakia but also in the world. In the US, 262.5 million antibiotic packs (842 prescriptions per 1 000 persons) were prescribed in 2011. In 2016, Slovak doctors prescribe 718 packs antibiotic per 1 000 inhabitants (Šušková, 2017).

Erythromycin is an antibiotic used for the treatment of some bacterial infections. Azithromycin is used for the treatment of a number of bacterial infections for example: ear infections, strep throat, pneumonia, diarrhea, and certain other intestinal infections (Sylvester et al., 2009). Clarithromycin is used to treat various bacterial infections as: pneumonia, skin infections, Helicobacter pylori infection, and Lyme disease; it can be taken by mouth as a pill or liquid (Sylvester et al., 2009).

Many studies confirm that pharmaceuticals appeared in high concentration in wastewater treatment plants (WWTPs) worldwide. Concentration of clarithromycin in the influent of WWTPs is from 330 to 600 ng/l and in the effluent of WWTPs it ranges from 150 to 460 ng/l (Göbel et al., 2005). Erythromycin in WWTPs influent ranges between 140—10 020 ng/l and in WWTPs effluent between 23—2 700 ng/l (Kasprzyk-Hordern, Dinsdale and Guwy, 2009). Azithromycin in WWTPs influent ranges from 90 to 380 ng/l and in the effluent from 40 to 380 ng/l (Göbel et al., 2005).

The adsorption technology in a real WWTP is designed according to (Keysers et al., 2015), after the settlement tank, two separate lines for ozonation and sorption are located; they can be operated as single lines or in sequence (ozonation with subsequent sorption). Regeneration of zeolites can be based on thermal treatment, where adsorbed molecules are volatilized and/or oxidized by heating. Alternatively, the solvent extraction of entrapped molecules is considered as another efficient technique. Other methods include photochemical, biological, vacuum, electrical/electrochemical, and supercritical fluid treatment, as well as microwave and ultrasound methods (Braschi et al., 2016).

The aim of this work was to eliminate selected antibiotics from effluent of wastewater treatment plants by means of sorption processes. For sorption tests, Slovak natural zeolites from Zeocem a.s. (Košice, Slovakia) were used.

Materials and methods

Laboratory sorption tests were realized with Slovak natural zeolites from Zeocem a.s. (Košice, Slovakia) and with effluents from two municipal WWTPs. In the effluent samples from WWTP Stupava and WWTP Devínska Nová Ves, a wide spectrum of pharmaceuticals from different therapeutic groups were analyzed. As antibiotics are the most prescribed pharmaceuticals in the Slovak Republic, three compounds for our research were selected: azithromycin (AZI), erythromycin (ERY) and clarithromycin (CLA).

Pharmaceuticals analysis

The samples were filtered through a 0.45 µm cellulose membrane filter. Before HPLC/MS/MS analysis, a mixture of isotopes labelled internal standards was added to 10 ml of the sample. For pharmaceutical products detection, SPE liquid chromatography combined with a hybrid quadrupole – Orbitrap, and a high resolution detector was used (Grabic et al., 2012). Table 1 summarizes basic information on the monitored antibiotics.

Characteristics of Slovak natural zeolites

Zeolites are natural or synthetic aluminosilicates of ordered arrangements of SiO_4 and AlO_4 tetrahedra. Isomorphic substitution of silicon (Si) by aluminum (Al) creates an overall negative charge which is compensated by cations, for example Na^+, K^+, Ca^{2+} and Mg^{2+}, providing zeolites with the properties of cationic exchangers. Natural zeolites and less pure forms of synthetic zeolites, such as those derived from fly ash, find limited applications in wastewater treatment, where high selectivity and specificity are not an issue. The general formula of a zeolite is $M_{e2/n}O \cdot Al_2O_3 \cdot xSiO_2 \cdot yH_2O$, where, M_e is any alkali or alkaline earth atom, n is the charge on that atom, x is the number of Si tetrahedron varying from 2 to 10, and y is the number of water molecules varying from 2 to 7 (Sun et al., 2017).

Extensive possibilities of zeolites are mainly due to their specific physicochemical properties:

- high ion exchange selectivity
- reversible hydration and dehydration
- high gas sorption capacity
- high thermostability
- resistance to aggressive media (Zeocem a.s., 2016)

Sorption tests were carried out with 10 g of three zeolite fractions (200 µm; 0.5–1 mm; 1–2.5 mm) and 200 ml of WWTPs effluent. Sorption time was

Tab. 2. Basic properties of tested zeolites (Zeocem a.s., 2016).

Fraction of zeolites		Specific surface area
200 µm	Powder	53–55 m^2/g
0.5–1 mm	Fine sand	44–46 m^2/g
1–2.5 mm	Coarse sand	40–42 m^2/g

Tab. 1. Basic characteristics of pharmaceuticals.

Pharmaceutical	Molecular weight (g/mol)	pKa	Charge at pH 7	Log Kow	References
azithromycin	784.99	$pKa_1 = 8.7$ $pKa_2 = 9.5$	Positive	0.44–3.16	Xian et al., 2015
clarithromycin	747.95	8.99	Positive	3.18; 3.16	Verlicchi et al., 2012a
erythromycin	737.93	8.88–8.9	Positive	2.5 3.06	Jones et al., 2002 Verlicchi et al., 2012a

Fig. 1. Zeolite fractions.

30 min. Subsequently, samples were taken and sent for drug analysis. Table 2 summarizes basic properties of the individual fractions.

Results and discussion

Since 2014, monitoring of pharmaceuticals in wastewater has been carried out at the Department of Environmental Engineering, Faculty of Chemical and Food Technology, Slovak University of Technology in Bratislava. In the first step, monitoring of selected antibiotics was carried out at 15 Slovak WWTPs. Table 3 summarizes average concentration of antibiotics in the individual stages of Slovak WWTPs. These data show that removal of antibiotics is very low; specifically, removal of ERY and AZI is only 32 % and 65 %, respectively. Although the removal of CLA is relatively high – 93 %, the total effluent concentration is very high (258 ng/l). Real effluent concentrations of all monitored antibiotics are higher than 200 ng/l, so adding a tertiary treatment step to eliminate these residual concentrations is strongly advised. Elimination of pharmaceuticals from water is very important as they negatively affect fish and other living organisms. Some studies indicate mutations in fish due to drug accumulation in water (Mimeault et al., 2005).

Wastewater treatment plant Stupava

In wastewater treatment plant Stupava, wastewater from 13 000 p.e. is treated but its capacity is up to 18 000 p.e. WWTP Stupava consists of a mechanical and a biological (pre-denitrification, nitrification) stage, and sludge is aerobically stabilized. Monitoring of the selected antibiotics shows that the drugs are present in the influent at hundreds of ng/l (Table 4) and their removal is not satisfying. Elimination of selected antibiotics is very high but effluent concentration is also high. For example, removal of CLA was 94 % but effluent concentration was 100 ng/l, which indicates the need to add a tertiary treatment step.

Tab. 4. Average concentration of pharmaceuticals in WWTP Stupava influents and effluents and their removal efficiency.

Pharmaceuticals	Influent ng/l	Effluent ng/l	Removal %
azithromycin	430	180	58
clarithromycin	1 700	100	94
erythromycin	390	63	84

Concentrations of AZI, CLA and ERY of 520 ng/l AZI, 2200 ng/l CLA and 16 ng/l ERY were detected in WWTP Stupava effluents. Table 5 summarizes data measured after the sorption test with individual zeolite fractions run for 30 minutes. AZI was effectively (over 99 %) removed by all three fractions. CLA was removed (79.1 %) using the largest zeolite fraction (1–2.5 mm), and the efficiency of the removal increased with the gradual reduction of the fraction. With the finest 200 µm fraction, CLA removal was above 99 %. The lowest elimination of the selected antibiotics was achieved for ERY, the elimination effect was 31 % with the largest fraction (1–2.5 mm), which is significantly lower than that for AZI and CLA. ERY was most effectively removed using the 200 µm fraction (94.7 %). The

Tab. 3. Average sewage concentration in individual WWTPS stages from long term monitoring during last 12 months.

Pharmaceuticals	Influent ng/l	Primary sedimentation tank ng/l	Removal after primary sedimentation tank %	Total effluent ng/l	Total removal of antibiotics %
azithromycin	598	387	35	208	65
clarithromycin	3 870	842	78	258	93
erythromycin	296	177	40	202	32

Tab. 5. Measured data from WWTP Stupava after 30 min of sorption tests.

Pharmaceuticals	Effluent ng/l	1–2.5 mm zeolite ng/l	Removal %	0.5–1 mm zeolite ng/l	Removal %	200 µm zeolite ng/l	Removal %
azithromycin	520	3.2	99.4	2.2	99.6	2.4	99.5
clarithromycin	2 200	460	79.1	280	87.3	4	99.8
erythromycin	16	11	31.3	5.3	66.9	0.85	94.7

results show that the highest sorption efficiency was achieved with the smallest zeolite fraction; which confirms the fact that smaller fraction of zeolites and larger specific surface provide better sorption.

Wastewater treatment plant Devínska Nová Ves (DNV)
This wastewater treatment plant currently treats 45 000 p.e. of wastewater, but its capacity is up to 76 000 p.e. WWTP DNV consists of a mechanical stage and a biological (nitrification, denitrification and bio-P elimination) stage, sludge is also anaerobically stabilized and generated biogas is energetically recovered. Monitoring showed that the selected antibiotics are present in the influent in hundreds of ng/l (Table 6). From the results it is evident that elimination of the selected antibiotics in WWTP Devínska Nová Ves is very low, for example average effluent concentration of CLA is 615 ng/l. The highest removal efficiency was observed for ERY (45 %), however, effluent concertation was 16 ng/l.

Tab. 6. Influents and effluents of WWTP Devínska Nová Ves and their removal during last 12 months.

Pharmaceuticals	Influent ng/l	Effluent ng/l	Removal %
azithromycin	780	610	22
clarithromycin	820	615	25
erythromycin	29	16	45

Subsequently, a second experiment was carried out to confirm the high removal of antibiotics with wastewater from WWTP Devínska Nová Ves. The observed substances were detected at concentrations of 300 ng/l of AZI, 440 ng/l of CLA and 37 ng/l of ERY. Table 7 summarizes concentrations of antibiotics in the WWTP effluents and concentrations after sorption on zeolites.

The second experiment confirmed the findings of the Stupava wastewater experiment. The removal of all drugs was above 90 %.

The removal efficiency of all monitored antibiotics was above 95 % for all zeolite fractions. More than 99 % of AZI were removed from both WWTPs with each of the three zeolite fractions. CLA concentration was fivefold lower in the effluent from WWTP Devínska Nová Ves than in that from WWTP Stupava. CLA removal in WWTP Devínska Nová Ves was 19 % higher for the zeolite fraction of 1—2.5 mm and 11 % for the 0.5—1 mm fraction compared to WWTP Stupava. For the ultra-fine-grained zeolite fraction, CLA elimination was comparable with the results from Stupava. The highest differences in the elimination of antibiotics were observed for ERY. From the WWTP Devínska Nová Ves effluent, 64 % more ERY were removed using zeolites than from the WWTP Stupava effluent (fraction 1—2.5 mm). This difference may be related to different wastewater composition as well as to different concentrations of other drugs that can preferably be sorbed onto the zeolites. This fact was also confirmed by the fraction 0.5—1 mm, where the difference in ERY elimination was 31 % between WWTP Devínska Nová Ves (97.5 %) and WWTP Stupava (66.9 %). The ultra-fine-grained zeolite fraction showed the highest ERY removal efficiency and was approximately the same for both effluents.

Oh et al. (2016) found that if pH < pKa, sorption is most effective, pH = pKa shows partial sorption and pH > pKa minimal sorption. The measured results confirm that pH of the WWTP Stupava effluent was 6.85 and all studied drugs have pKa of above 8 and a positive charged molecule at pH = 7 (see Table 1). All tested antibiotics have a positive charged molecule at pH = 7 while zeolites have a negative charged crystal grid (Frankovská et al., 2010); thus antibiotics and zeolites interact with each other, which promotes their sorption. Measured pH in the effluent of WWTP Devínska Nová Ves was 7.01, which meets the condition of good sorption at pH < pKa. Based on the results, zeolite sorption is an effective way of eliminating antibiotics from wastewater in a post-treatment step.

Conclusions

The work was focused on finding sorption properties of selected antibiotics. High concentrations of azithromycin, clarithromycin and erythromycin were found in the effluents from WWTP Stupava and WWTP Devínska Nová Ves. Three zeolite fractions with different specific surfaces were tested. These sorption tests showed their potential for

Tab. 7. Measured data from WWTP Devínska Nová Ves.

Pharmaceuticals	Effluent ng/l	1—2.5 mm zeolite ng/l	Removal %	0.5—1 mm zeolite ng/l	Removal %	200 µm zeolite ng/l	Removal %
azithromycin	300	0.89	99.7	0.62	99.8	0.92	99.6
clarithromycin	440	9.4	97.9	8.1	98.2	3.6	99.2
erythromycin	37	1.7	95.4	0.91	97.5	0.57	98.5

eliminating selected drugs from the wastewater treatment plant. The highest rate of antibiotic removal was observed using zeolites with the highest specific surface, i.e., the smallest fraction 200 μm (WWTP Stupava: AZI 99.5 %, CLA 99.8 % ERY 94.7 %, WWTP Devínska Nová Ves: AZI 99.6 %, CLA 99.2 % ERY 98.5 %). The results prove that zeolites can be used as sorption material for pharmaceuticals removal from wastewater; however, due to problematic handling of the finest dust fractions in real conditions, using the middle fraction of zeolites is recommended as their antibiotic removal efficiency is approximately the same.

Acknowledgement

This work was supported by the Slovak Research and Development Agency under the contract No APVV 0119-17. The authors thank the company Zeocem a.s. (Košice, Slovakia) for providing zeolite samples.

References

Braschi I et al. (2016) Physicochemical regeneration of high silica zeolite Y used to clean-up water polluted with sulfonamide antibiotics, Journal of Environmental Sciences. Elsevier, 43, pp. 302–312. doi: 10.1016/J.JES.2015.07.017.

Frankovská J et al. (2010) Atlas sanačných metód environmentálnych záťaží. Štátny geologický ústav Dionýza Štúra, Bratislava.

Göbel A et al. (2005) Extraction and determination of sulfonamides, macrolides, and trimethoprim in sewage sludge, Journal of Chromatography A. Elsevier, 1085(2), pp. 179–189. doi: 10.1016/J.CHROMA.2005.05.051.

Grabic R et al. (2012) Multi-residue method for trace level determination of pharmaceuticals in environmental samples using liquid chromatography coupled to triple quadrupole mass spectrometry, Talanta. Elsevier, 100, pp. 183–195. doi: 10.1016/J.TALANTA.2012.08.032.

Kasprzyk-Hordern B, Dinsdale RM and Guwy AJ (2009) The removal of pharmaceuticals, personal care products, endocrine disruptors and illicit drugs during wastewater treatment and its impact on the quality of receiving waters, Water Research. Pergamon, 43(2), pp. 363–380. doi: 10.1016/J.WATRES.2008.10.047.

Keysers CH, Grünebaum T, Thöle D, Pinnekamp J (2013) Removal of pharmaceuticals in municipal wastewater treatment plants, Proc. from the 8th IWA Specialist Conference on Assessment and Control of Micropollutants/Hazardous Substances in Water, Zurich, Switzerland.

Kümmerer K (2009) The presence of pharmaceuticals in the environment due to human use – present knowledge and future challenges, Journal of Environmental Management. Academic Press, 90(8), pp. 2354–2366. doi: 10.1016/J.JENVMAN.2009.01.023.

Lu X et al. (2014) Long-term effect of the antibiotic cefalexin on methane production during waste activated sludge anaerobic digestion, Bioresource Technology. Elsevier, 169, pp. 644–651. doi: 10.1016/J.BIORTECH.2014.07.056.

Mimeault C et al. (2005) The human lipid regulator, gemfibrozil bioconcentrates and reduces testosterone in the goldfish, Carassius auratus, Aquatic Toxicology. Elsevier, 73(1), pp. 44–54. doi: 10.1016/J.AQUATOX.2005.01.009.

Sun K et al. (2017) Sorption and retention of diclofenac on zeolite in the presence of cationic surfactant, Journal of Hazardous Materials. Elsevier B.V., 323, pp. 584–592. doi: 10.1016/j.jhazmat.2016.08.026.

Šušková T (2017) Takmer 4 milióny antibiotík. Available at: https://zivotbezantibiotik.sk/rok-2016-takmer-4-miliony-antibiotik (Accessed: 11 March 2019).

Sylvester RK et al. (2009) A hospice-based advanced pharmacy experience, American Journal of Pharmaceutical Education, 73(3), pp. 1–4. doi: 10.5688/aj730344.

Zeocem a.s. (2016) Čo je Zeolit – Klinoptilolit. Available at: https://www.zeocem.com/sk/zeolit (Accessed: 20 March 2019).

Quantum-chemical studies of rutile nanoparticles toxicity I. Defect-free rod-like model clusters

Martin Breza, Peter Šimon

Department of Physical Chemistry, Faculty of Chemical and Food Technology,
Slovak University of Technology, Radlinského 9, 812 37 Bratislava, Slovak Republic
martin.breza@stuba.sk

In the memory of Prof. Vojtech Kellö (1919–2007)

Abstract: Using the semiempirical PM6 method, structures of a rod-like $[Ti_{40}O_{124}H_{81}]^{7-}$ model cluster and of $[Ti_{40}O_{124}H_{81}Cu]^{5-}$ with Cu^{2+} coordinated at various sites were optimized in order to assess the toxicity of rutile nanoparticles. If the relative toxicity of individual Ti centers in rod-like rutile nanoparticles can be evaluated by the electron density transfer to a Cu^{2+} probe, its maximal values can be ascribed to the pentacoordinated corner and hexacoordinated edge Ti centers with three Ti—OH bonds. However, these centers exhibit the least negative interaction energies which can be compensated by the significantly better accessibility of the corner Ti center compared with that of the remaining ones. Ti centers with the most negative interaction energy parameters exhibit the lowest extent of electron density transfer to a Cu^{2+} probe. Rutile nanoparticles destruction starts at pentacoordinated Ti face centers.

Keywords: protonated rutile nanoparticle, PM6 semiempirical method, Cu(II) probe, electron density transfer, active centers

Introduction

Nano-sized TiO_2 particles can be found in a large number of foods, cosmetics and consumer products. Their nanotoxicity has drawn increasing attention because human body is potentially exposed to this nanomaterial either by inhalation, oral or dermal intake. Numerous studies have attempted to characterize their in vivo biodistribution, clearance and toxicological effects, especially in lungs, liver, kidneys, spleen, brain, lymph nodes, testis, blood and lungs of rats (see e.g. Olmedo et al., 2002; Wang et al., 2007; Fabian et al., 2008; Xie et al., 2011; Wang et al., 2011; Wang et al., 2013; Geraets et al., 2014; Elgrabli et al., 2015).

Rutile is the most stable polymorph of TiO_2 at all temperatures exhibiting lower total free energy than the metastable phases of anatase or brookite (Hanaor et al., 2012). Rutile has a tetragonal unit cell (space group P42/mnm) (Diebold, 2003) and its crystals are most commonly observed to exhibit a prismatic or acicular growth habit with preferential orientation along their c-axis, [001] direction. This growth habit is favored as the {110} facets of rutile exhibit the lowest surface free energy and are therefore thermodynamically the most stable ones (Hanaor et al, 2012a).

Interaction of water with TiO_2 is crucial in many of its practical applications. The rutile (110)-aqueous solution interface structure was measured (Zhang et al., 2007) in deionized water (DIW) at 25 °C by the X-ray crystal truncation rod method. Rutile surface consists of a stoichiometric (1 : 1) surface unit mesh with the surface terminated by bridging oxygen (BO) and terminal oxygen (TO) sites with a mixture of water molecules and hydroxyl groups (OH) occupying the TO sites. An additional hydration layer can be observed above the TO site, having three distinct water adsorption sites each in well-defined vertical and lateral locations. Structural displacements of atoms at the oxide surface are sensitive to the solution composition. Ti atom displacements from their bulk lattice positions, as large as 0.05 Å at the rutile (110)-DIW interface, decay in magnitude into a crystal with significant relaxations that are observable down to the fourth Ti-layer below the surface. A systematic outward shift was observed for Ti atom locations below the BO rows, while a systematic inward displacement was found for Ti atoms below the TO rows. The distance between the surface fivefold Ti atoms and the oxygen atoms of the TO site is 2.13 ± 0.03 Å in DIW, suggesting molecular adsorption of water at the TO site to the rutile (110) surface in DIW.

Very recently, scanning tunneling microscopy and surface X-ray diffraction have been used (Hussain et al., 2017) to determine the structure of the rutile (110)–aqueous interface which is comprised of an ordered array of hydroxyl molecules with molecular water in the second layer. A combination of data from real-space imaging, spectroscopic measurements and surface X-ray diffraction, with interpretation aided by DFT calculations, implies that the rutile TiO_2 (110) surface has terminal hydroxyls in the contact layer. The ideal coverage by terminal OH groups is half a monolayer, which is decreased to approximately 0.4 monolayers due to absences at domain wall boundaries.

According to Alagona and Ghio (Alagona and Ghio, 2009, 2009a), antioxidant activity of prenylated pterocarpans is related to their copper coordination ability. Based on B3LYP calculations of several complexes with Cu^{2+} of their low-energy conformers, their metal ion affinity (MIA) values have been determined. In aqueous solutions, the solvent effect dampens the free energy differences and reduces the MIA especially when the ion is extensively exposed to the solvent. Stability order of the species with metals bonded at various coordination sites strongly depends on their position and nature. Spin density of the cation upon ligand coordination becomes negligibly low, whereas the ligand spin density approaches 1. Thus, the ligand is oxidized to a radical cation (Ligand$^{\bullet+}$) while Cu(II) is reduced to Cu(I). In agreement with experimental investigations, the higher antioxidant activity of individual compounds and their reaction sites can be assigned to higher MIA values and higher reducing character toward Cu(II). Antioxidant ability of various sites of hyperjovinol A through their ability to coordinate a Cu^{2+} ion and reduce it to Cu^{+} was successfully tested by Mammino (Mammino, 2013). Another modification of the above-mentioned method has been used for both N centers of a series of para-phenylene diamine (PPD) antioxidants (Puškárová and Breza, 2016). Nearly linear dependence of the experimental antioxidant effectiveness on Cu(II)-PPD interaction energies, Cu atomic charges and other electron density parameters has been deduced.

From the chemical point of view, nanoparticles toxicity is also based on electron density transfer to human tissues. Therefore, the above-mentioned method, tested for antioxidants, might be suitable for the relative toxicity estimation of various sites of model nanoparticles. The liquids in human body are, in principle, aqueous solutions, which implies protonation of the negative charged surface of rutile nanoparticles. For the sake of simplicity, only hexacoordinated Ti atoms and full protonation of non-bridging O atoms are considered in model systems. Molecular mechanics methods are suitable for large model systems but reveal on their electron structure. DFT methods bring valuable information on electron distribution within the studied systems but their size is significantly restricted due to technical reasons. Semiempirical methods of quantum chemistry seem to be a suitable compromise between the above-mentioned ones. The aim of this study was to estimate the toxicity of various sites of an idealized protonated rod-like rutile nanoparticle (over 200 atoms) based on its Cu(II) complexation ability and electron density transfer to Cu at semiempirical PM6 level of theory.

Method

Geometries of the model systems under study were optimized using the PM6 method of quantum chemistry (Stewart, 2007). Stability of the optimized structures was confirmed by vibrational analysis (no imaginary vibrations). Atomic charges were evaluated in terms of the Mulliken population analysis (MPA) (Mulliken, 1955) and alternatively atomic polar tensor (APT) derived charges (Stephens et al., 1990). All calculations were performed using the Gaussian09 program package (Frisch et al., 2009).

Metal-ligand interaction energy $\Delta_{\text{int}}E$ is defined as

$$\Delta_{\text{int}}E = E_{\text{Complex}} - E_{\text{L}} - E_{\text{ion}} \tag{1}$$

where E_{Complex} and E_{L} are the energies of the $^{2}[\text{L}\cdots\text{Cu}]^{q+2}$ complex and of the isolated rutile nanoparticle $^{1}\text{L}^{q}$ model cluster in their optimized geometries, respectively, and E_{ion} is the energy of the isolated $^{2}Cu^{2+}$ ion (Alagona and Ghio, 2009, 2009a; Mammino, 2013). Left superscripts denote spin multiplicities. Analogously, metal-ligand interaction enthalpy $\Delta_{\text{int}}H_{298}$ and Gibbs free energy $\Delta_{\text{int}}G_{298}$ at 298 K data were also evaluated.

Deformation energy E_{def} is the difference (Alagona and Ghio, 2009, 2009a; Mammino, 2013) between the energy of the ligand L^{q} in its $^{2}[\text{L}\cdots\text{Cu}]^{q+2}$ complex geometry ($E_{\text{L(Cu)}}$) and that corresponding to its optimized structure (E_{L})

$$E_{\text{def}} = E_{\text{L(Cu)}} - E_{\text{L}} \tag{2}$$

Deformation energies should be lower than the corresponding metal-ligand ones.

Results and Discussion

Using experimental rutile structure (Swope et al., 1995), an idealized rod-like $[Ti_{40}O_{124}]^{88-}$ cluster (Fig. 1) of ca 1.5 nm × 1 nm × 1 nm size was formed. Its planes are parallel with the (110) plane of the rutile unit cell and all Ti atoms are hexacoordinated. As such a highly negative nanoparticle cannot exist in biological aqueous solutions, all monovalent O atoms were protonated to form a $[Ti_{40}O_{124}H_{81}]^{7-}$ cluster with geometry optimized

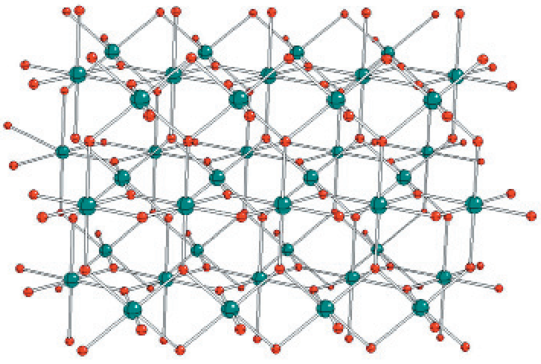

Fig. 1. $[Ti_{40}O_{124}]^{88-}$ cluster in experimental rutile geometry (Swope et al., 1995), (Ti — green, O — red).

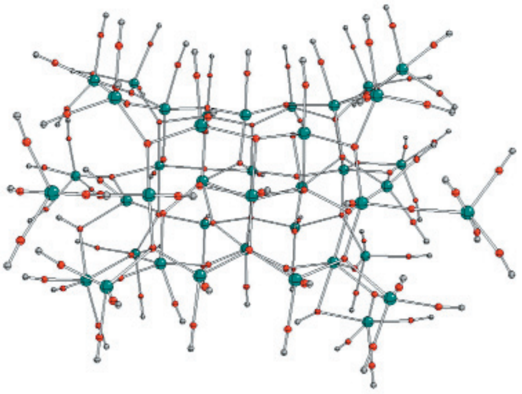

Fig. 2. PM6 optimized geometry of $[Ti_{40}O_{124}H_{81}]^{7-}$ cluster (Ti — green, O — red, H — grey).

in the singlet ground spin state (Fig. 2). It can be seen that its planes are significantly deformed due to protonation and the original Ti hexacoordination is sometimes reduced to pentacoordination. Several Ti centers can be distinguished according to their bonding to hydroxyl groups (OH) and bridging oxygens (O_b) between two Ti atoms. These centers can be divided into three groups as follows:

A. At the rod corners, only pentacoordinated $Ti(OH)_3(O_b)_2$ centers are found (model A, see Fig. 3)

B. Rod edges contain either hexacoordinated $Ti(OH)_3(O_b)_3$ (model B1, see Fig. 4), $Ti(OH)_2(O_b)_4$ (model B2, see Fig. 4) and $Ti(OH)(O_b)_5$ (model B3, see Fig. 4) centers or pentacoordinated $Ti(OH)_4(O_b)$ (model B4, see Fig. 5), $Ti(OH)_3(O_b)_2$ (model B5, see Fig. 5) and $Ti(OH)_2(O_b)_3$ (model B6, see Fig. 5) centers.

C. Rod faces have hexacoordinated $Ti(OH)(O_b)_5$ (model C1, see Fig. 6) or pentacoordinated $Ti(OH)(O_b)_4$ (model C2, see Fig. 6) centers.

In order to compare the reactivity of all the above-mentioned possible reaction sites, a Cu^{2+} ion was added at the distance of ca 1.9–2.3 Å from the hydroxyl groups of every center under study. Geometries of thus created $[Ti_{40}O_{124}H_{81}Cu]^{5-}$ clusters were again PM6 optimized in the ground doublet spin state. The resulting structures are depicted in Figs. 3–6. For the sake of simplicity, notation of the above reaction sites agrees with the $[Ti_{40}O_{124}H_{81}Cu]^{5-}$

Tab. 1. Copper(II)-ligand interaction energies ($\Delta_{int}E$), Gibbs free interaction energies ($\Delta_{int}G_{298}$) and interaction enthalpies ($\Delta_{int}H_{298}$) at 298 K, and deformation energies (E_{def}) of $^2[Ti_{40}O_{124}H_{81}Cu]^{5-}$ structures obtained by the PM6 method for the model systems under study (see Appendix).

Model	$\Delta_{int}E$ [kJ/mol]	$\Delta_{int}G_{298}$ [kJ/mol]	$\Delta_{int}H_{298}$ kJ/mol]	E_{def} [kJ/mol]
A	-3789.9	-3707.4	-3770.6	1212.9
B1	-3888.6	-3803.7	-3862.7	1196.2
B2	-4046.8	-3955.1	-4019.2	1312.5
B3	-4190.3	-4110.8	-4167.3	1397.9
B4	-4086.5	-3993.6	-4058.5	1353.9
B5	-4047.2	-3950.1	-4022.9	1331.3
B6	-3981.1	-3888.2	-3956.8	1392.4
C1	-4053.0	-3964.8	-4029.2	1438.0
C2	-4152.6	-4057.6	-4126.7	1392.4

Tab. 2. MPA ($q(Cu)_{MPA}$) and APT ($q(Cu)_{APT}$) copper atomic charges and lengths of Cu—O bond to hydroxyl ($d_{Cu—OH}$) and bridging ($d_{Cu—Ob}$) oxygen atoms of $^2[Ti_{40}O_{124}H_{81}Cu]^{5-}$ structures obtained by the PM6 method for the model systems under study.

Model	$q(Cu)_{MPA}$	$q(Cu)_{APT}$	$d_{Cu—OH}$ [Å][a)]	$d_{Cu—Ob}$ [Å]
A	0.586	0.669	2.009, 2.038, 2.048 (2.032)	–
B1	0.585	0.638	2.018, 2.034, 2.039 (2.030)	–
B2	0.633	0.721	2.068, 2.077, 2.086 (2.077)	–
B3	0.648	0.744	2.089, 2.124, 2.126, 2.184 (2.131)	–
B4	0.634	0.734	2.040, 2.058,2.062, 2.105 (2.066)	–
B5	0.648	0.721	2.126, 2.130, 2.138, 2.160, 2.193 (2.149)	–
B6	0.645	0.740	2.133, 2.139, 2.158, 2.198 (2.157)	2.107
C1	0.627	0.739	2.081, 2.120, 2.137, 2.152 (2.123)	2.146
C2	0.641	0.899	2.141, 2.177, 2.194, 2.256, 2.294 (2.212)	2.071

[a)] Average values in parentheses.

model system labels. Their selected characteristics are presented in Tables 1 and 2 and in Table 3 of Appendix.

Our results (Table 1) indicate that all copper(II)-ligand interaction energy parameters exhibit the same trends. Differences between various model systems are higher than those in the corresponding deformation energies. Thus, no corrections in the observed trends of the calculated interaction energy are necessary. As expected, corner Ti centers (model A) exhibited the least negative interaction energy parameters. The most negative values were observed for the hexacoordinated edge Ti centers with a single hydroxyl group (model B3). These are shifted to less negative values with the increasing number of hydroxyl groups in other hexacoodinated edge Ti centers (B2 and B1 models). Pentacoordinated edge Ti centers (B4, B5 and B6 models) exhibited reverse trends. Interaction energy parameters of hexacoordinated face Ti centers (C1 model) are comparable with the medians of the edge Ti centers. Their values for pentacoodinated face Ti centers (C2 model) are significantly more negative due to the removal of the $[\mathrm{Ti(OH)_5}]^-$ cluster from the nanoparticle by a Cu^{2+} probe, which indicates the most probable site of a nanoparticle destruction.

Table 2 contains charges of Cu probes indicating the extent of electron density transfer from the ligand (the higher Cu charge corresponds to the lower electron density transfer). The resulting Cu spin density is negligible in all the model systems under study and thus the corresponding data are not presented. Positive APT charges at Cu atoms are higher than the MPA ones and need not exhibit the same trends for pentacoordinated centers. In general, more negative interaction energy parameters (Table 1) are connected with higher Cu charges, however they are significantly affected by the number and type of Cu bonded oxygen atoms (OH or $\mathrm{O_b}$). Cu probes in A, B1 and B2 models are tricoordinated, in B3 and B4 models tetracoordinated and in the B5 one, they

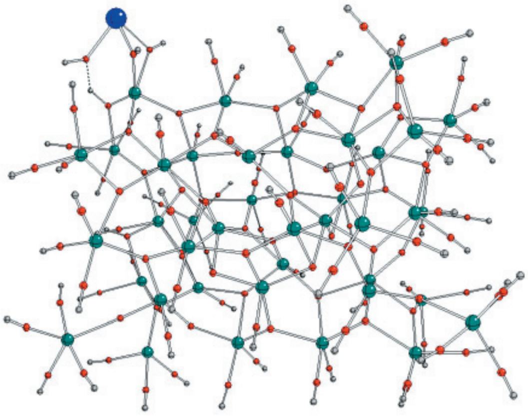

Fig. 3. PM6 optimized geometry of $[\mathrm{Ti_{40}O_{124}H_{81}Cu}]^{5-}$ cluster, model A (Ti – green, O – red, H – grey, Cu – blue).

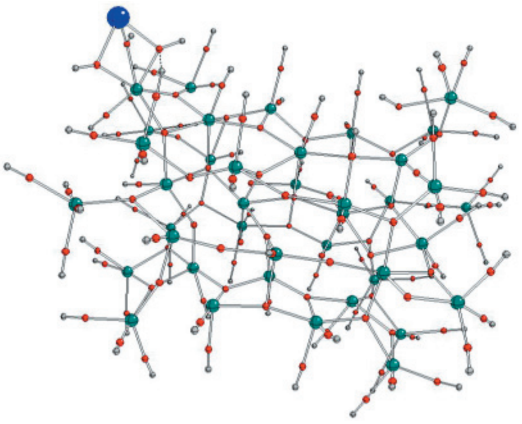

Model B1

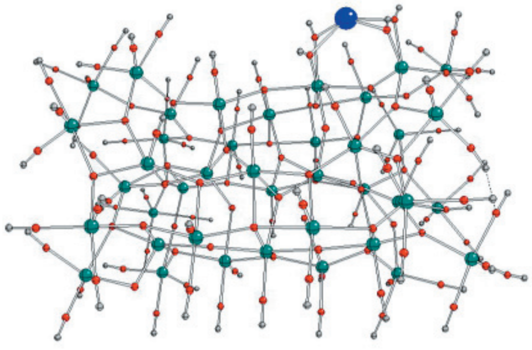

Model B2

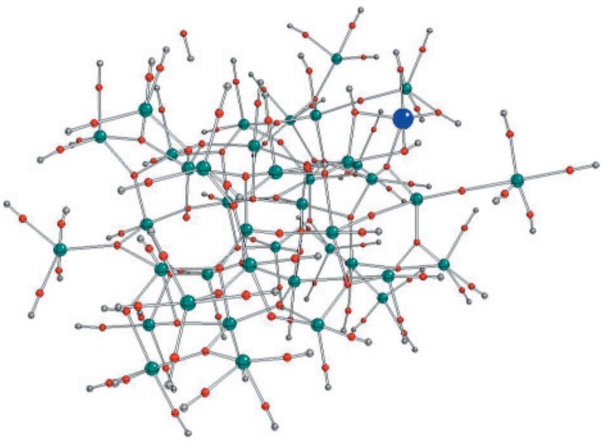

Model B3

Fig. 4. PM6 optimized geometry of $[\mathrm{Ti_{40}O_{124}H_{81}Cu}]^{5-}$ clusters, models B1–B3 (see Fig. 3 for atom notations).

are pentacoordinated by hydroxyls. The remaining models: B6, C1 and C2, have the Cu probe coordinated by a single bridging oxygen atom and 4—5 hydroxyls which can lead to irregularities in Cu charge. Average Cu—OH bond lengths (as a measure of corresponding Cu—O bond strengths implied by electron density transfer) follow the trends in the interaction energy parameters and Cu charges for hexacoordinated Ti edge centers unlike the pentacoordinated ones.

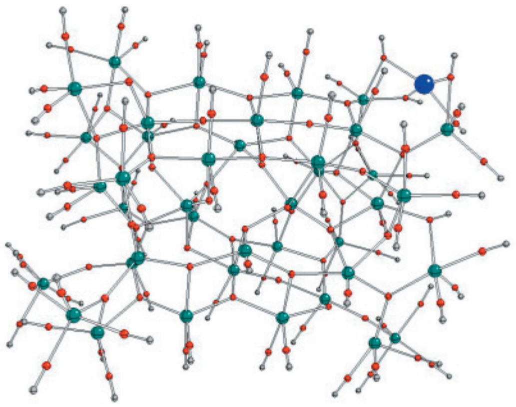

Model B4

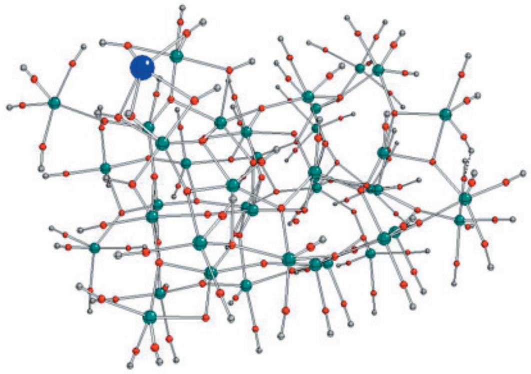

Model B5

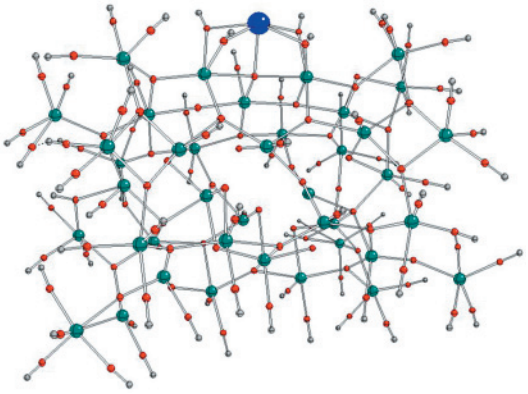

Model B6

Fig. 5. PM6 optimized geometry of $[Ti_{40}O_{124}H_{81}Cu]^{5-}$ clusters, models B4—B6 (see Fig. 3 for atom notations).

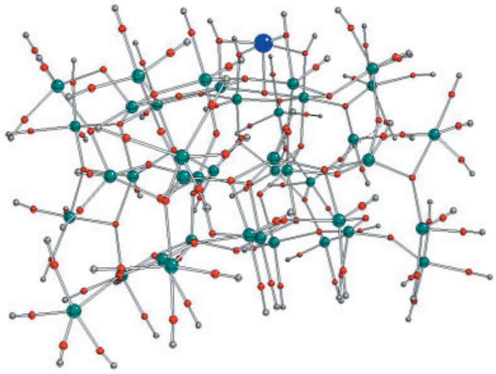

Model C1

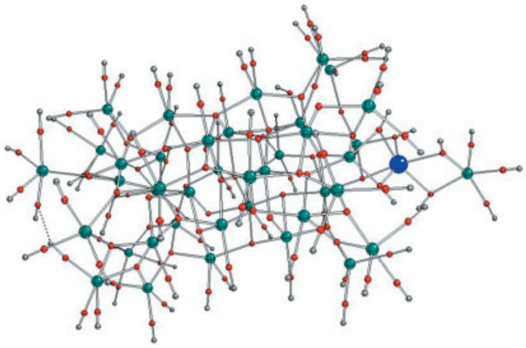

Model C2

Fig. 6. PM6 optimized geometry of $[Ti_{40}O_{124}H_{81}Cu]^{5-}$ clusters, models C1 and C2 (see Fig. 3 for atom notations).

Conclusions

If relative toxicity of individual Ti centers in rod-like rutile nanoparticles can be evaluated by the electron density transfer to a Cu^{2+} probe, its maximal values can be ascribed to the pentacoordinated corner (A model) and hexacoordinated edge Ti centers with three Ti—OH bonds (B1 model). However, these centers exhibit the least negative interaction energies, which can be compensated by the significantly better accessibility of the corner Ti center (A model) compared with that of the remaining ones. Ti centers with the most negative interaction energy parameters exhibit the lowest extent of electron density transfer to a Cu^{2+} probe (B3 and C2 models). Rutile nanoparticles destruction starts at pentacoordinated Ti face centers (C2 model).

Our model systems consist of three TiO_2 planes only and their protonation causes too high planes warping in comparison with significantly larger real systems. As quantum-chemical calculations of larger model systems are connected with serious technical problems even at the semiempirical level of theory, ONIOM treatment (Dapprich et al., 1999) combining semiempirical and molecular mechanics calculations should be used. Molecular mechanics methods enable to increase the size of model systems (which in our case reduces the plane warping due to surface protonation) but do not reveal their electron structure.

It has to be mentioned that our quantum-chemical treatment evaluates the electron affinity of individual surface reaction sites as the source of their toxicity (and, in general, of the oxidation stress). On the other hand, the experiments measure an integral response reflecting the microstructure properties of nanoparticles as a whole. In our future studies, the above-mentioned conclusions on toxicity of individual Ti centers in rutile nanoparticles will be extended to model systems of various shapes and sizes in order to identify their surface reaction sites. In the next step, nanoparticles of suitable shapes should be synthesized. This will subsequently enable studying in vitro correlations between theoretical and experimental data based on quantitative structure – activity relationship models.

Acknowledgements

This project has received funding from the European Union's Horizon 2020 research and innovation programme under grant agreement No 685817 (HISENTS). The authors thank the HPC center at the Slovak University of Technology in Bratislava, which is a part of the Slovak Infrastructure of High Performance Computing (SIVVP Project ITMS 26230120002, funded by the European Region Development Funds) for providing computing facilities. The authors also appreciate the Ministry of Education, Science, Research and Sport of the Slovak Republic for funding within the scheme 'Excellent research teams'.

References

Alagona G, Ghio C (2009) Antioxidant Properties of Pterocarpans through Their Copper(II) Coordination Ability. A DFT Study in Vacuo and in Aqueous Solution. J Phys Chem. A 113: 15206–15216.

Alagona G, Ghio C (2009a) Plicatin B conformational landscape and affinity to copper (I and II) metal cations. A DFT study. Phys Chem Chem Phys 11: 776–790.

Dapprich S, Komáromi I, Byun KS, Morokuma K, Frisch MJ (1999) A New ONIOM Implementation in Gaussian 98. 1. The Calculation of Energies, Gradients and Vibrational Frequencies and Electric Field Derivatives. J Mol Struct (Theochem) 462: 1–21.

Diebold U (2003) The surface science of titanium dioxide. Surf Sci Rep 48: 53–229.

Elgrabli D, Beaudouin R, Jbilou N, Floriani M, Pery A, Rogerieux F, Lacroix G (2015) Biodistribution and Clearance of TiO_2 Nanoparticles in Rats after Intravenous Injection. PLoS ONE 10: e0124490.

Fabian E, Landsiedel R, Ma-Hock L, Wiench K, Wohlleben W, van Ravenzwaay B (2008) Tissue distribution and toxicity of intravenously administered titanium dioxide nanoparticles in rats. Arch Toxicol 82: 151–157.

Frisch MJ, Trucks GW, Schlegel HB, Scuseria GE, Robb MA, Cheeseman JR et al. (2009) Gaussian 09, Revision D.01, Gaussian Inc., Wallingford, CT.

Appendix. Calculated energy terms in Table 3.

Tab. 3. Energies (E), Gibbs free energies (G_{298}) and enthalpies (H_{298}) at 298 K of the optimized structures and energies ($E_{L(Cu)}$) of $^1[Ti_{40}O_{124}H_{81}]^{7-}$ structures in the optimized geometries of $^2[Ti_{40}O_{124}H_{81}Cu]^{5-}$ structures obtained by the PM6 method for the model systems under study (model system charges as right superscripts) in the lowest spin states (spin multiplicities as left superscripts).

Compound	Model	E [hartree]	G_{298} [hartree]	H_{298} [hartree]	$E_{L(Cu)}$ [hartree]
$^2Cu^{2+}$	–	1.12549	1.10898	1.12785	–
$^1[Ti_{40}O_{124}H_{81}]^{7-}$	–	–16.76540	–16.06479	–15.48855	–
$^2[Ti_{40}O_{124}H_{81}Cu]^{5-}$	A	–17.08336	–16.36790	–15.79679	–16.62130
	B1	–17.12093	–16.40457	–15.83200	–16.66530
	B2	–17.18115	–16.46220	–15.89152	–16.68130
	B3	–17.23596	–16.52159	–15.94788	–16.70352
	B4	–17.19641	–16.47689	–15.90647	–16.68078
	B5	–17.18140	–16.4603	–15.89300	–16.67434
	B6	–17.15617	–16.43676	–15.86785	–16.62577
	C1	–17.18356	–16.46588	–15.89537	–16.63582
	C2	–17.22160	–16.5012	–15.93244	–16.69118

Energy, Gibbs free energy and enthalpy of $^2Cu^{2+}$ correspond to E_{ion} in Eq. (1). Analogous data of $^1[Ti_{40}O_{124}H_{81}]^{7-}$ correspond to E_L in Eqs. (1) and (2). Energies, Gibbs free energies and enthalpies of $^2[Ti_{40}O_{124}H_{81}Cu]^{5-}$ correspond to $E_{Complex}$ in Eq. (1).

Geraets L, Oomen AG, Krystek P, Jacobsen NR, Wallin H, Laurentie M et al. (2014) Tissue distribution and elimination after oral and intravenous administration of different titanium dioxide nanoparticles in rats. Part Fibre Toxicol 11: 0030.

Hanaor DAH, Assadi MHN, Li S, Yu A, Sorrell CC (2012) Ab initio study of phase stability in doped TiO_2. Comput Mechan 50: 185–94.

Hanaor DAH, Xu W-Q, Ferry M, Sorrell CC (2012a) Abnormal grain growth of rutile TiO_2 induced by $ZrSiO_4$. J Cryst Growth 359: 83–91.

Hussain H, Tocci G, Woolcot T, Torrelles X, Pang CL, Humphrey DS, Yim CM, Grinter DC, Cabail G, Bikondo O, Lindsay R, Zegenhagen J, Michaelides A, Thornton G (2017) Structure of a model TiO_2 photocatalytic interface. Nature Mater 16: 461–466.

Mammino L (2013) Investigation of the antioxidant properties of hyperjovinol A through its Cu(II) coordination ability. J Mol Model 19: 2127–2142.

Mulliken RS (1955) Electronic Population Analysis on LCAO-MO Molecular Wave Functions. I. J Chem Phys 23: 1833–1840.

Olmedo D, Guglielmotti MB, Cabrini RL (2002) An experimental study of the dissemination of Titanium and Zirconium in the body. J Mater Sci-Mater Medicine 13: 793–796.

Wang JX, Zhou GQ, Chen CY, Yu HW, Wang TC, Ma YM et al. (2007) Acute toxicity and biodistribution of different sized titanium dioxide particles in mice after oral administration. Toxicol Let 168: 176–185.

Puškárová I. Breza M (2016) DFT studies of the effectiveness of p-phenylenediamine antioxidants through their Cu(II) coordination ability. Polym Degrad Stab 128: 15–21.

Stephens PJ, Jalkanen KJ, Kawiecki RW (1990) Theory of vibrational rotational strengths: comparison of a priori theory and approximate models. J Am Chem Soc 112: 6518–6529.

Stewart JJP (2007) Optimization of parameters for semiempirical methods. V. Modification of NDDO approximations and application to 70 elements. J Mol Model 13: 1173–1213.

Swope RJ, Smyth JR, Larson AC (1995) H in rutile-type compounds: I. Single-crystal neutron and X-ray diffraction study of H in rutile. Am Mineral 80: 448–453.

Wang Y, Chen Z, Ba T, Pu J, Chen T, Song Y et al. (2013) Susceptibility of young and adult rats to the oral toxicity of titanium dioxide nanoparticles. Small 9: 1742–1752.

Xie G, Wang C, Zhong G (2011) Tissue distribution and excretion of intravenously administered titanium dioxide nanoparticles. Toxicol Let 205: 55–61.

Zhang Z, Fenter P, Sturchio NC, Bedzyk MJ, Machesky M, Wesolowski DJ (2007) Structure of rutile TiO_2 (110) in water and 1 molal Rb^+ at pH 12: Inter-relationship among surface charge, interfacial hydration structure, and substrate structural displacements. Surf Sci 601: 1129–1143.

sciendo

Growth of *Staphylococcus aureus* 2064 described by predictive microbiology: From primary to secondary models

Alžbeta Medveďová, Adriana Havlíková, Ľubomír Valík

Department of Nutrition and Food Quality Assessment, Faculty of Chemical and Food Technology,
Slovak University of Technology in Bratislava Radlinského 9, Bratislava 812 37, Slovakia
alzbeta.medvedova@stuba.sk

Abstract: The growth of *Staphylococcus aureus* 2064 isolate in model nutrient broth was studied as affected by temperature and water activity using principles and models of predictive microbiology. Specific rates resulting from growth curves fitted by the Baranyi model were modelled by the secondary Ratkowsky model for sub-optimal temperature range (RTKsub) as well as the Ratkowsky extended model (RTKext) and cardinal model (CM) in the whole temperature range. With the biological background of the RTKext model, cardinal values of temperature T_{min} = 6.06 °C and T_{max} = 47.9 °C and water activity $a_{w\,min}$ = 0.859 were calculated and validated with cardinal values estimated by CM (T_{min} = 7.72 °C, T_{max} = 46.73 °C, $a_{w\,min}$ = 0.808). CM also provided other cardinal values, T_{opt} = 40.63 °C, $a_{w\,\text{opt}}$ = 0.994, as well as optimal specific growth rate of 1.97 h^{-1} (at T_{opt} and $a_{w\,\text{opt}}$). To evaluate the goodness of fit of all models, mathematical and graphical validation was performed and the statistical indices proved appropriateness of all the secondary models used.

Key words: food safety, prediction, *Staphylococcus aureus*, temperature, water activity

Introduction

Regardless the intensive effort in food hygiene, increase of knowledge and available resources, *Staphylococcus aureus* is still a challenge for food microbiologists and technologists, mainly in products with increased manual handling, which is documented by higher occurrence of *S. aureus* in food. For example in 2016, 17 % of 962 milk samples tested in Italy and 21 % of 940 food samples in Spain were positive for *S. aureus*. In 2017, the total of 655 (3.6 %) of the 18,361 food samples tested in the European Union were positive for this species. Moreover, one outbreak of staphylococcal intoxication occurred in the European Union in 2017 (EFSA Report 2017, 2018). In Slovakia, there were 174 cases of staphylococcal food-poisoning (SFP) outbreaks in 2016 and 14 cases in 2017. As the symptoms of SFP disappear quickly in healthy population, it is generally known that data underestimate the real situation in the food chain. In Slovakia occurrence of *S. aureus* was confirmed in 1.5 % of 13,221 tested food samples in 2016 and in 2 % of 12,291 tested samples in 2017 (Report on Zoonoses 2017, 2018).

The awareness of *S. aureus* in food and food environment results from its good growth in various food matrices, tolerance to low water activity and wide range of virulent factors, production of which is dependent on actual *S. aureus* growth ability. *S. aureus* is a versatile microorganism capable of quick adaptation to different environmental conditions (Mariutti et al., 2017) and persists even on plastic surfaces thanks to the interaction of teichoic acid, which is a part of Gram-positive bacteria cell membrane, with other surface polymers (Reffuveille et al., 2017). It is normally found on the skin of about 10—50 % asymptomatic humans (ECDC, 2017) and in animals. In the European Union, 56.4 % of 225 animal samples tested in 2016 and 29.6 % of 4,812 animal samples in 2017 were positive for *S. aureus* presence (EFSA Report 2017, 2018). In Slovakia, 17.8 % positive samples of 1,949 tested animals in 2016 and 18.4 % of 2,907 tested animal samples in 2017 were found positive (Report on Zoonoses 2017, 2018). Due to the production of a wide range of surface-associated factors, enzymes, toxins and superantigenic toxins, *S. aureus* is considered as a pathogen (Ote et al., 2011; Arbuthnott et al., 1990) but diseases caused by *S. aureus* do not necessarily originate only in direct tissue invasion (Mariutti et al., 2017). From the food point of view, the production of one or more of heat-resistant staphylococcal enterotoxins (SEs) is the most crucial, because they are a causative agent of SFP outbreaks. The production of SEs is strongly dependent on environmental factors (Medveďová et al., 2017); thus the role of food microbiologists is to prevent *S. aureus* to grow and subsequently to produce SEs. In this context, predictive microbiology and its models represent a very useful tool.

As defined by Ross and McMeekin (1994), predictive microbiology is based on the premise that responses of microbial populations to environmental factors are reproducible, and that it is possible to predict microbial responses from past observations considering the environment in terms of identifiable dominating constraints. Based on cultivation experiments, the growth (or sometimes inactivation) of microorganisms is defined and subsequently described by primary models. These are defined by the change of microbial count as a function of time ($N = f(t)$) in constant conditions and their result is the definition of growth parameters (specific growth rate μ, lag phase duration *lag*, etc.). In a next step/advantage of predictive microbiology, the effects of changing environmental conditions (temperature, water activity, pH, etc.) on microbial growth parameters can be described by the use of secondary models (Valík et al., 2019; Dubois-Brissonnet et al., 2015). Applying appropriate secondary models, cardinal values of environmental factors enabling growth of selected microorganisms can be defined. Finally, tertiary models are available in predictive microbiology. They include databases, fitting utilities, growth/no growth predictions, probability models and risk assessment modules enabling a wide range of applications such as HACCP system support, product and process design, shelf life assessment, sampling plans and experimental design and education (Valík et al., 2019).

However, to reliably and precisely predict microbial response to changing environmental factors, the adequate model has to be used. As stated by McMeekin et al. (2008), the process of model building in not simply a matter of finding an equation describing a single or some data sets. The equation should be based on biological observations; it should provide useful information about the relation between the microorganism and its environment. Moreover, the confidence in predictions significantly increases when different models or models from different sources provide comparable estimates of environmental influence on the microbial population behavior (Wood, 2016; McMeekin et al., 2008). Therefore, application of different secondary models (Ratkowsky model RTKsub, Ratkowsky extended model RTKext and cardinal model CM) describing the simultaneous effect of temperature and water activity on the growth of isolate *S. aureus* 2064 in model nutrient broth has been studied. Furthermore, the cardinal values of temperature and water activity of the isolate were defined and verified.

Materials and methods

Microorganism

The effect of simultaneous effect of temperature (8, 10, 12, 15, 18, 21, 25, 30, 35, 37, 39, 43, 46 and 50 °C ±0.5 °C) and water activity (a_w ranging from 1.0 to 0.84) on growth of *S. aureus* 2064 was studied. The identity of this isolate was earlier confirmed by Medveďová et al. (2011).

Media

The isolate was maintained on slopes of Plate Count Agar (PCA; Difco, Le Pont de Claix, France) at 6 ±1 °C. Its standard inoculum (0.3 mL from 10^3 dilution of an 18 h isolate culture grown on PCA agar at 37 °C) was inoculated aseptically into 300 mL of pre-tempered glucose-tryptone yeast extract broth (GTYE; Difco, Le Pont de Claix, France) to reach initial counts as close as possible to 10^3 CFU mL^{-1}. The samples were incubated in three parallels under static aerobic conditions at selected temperatures and a_w values. The a_w values of GTYE broth were set by an addition of NaCl (Sigma-Aldrich, Buchs, Switzerland) according to Rödel et al. (1979) and controlled by an a_w-meter (Aw-Sprint TH500, Novasina, Lachen, Switzerland).

Counts of S. aureus 2064 in growth media

At chosen time intervals, depending on actual temperature and a_w, cell numbers of *S. aureus* 2064 were determined according to ISO 4833-1:2013 on PCA agar (Sigma-Aldrich, St. Louis, USA).

Fitting the growth curves and primary modelling

S. aureus 2064 growth parameters were analysed, fitted and calculated using the DMFit Excel Add-in package version 3.5 (ComBase managed by the United States Department of Agriculture-Agricultural Research Service, Washington, DC, USA and the University of Tasmania Food Safety Centre Hobart, Australia) that incorporates the mechanistic model of Baranyi and Roberts (1994). Actual counts were plotted against time and fitted by a model for the estimation of μ and further analysed by secondary models using the Microsoft Office version 2013 (Microsoft, Redmond, Washington, USA) and the Statistica data analysis software system, version 10.0 (Tibco Software, Inc., Palo Alto, USA).

Secondary modelling

Growth parameters from each individual growth curve were analysed by secondary models. Specific growth rate (μ) was modelled as a function of the incubation temperature (T) in the suboptimal temperature range at all studied a_w values according to the Ratkowsky model (RTKsub):

$$\sqrt{\mu} = b\left(T - T_{\min}\right) \times \sqrt{\left(a_w - a_{w\min}\right)} \qquad (1)$$

where $T_{\min}$ and $a_{w\min}$ are the temperature or a_w, respectively, below which no growth is observed. Growth parameters estimated at 43 °C and 46 °C (n = 38) were excluded from the suboptimal temperature data set. All model parameters ($T_{\min}$, $a_{w\min}$ and b) were calculated by non-linear regression analysis (Microsoft Excel and Statistica v. 10.0). To describe the simultaneous effect of a_w and temperature in the whole range of these environmental factors, the extended model of Ratkowsky (RTKext) was used (Ratkowsky et al., 1983):

$$\mu_{max} = b\left[(T - T_{\min}) \times \left\{1 - exp\left[c - (T - T_{\max})\right]\right\}\right]^2 \times \\ \times (a_w - a_{w\min}) \times \left\{1 - exp\left[d(a_w - a_{w\max})\right]\right\} \qquad (2)$$

where, $T_{\min}$ and $a_{w\min}$ have the same meaning as previously, $T_{\max}$ and $a_{w\max}$ are the temperature or a_w, respectively, above which no growth occurs.

Cardinal model (CM) was used to describe the cumulative influence of temperature and a_w on the microbial growth rate. Maximum specific growth rate was subjected to secondary modelling in relation to the incubation temperature (Rosso et al. 1993). The combined effect of temperature and a_w was determined according to the **gamma concept** (Zwietering et al., 1991) based on individual cardinal models (Rosso et al., 1993):

$$\mu_{\max}(T, a_w) = CM(T, a_w) = \mu_{\text{opt}} \times \tau(T) \times \gamma(a_w) \qquad (3)$$

where $\tau(T)$ and $\gamma(a_w)$ are in Eqs. 4 and 5, where T_{opt} is the temperature at which the maximum specific growth rate equals its optimal value, μ_{opt}.

Goodness of fit

To evaluate the goodness of fit of mathematical models, several mathematical and statistical indices were used. The ordinary least-squares criterion and regression coefficient (R^2) were used to fit the models to the data. The goodness of fit of the modelling approach was assessed by the root mean square error (*RMSE*), which measures the average deviation between the observed and predicted values (Garcia et al., 2011). Also standard error of prediction (%*SEP*) as reported Zurera-Cosano et al. (2006) and the per cent of variance (%*V*) as reported Daughtry et al. (1997) were used.

Results and discussion

A typical representation of an increase of bacterial culture with time is a sigmoid curve, as it is also depicted in Fig. 1. In a given environment allowing growth of bacterial population, typical phases of the growth curve are visible. First is the **lag phase** characterized as an adjustment period of the cells to the new environment; the **growth phase** is characterized by exponential increase of cells defined by specific growth rate (μ) and finally, the **stationary phase** during which the increment of cells is equal to their inactivation rate. The most worldwide used primary model describing the dynamics of bacterial cultures growth is the model introduced by Baranyi and Roberts (1994). Its main advantage is that the definition of the lag phase is independent of the growth curve shape and the effect of previous environment is separated from that of the present environment (Baranyi et al., 1993).

This model was also successfully applied (R^2 ranging from 0.973 to 0.998) to describe the growth dynamics of isolate *S. aureus* 2064 at 39 °C affected by changing a_w values. The temperature of 39 °C was chosen from the temperature rage since almost optimal growth of the 2064 isolate was observed, as it will be discussed further. At almost all studied a_w values; the growth curves of the isolate had a typical sigmoid shape. The only exception was the experiment at $a_w = 0.842$, when only the growth inhibition of the isolate was noticed without any previous adaptation phase to such inhospitable conditions.

In the secondary phase of predictive modelling, the effect of environmental factors, e.g. a_w and/or temperature on the growth parameters is described (Valík et al., 2019; Dubois-Brissonnet et al., 2015). Experimental data (points in Figures 1–3) are compared to the microorganisms behaviour (graticule in Figures 1–3) predicted by the selected model. Reliability and accuracy of the model are subsequently evaluated within the validation process.

To simply and quickly describe the effect of temperature and a_w, the Ratkowsky model (RTKsub; Eq. 1; Ratkowsky et al., 1983) was used for the data set of 209 growth parameters. The disadvantage of RTKsub model is that it is applicable only in the suboptimal temperature range and thus, in case of *S. aureus* 2064, the experimental data obtained at 43 °C and 46 °C were excluded. The RTKsub model parameters and evaluation indices are summarized in Table 1. From statistical evaluation as well from

$$\tau(T) = \frac{(T - T_{\max})(T - T_{\min})^2}{(T_{\text{opt}} - T_{\min})\left[(T_{\text{opt}} - T_{\min})(T - T_{\text{opt}}) - (T_{\text{opt}} - T_{\max})(T_{\text{opt}} + T_{\min} - 2T)\right]} \qquad (4)$$

$$\gamma(a_w) = \frac{(a_w - a_{w\max})(a_w - a_{w\min})^2}{(a_{w\text{opt}} - a_{w\min})\left[(a_{w\text{opt}} - a_{w\min})(a_w - a_{w\text{opt}}) - (a_{w\text{opt}} - a_{w\max})(a_{w\text{opt}} + a_{w\min} - 2a_w)\right]} \qquad (5)$$

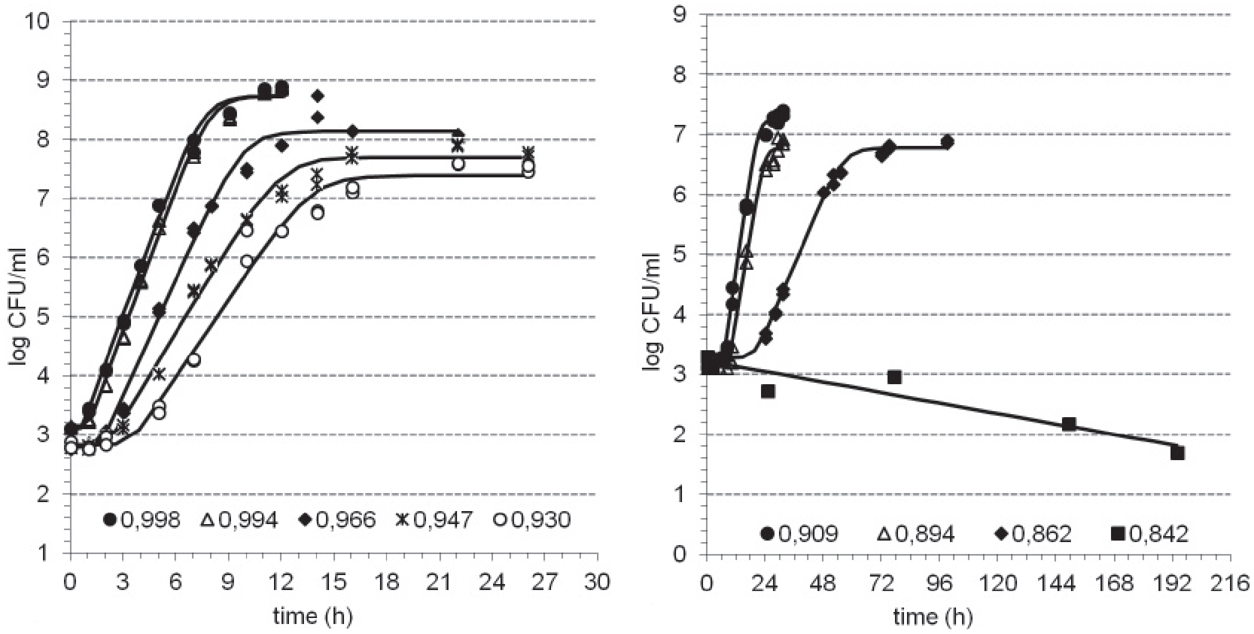

a) b)

Fig. 1. Growth curves of *S. aureus* 2064 in GTYE broth at 39 °C in dependence on a_w modelled by primary model of Baranyi and Roberts (1994).

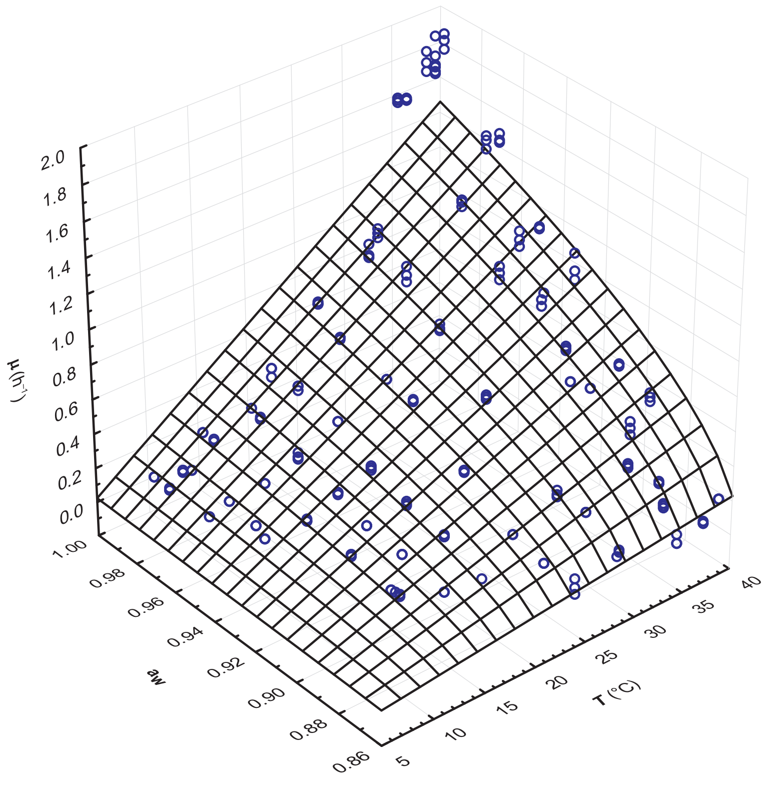

Fig. 2. Graphical presentation of RTKsub model of the effect of a_w and T in the suboptimal range (10 °C—39 °C) on the specific growth rate of *S. aureus* 2064 ($n = 209$).

graphical presentation of the model (Fig. 2), the highest variance occurred and the linearity of the model was disrupted at temperatures close to the optimal one. Further increase of the incubation temperature led to slower growth rate and subsequent change of the linear trend of the model line, as the curvature appeared at higher temperatures. So, to model the effect of temperature in the whole temperature range allowing the growth of selected microorganism, the RTKext (Eq. 2) was used.

The whole a_w region was included into modelling similarly as in the previous case, but also the whole T region was accounted for. RTKext was an appropriate model for the *S. aureus* 2064 growth rate in dependence on these two environmental factors; their simultaneous effect on specific growth rate of *S. aureus* 2064 is depicted in Fig. 3. As it can be seen, the specific growth rate increased with a constant slope with the incubation temperature increase up to 40 °C. At temperatures above 40 °C, the growth of *S. aureus* slowed down at all a_w values. Therefore, the curvature is observed in the optimal region, i.e. 35–40 °C. Asperger and Zangerl (2003) or Normanno et al. (2007) also confirmed the mesophilic character of *S. aureus* with the optimum temperature in the range from 37 °C to 40 °C. Regarding the effect of a_w, the increase of specific growth rate with the increase of a_w value also shows a constant slope and a very small curvature at the a_w value of about 0.994 (however, not as significant as in case of temperature). A slightly lower a_w or small amounts of NaCl (1.5 %) in media are needed to reach more intensive growth as was also confirmed by Cebrián et al. (2015).

Response of *S. aureus* 2064 to the simultaneous influence of changing temperature and a_w values fitted by the RTKext model is described by the following equation, with defined degree of reliability given by validation indices summarized in Table 1:

$$\begin{aligned}\mu_{max} &= 0.0144 \times \\ &\times \left[(T - T_{min}) \times \left\{1 - \exp\left[0.3345 - (T - T_{max})\right]\right\}\right]^2 \times \\ &\times (a_w - a_{w,min}) \times \left\{1 - \exp\left[1241.9(a_w - a_{w,max})\right]\right\}\end{aligned}$$

An advantage of the RTKext model is that it is able to provide definition of cardinal values of modelled environmental factors. So, applying this model for *S. aureus* 2064 growth data set, T_{min} = 6.06 °C, T_{max} = 47.9 °C and $a_{w\,min}$ = 0.859 were calculated. Although the RTKext model proved its appropriateness, it can provide only three cardinal values. In this context, application of the CM model is more complex. According to the CM model in combination with a global fit, seven parameters of the CM model, i.e. cardinal temperatures (T_{min} = 7.72 °C, T_{opt} = 40.63 °C, T_{max} = 46.73 °C), cardinal a_w values ($a_{w\,min}$ = 0.808, $a_{w\,opt}$ = 0.994, $a_{w\,max}$ fixed to 1) and the optimal growth rate (μ_{opt} = 1.97 h^{-1}) were determined.

Differences between the calculated cardinal values, i.e. about 1 °C in the minimum and maximum temperatures and about 0.05 of a_w, may result from different approaches that both models use for fitting to experimental data set. The RTKext model offers a wider temperature range; however, applying the CM model allows the isolate to grow at higher NaCl addition (at about 22 %). Based on validation indices, both models proved their appropriateness, however, CM model is preferred based on higher R^2 and $\%V$ coefficients and lower $RMSE$ and SEP indices.

Besides mathematical evaluation of the goodness of fit of the models, also graphical comparison of predicted (μ_{calc}) and experimental (μ_{exp}) values of *S. aureus* 2064 specific growth rates was performed (Fig. 4). From Fig. 4 it is obvious that RTKext and CM are more suitable for the prediction of *S. aureus*

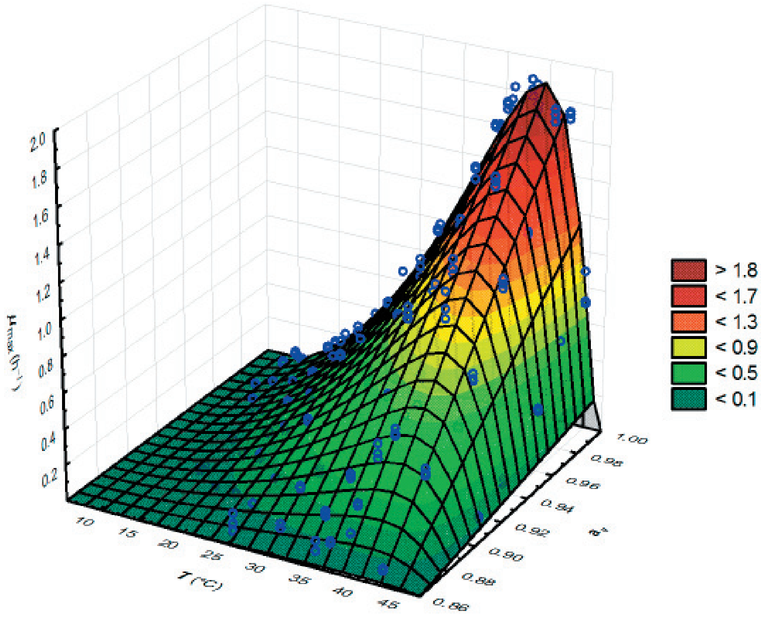

Fig. 3. Simultaneous effect of temperature and a_w on the specific growth rate of *S. aureus* 2064 (n = 247) modelled by RTKext in the whole studied ranges of temperature and a_w.

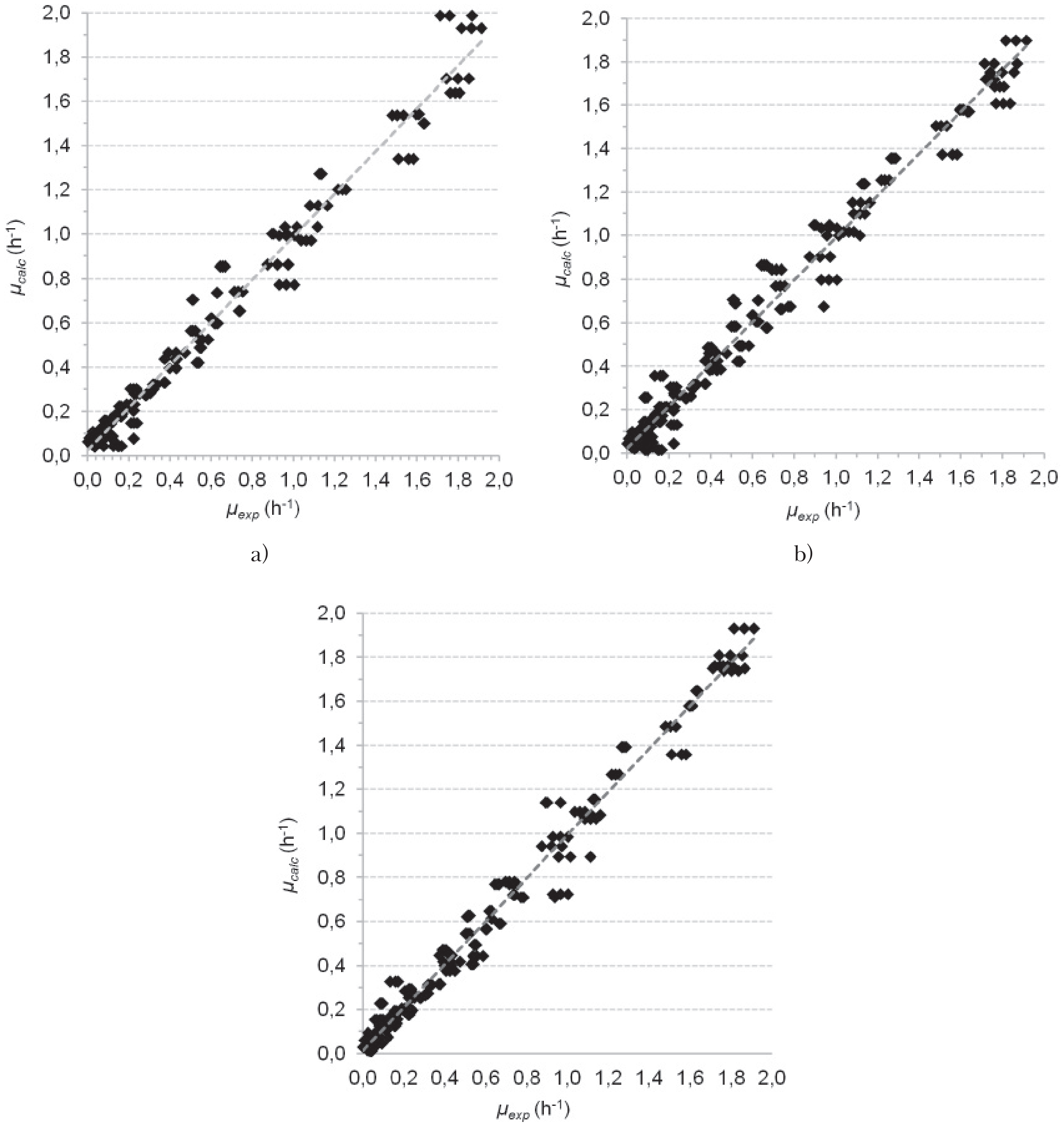

a)

b)

c)

Fig. 4. Comparisons of μ-values of *S. aureus* 2064 estimated with RTKsub (4a), RTKext (4b) and CM models (4c) with experimental values.

growth in dependence on temperature and a_w in the whole range of food environmental factors.

Conclusion

Usefulness of predictive microbiology has been pointed out for the simultaneous effect of temperature and water activity on the growth of *S. aureus* 2064. The process of predictive modelling was presented with the *pros* and *cons* of some secondary models. Moreover, cardinal temperatures ($T_{\min}$ = 6.06–7.72 °C, T_{opt} = 40.63 °C, $T_{\max}$ = 46.73–47.9 °C) and water activity ($a_{w\,\min}$ = 0.808–0.859, $a_{w\,\text{opt}}$ = 0.994) of *S. aureus* 2064 and its optimal μ = 1.97 h^{-1} at both optimal factors were calculated. The presented results can be applied in the control of the *S. aureus* growth and potential staphylococcal enterotoxins production in food practice and research.

Acknowledgment

This work was financed by the Slovak Research and Development Agency (Contract No. APVV-15-006) and the

Tab. 1. Parameters of models and validation indices for RTKsub, RTKext and CTMI models used for the prediction of *S. aureus* 2064 growth in dependence on temperature and a_w.

Model parameters	RTKsub	RTKext	CTMI
b	0.1085	0.0144	–
c	–	0.3345	–
d	–	1241.9	–
μ_{opt}	–		1.97
T_{min}	4.45	6.06	7.72
T_{opt}	–		40.63
T_{max}	–	47.91	46.73
$a_{w\,min}$	0.857	0.859	0.808
$a_{w\,opt}$	–		0.994
$a_{w\,max}$	–	1 (fixed)	1 (fixed)
n	209	247	247
R^2	0.977	0.977	0.983
RMSE	0.0824	0.0847	0.0732
SEP	0.158	0.152	0.073
%V	97.7	97.6	98.2

Scientific Grant Agency of the Ministry of Education of the Slovak Republic and Slovak Academy of Science – VEGA 1/0532/18.

References

Arbuthnott J, Coleman D, DeAzavedo J (1990) Journal of Applied Bacteriology Symposium Supplement 69: 1S–8S.

Asperger H, Zangerl P (2003) In: Roginski H, Fuquay J, Fox P (Eds) Encyclopedia of Dairy Science (pp 2563–2569). Academic Press, San Diego.

Baranyi J, Roberts TA (1994) International Journal of Food Microbiology 26: 199–218.

Baranyi J, Roberts TA, McClure P (1993) Food Microbiology 10: 43–59.

Cebrián G, Arroyo C, Condón S, Mañas P (2015) International Journal of Food Microbiology 214: 83–90.

Daughtry BJ, Davey KR, King KD (1997) Food Microbiology 14: 21–30.

Dubois-Brissonnet F, Guillier L, Naitali M (2015) International Journal of Food Studies 4: 134–140.

ECDC (2017) Antimicrobial resistance surveillance in Europe 2015, Surveillance report, Avialable in May 2017: http://ecdc.europa.eu/en/publications/Publications/antimicrobial-resistance-europe-2015.

The European Union Summary Report on Trends and Sources of Zoonoses, Zoonotic Agents and Food-borne Outbreaks in 2017 (2018). EFSA Journal 16(12): 5500.

The European Union Summary Report on Trends and Sources of Zoonoses, Zoonotic Agents and Food-borne Outbreaks in 2016 (2017). EFSA Journal 15(12): 5077.

Garcia D, Ramos AJ, Sanchis V, Marín S (2011) Food Microbiology 28: 406–417.

Mariutti RB, Tartaglia NR, Seyffert N, de Paula Castro TL, Arni RK, Azevedo VA, Le Loir Y, Nishifuji K (2017) In: Enany S, Alexander LEC (Eds) The rise of virulence and antibiotic resistance in *Staphylococcus aureus*, (pp 127–143). InTech, Rijeka.

McMeekin T, Bowman J, McQuestin O, Mellefont L, Ross T, Tamplin M (2008) International Journal of Food Microbiology 128: 2–9.

Medveďová A, Havlíková A, Valík Ľ (2017) In: Enany S, Alexander LEC (Eds) The rise of virulence and antibiotic resistance in *Staphylococcus aureus*, (pp 145–167). InTech, Rijeka.

Medveďová A, Valík Ľ, Liptáková D (2011) Journal of Food and Nutrition Research 50: 193–198.

Normanno G, LaSalandra G, Dambrosio A, Quaglia NC, Corrente M, Parisi A, Santagada G, Firinu A, Crisetti E, Celano GV (2007) International Journal of Food Microbiology 115: 290–296.

Ote T, Taminiau B, Duprez JN, Dizier I, Mainil JG (2011) Veterinary Microbiology 153: 285–292.

Ratkowsky DA, Lowry RK, McMeekin TA, Stokes AN, Chandler RE (1983) Journal of Bacteriology 154: 1222–1226.

Reffuveille F, Josse J, Vallé Q, Mongaret C, Gangloff SC (2017) In: Enany S, Crotty Alexander LE (Eds.) The rise of virulence and antibiotic resistance in *Staphylococcus aureus*, (pp. 189–214). InTech, Zagreb.

Report on Zoonoses, alimentary diseases and diseases from water in Slovak Republic in 2017 (2018) 118 p.

Report on Zoonoses, alimentary diseases and diseases from water in Slovak Republic in 2016 (2017) 114 p.

Ross T, McMeekin TA (1994) International Journal of Food Microbiology 23: 241–264.

Rosso L, Lobry JR, Flanders JP (1993) Journal of Theoretical Biology 162: 447–463.

Rödel W, Krispien J, Leistner L (1979) Fleischwirtschaft 59: 849–851.

Valík Ľ, Medveďová A, Ačai P (2019) Journal of Food and Nutrition Research, in press.

Wood J (2016) Bioinformatics review 2: 15–17.

Zurera-Cosano G, Garciá-Gimeno RM, Rodríguez-Pérez R, Hervás-Martínez C (2006) Food Control 17: 429–438.

Zwietering MH, De Koos JT, Hasenack BE, De Wit JC, Riet K (1991) Applied and Environmental Microbiology 57: 1094–1101.

sciendo

3-Hydroxymethyl-1,4-dihydro-4-oxoquinoline like compound with promising biological and complexing activity

Viktor Milata, Maroš Bella, Robert Kurinec

Department of Organic Chemistry, Institute of Organic Chemistry, Catalysis and Petrochemistry,
Faculty of Chemical and Food Technology, Slovak University of Technology,
812 37 Bratislava, Radlinského 9, Slovakia
viktor.milata@stuba.sk

Introduction

Hydroxymethyl group is present in many useful and biologically potent substances like sugars, kojic acid (Bajpai, 1982), ronicol (3-hydroxymethylpyridine) (Moncol, 2006; Broghammer, 1967) or hydroxymethylphenol — intermediate for bakelite (Baekeland, 1909).

On the other hand, 4-quinolones are a group of antibacterials with various biological activities if substituted in position 3- and they are anti-CNS and similar diseases agents if substituted in position 2- (kynurenic acid derivatives) (Turski, 2013; Szalardy, 2012; Fulop, 2009). Considering this, we were interested in the synthesis of 3-hydroxymethyl-1,4-dihydro-4-oxoquinoline.

4-Quinolones are a well-known group of chemotherapeutics with a broad spectrum of activities (Andriole, 2000; Milata, 2000) based on inhibition of the enzyme of bacterial topoisomerase II (DNA gyrase) and topoisomerase IV in Gram-positive species, thus inhibiting tertiary negative supercoiling of bacterial DNA (Gellert, 1976; Wang, 1985; Gootz, 1996) mostly bound to oxygen atoms in positions 3- and 4- of the fused pyrid-4-one-3-carboxylic acid moiety (Andriole, 2000). Therefore, it should be interesting to prepare and evaluate the corresponding structural motif, namely 3-hydroxymethylquinol-4-one.

Substructural search in database SciFinder® provided only various applications of formaldehyde with 4-quinolones or their precursors (Goldsworthy, 1982) but no true synthesis has been reported. Therefore, this compound with promising binding and complexing activity has been prepared.

Materials and Methods

Spectrometer INOVA 300 (300 MHz, Varian Inc., Palo Alto, CA, USA) was used to measure ^{1}H NMR spectra, at their RT frequencies. Chemical shifts in (δ)—[ppm] (parts per million) were referenced to the residual signal of the solvent. Coupling constants (J) are given in [Hz] with multiplicity: s (singlet), d (doublet), dd (doublet of the doublet), t (triplet), q (quartet), q (quintet) and m (multiplet). Tetramethylsilane was used for the calculation of ^{1}H chemical shift scales and correctly referenced using the (residual) solvent signals (2.50 and 39.52 ppm for DMSO).

All reagents and solvents were purchased from Sigma-Aldrich® (Darmstadt, Germany), Alfa-Aesar® (Ward Hill, MA, USA), Fluka® (Buchs, Switzerland) and Mikrochem® (Pezinok, Slovakia). Solvents were purified and/or dried using standard laboratory methods and stored over molecular sieves (4 Å). Column chromatography was performed using silica gel Nomasil—40—63 m (VWR®, Randor, PA, USA) and a suitable eluent according to TLC. Reaction progress was monitored by thin layer chromatography on Silufol or Alufol plates (Merck®, Darmstadt, Germany) with a UV indicator for λ = 254 nm.

Melting points (m. p.) of the prepared compounds were determined on a Boetius micro hot stage using digital thermometer TD 121 (VWR®, Randor, PA, USA) and are uncorrected.

Experimental

3-Hydroxymethyl-4-oxo-1,4-dihydroquinoline 7

A sample of 0,5 g (2,3 mmol) of ethyl 1,4-dihydro-4-oxoquinoline-3-carboxylate (**4**) was added to a 100 mL flask and solved in dry THF (20 mL) equipped with a $CaCl_2$ drying stopper under argon at LT. To this solution, small portions of powdered $LiAlH_4$ (0.5 g) were added and the mixture was stirred at LT for 24 hours. Then, it was poured into a water solution of NH_4Cl (50 mL, 10 %) which was afterwards filtered and the filter was washed with ethyl acetate. The filtrate was also extracted with ethyl acetate. Both parts were collected and evaporated to dryness. Yield 0.3 g (74,4 %) of 3-hydroxymethyl-4-oxo-1,4-dihydroquinoline, almost pure raw product. M. p. 183—184 °C.

Elemental analysis (calc./found): %C: 68,57/68,69, %H: 5,14/4,96 and %N: 8,00/7,69.

^{1}H NMR (DMSO-d_6): 4.42 d (CH_2, 2H, 4,8 Hz), 4.94 t (OH, 1H, 4,8 Hz), 7.30 t (H-8, 1H, 7,8 Hz), 7.53 d (H-6, 1H, 7,8 Hz), 7,63 t (H-7, 1H, 7,8 Hz), 7,88 bs (H-2, 1H), 8.11 d (H-5, 1H, 7,8 Hz).

Results and Discussion

3-Hydroxymethyl derivative **7** represents an interesting tautomeric system (Scheme 1).

4-Oxoform B, compared to tautomer A, includes an intramolecular hydrogen bond between oxygen of the carbonyl group of the 4-pyridone system and hydrogen of the hydroxyl group. Another possible tautomer is aromatic 4-hydroxyquinoline with intramolecular hydrogen bond between hydrogen of the hydroxy group of 4-hydroxyquinoline and oxygen of the hydroxymethyl group (C) (Scheme 1).

Our first attempt was focused on the exploitation of formaldehyde as a hydroxymethylation agent considering that unsubstituted 4-quinolone (**6,** prepared from **4** *via* **5,** Scheme 2) reacts under the conditions of electrophilic substitution to position 3-, which has the highest electron density in the enaminone system, in agreement with previous results (Zubkov, 2003). Variation of reaction conditions (time, temperature, solvent) resulted in unsatisfactory yields, reactions produced mixtures of deeply colored and hardly separable by-products.

The second strategy was based on the reduction of corresponding 3-ethoxycarbonylderivative, easily accessible through the Gould-Jacobs reaction (Nicolson 1989). Heating of the starting equimolar mixture of aniline and diethyl ethoxymethylene malonate (EMME) to 120–130 °C for three hours (instead of 2 h at 130 °C) gave only an 83 % yield after cooling to LT (Nicolson, 1989: 96 % after cooling to –78 °C). Thermal cyclisation of diethyl anilinomethylene malonate (**3**) in diphenyl ether to reflux, including cooling of the reaction mixture, filtering off of the separated raw solid (**4**) and washing with chloroform to remove traces of **3** yielded 60 % of ethyl 4-oxo-1,4-dihydroquinoline-3-carboxylate (**4**) (Nicolson, 1989: after cyclisation in Dowtherm, an eutectic mixture of biphenyl and diphenyl ether offered a 73 % yield after recrystallisation from acetic acid). Dilution of **3** in solvent was 2,63 g/20 ml while Nicolson (1989) used the dilution of 10 g/50 ml both for 30 min.

Acknowledgement

This work was financially supported by the Science and Technology Assistance Agency under the contract No. APVV-17-0513.

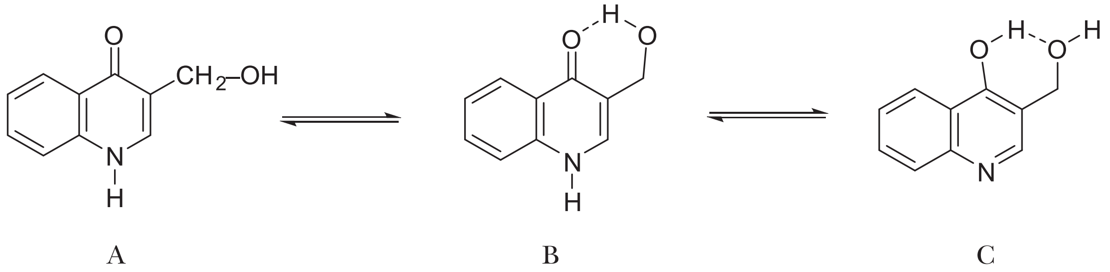

Scheme 1. Tautomerism of 3-hydroxymethyl-1,4-dihydro-4-oxoquinoline **7**.

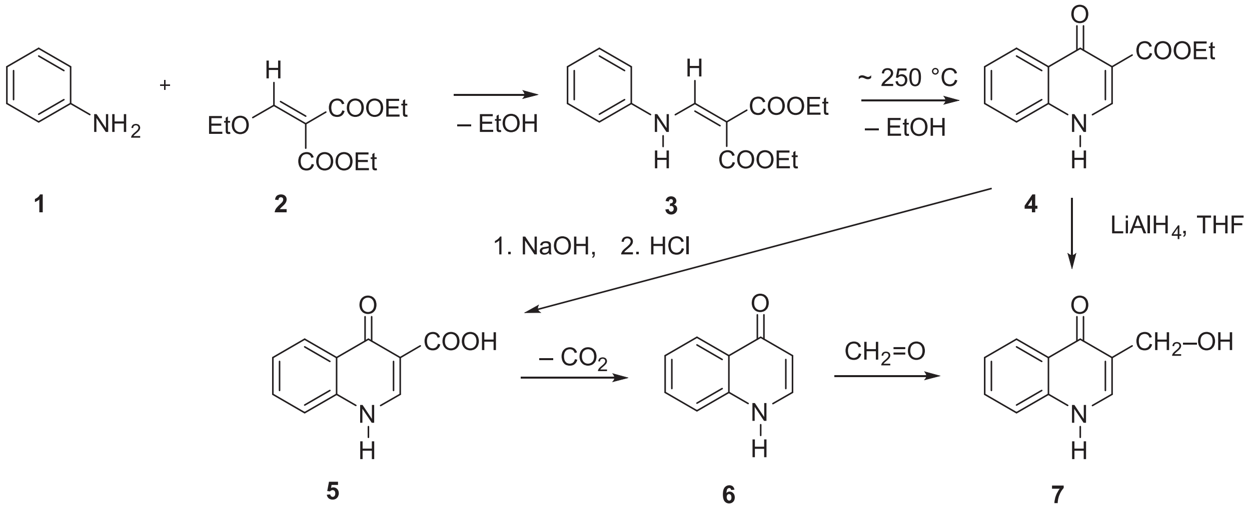

Scheme 2: Preparation of 3-hydroxymethyl-1,4-dihydro-4-oxoquinoline **7**.

References

Andriole VT (2000) The Quinolones. 3rd ed., Academic Press, San Diego, 2000, 518 pp.

Baekeland LH (1909) Method of making insoluble products of phenol and formaldehyde, US patent 942699, issued December 7, 1909.

Bajpai P, Agrawal PK, Vishwanathan L (1982) J. Sci. Ind. Res. 41(3): 185–194.

Broghammer H (1967) Mediz. Welt 17: 1091–1097.

Fulop F, Vamos E, Zadori D, Toldi J, Vecsei L (2009) Curr. Med. Chem. 16(36): 4828–4842.

Gellert M, Mizuuchi K, O'Dea MH, Nash HA (1976) Proc. Natl. Acad. Sci. U.S.A. 73, 3872–3876.

Goldworthy J, Ross WJ, Verge JP (1982) Eur. Pat. Appl., 55068 (30 Jun 1982), Chem. Abstr. 97: 162848, 1982.

Gootz TD, Brighty KE (1996) Med. Res. Rev. 16: 433–486.

Milata V, Claramunt RM, Elguero J, Zálupský P (2000) Targets in Heterocyclic Systems 4: 167–203.

Moncol J, Segla P, Miklos D, Mazur M, Melnik M, Glowiak T, Valko M, Koman M (2006) Polyhedron 25: 1561–1566.

Nicholson JR, Singh G (1989) Tetrahedron 45(3): 889–908.

Szalardy L, Zadori D, Toldi J, Fulop F, Klivenyi P, Vecsei L (2012) Curr. Topics Med. Chem. 12(16): 1797–1806.

Turski MP, Turska M, Paluszkiewicz P, Parada-Turska J, Oxenkrug GF (2013) Int. J. Tryptophan Res. 6: 47–55.

Wang JC (1985) Annu. Rev. Biochem. 54: 665–697.

Zubkov VO, Benzugly PO, Taran KA, Kamenetskaya OL, Silayeva LF (2003) Visnik Farmatsii 4: 3–6.

sciendo

Steam explosion of wood particles from fibreboard and particle board with indirect control by enzymatic hydrolysis

Andrej Pažitný

Pulp and Paper Research Institute, Dúbravská cesta 14, 841 04, Bratislava, Slovak Republic
pazitny@vupc.sk, ORCID: Andrej Pažitný 0000-0003-2269-953X

Abstract: Pretreatment of particles obtained from lignocellulosic materials by steam explosion with indirect control by enzymatic hydrolysis has been studied. The dendromass pretreatment model has been applied for recycled fibreboard and particle board based on softwood. Their structure and chemical composition partly predetermine these lignocellulosic materials consisting of a mixture of spruce and fir particles also for bioethanol production. Optimum steam explosion temperature of 205 °C was determined based on the concentration of total monosaccharides — glucose, xylose and arabinose, among all experimentally prepared hydrolysates. This corresponds to basic conditions for fine disintegration of biomass to lignocellulosic structure with good holocellulose accessibility. Particles obtained from fibreboard and particle board primarily consisting of softwood without steam explosion pretreatment provide relatively low cellulose accessibility for commercial enzymes activity while monosaccharides concentration is partly reduced because of torrefaction at high temperatures. The concentration of monosaccharides in hydrolysates was determined for original sample and each steam explosion temperature. Based on the steam explosion conditions, the effect of severity factors was investigated to find optimum pretreatment conditions to increase accessibility of softwood cellulose and hemicelluloses. The identified optimum severity factor R_O = 4.09 matches the optimum steam explosion temperature of 205 °C and the residence time of 10 minutes.

Keywords: biofuel industry, dendromass, fibreboard, particle board, severity factor, steam explosion

Introduction

Middle density fibreboards (MDF) and particle boards (PB) are the most produced wood based panels for furniture industry (Irle and Barbu, 2010). Generally, fibreboards and particle boards based on softwood are very useful materials also in building industry (Lühr et al., 2018). European production of wood chips and particles for MDF and PB boards manufacturing was about 86 million m^3 in 2018 which is 15 % of predicted wood consumption in 2020. From this amount, about 45 million m^3 of PB were produced in 2018. According to the FAO, it is assumed that wood consumption for energy generation in the European Union will grow from 346 million m^3 in 2010 to 573 million m^3 in 2020 and could reach as much as 752 million m^3 in 2030 (Moskalik and Gendek, 2019). Slovak republic participates with the production of about 830 thousand m^3 of chips and 630 thousand m^3 of particle boards. Urea-formaldehyde (UF), melamine-urea-formaldehyde (MUF), and melamine-urea-formaldehyde resins combined with a phenolic resin (MUPF) for external environment have been used for the production of fibreboards and particle boards considering the humidity of the environment of their use. Formaldehyde used for resin condensation is gradually released from boards during their lifetime. Formaldehyde is a colourless, highly toxic, and flammable gas. It is slightly heavier than air at room temperature and its releasing, especially from furniture boards, is strictly monitored. Just the amount of formaldehyde included in waste agglomerated boards significantly reduces the possibility of their recycling (Ihnát et al., 2017).

However, after a few decades of using fibreboards and particle boards their end-of-life comes and wood waste is formed. The used waste wood based panels are classified among municipal waste which may not be put on landfills but should be recycled or energy utilised. In general, recycling of wood waste is difficult due to the presence of harmful chemicals contained both in glue used during the manufacturing process (Risholm-Sundman and Vestin, 2005) and in additives originally protecting it from moisture and wood decaying fungi, increasing its fire resistance and so on (Erbreich 2004). There are also efforts to use wood waste in combination with other organic waste, e.g. with polyurethane since urea-formaldehyde resin is the main synthetic component in the fibreboard and particle board production and the obtained composite panels containing a certain amount of urea-formaldehyde resin and polyurethane show good mechanical properties (Liu et al., 2019). Additionally, researchers in our work group assume that the amounts of urea-formaldehyde resin from waste fibreboard and particle board materials gradually reduce after boiling water treatment due to its hydrolysis and the obtained materials with reduced urea-formaldehyde resin are suitable for the production of recycled and agglomerated materials (Ihnát et al., 2017; Ihnát et al., 2018). Recycled fibreboards can also be combined with other biomass species like straw pulp to prepare insulating fibreboards (Ihnát et al., 2015).

In Slovakia, commonly available softwood (Petráš et al., 2019) is used for the production of agglomerated materials such as MDF and PB, especially spruce. There often are combinations of spruce with deciduous trees, mainly beech. Their ratio and resulting composition are subject to availability of natural lignocellulosic sources. In the past, PB was produced mainly from deciduous trees – beech trees with a small addition of other ones (V. Ihnát, personal communication). Such lignocellulosic materials have considerably high holocellulose content and thus the particle boards and fibreboards contained a considerable amount of cellulose since they were produced from natural lignocellulosic materials (Arévalo and Peijs, 2016). Lignocellulosic materials are the most widespread natural form of cellulose, which is the most common biopolymer on Earth. Its annual worldwide production is estimated to be up to 10^{10} tonnes (Alvira et al., 2010; Sánchez and Cardona, 2008). Many research activities refer to thermo-mechanical or thermo-hydro-mechanical refining processes that can be optimised and applied in particle boards and fibreboards refining pretreatment (Xing et al., 2008). Optimal conditions can result in structural recalcitrance reduction and enhanced cellulose accessibility. These facts can be generalised for all lignocellulosic biomass species such as wheat straw, beech sawdust, etc. (Pažitný et al., 2019a; Pažitný et al., 2019b). Steam explosion is such an alternative (Yin et al., 2007). This pretreatment process can be controlled indirectly by enzymatic hydrolysis which is a very useful process common in industrial technologies (Pažitný et al., 2019a). Numerous experiments of enzymatic hydrolysis on bioconversion of pretreated sugarcane bagasse have been studied (Patel et al. 2017). The main advantage of enzymatic hydrolysis performance is also obtaining information about the hydrolysates content. This can vary significantly depending on biomass species, stiffness of starting material, and enzymatic hydrolysis conditions (Gigac et al., 2017).

Materials and Methods

Materials

Two types of recycled holocellulose sources: recycled fibreboards (Kronospan Mielec Ltd. Co., Poland) and particle boards (Bučina Zvolen JSC, Slovak Republic) were used. The raw material was recovered as waste from these lignocellulosic materials. Cellic CTec3 was used as a ready-to-use stabilised enzyme complex supplied by Novozymes A/S (Bagsværd, Denmark) for lignocellulosic raw material consumption to fermentable monosaccharides. The enzyme activity was measured to be 1.700 BHU (Biomass Hydrolysis Units)/g product in our laboratory.

Preparation of wood chips from waste particle boards

Initial destruction of large dimension materials, thickness of 18 mm, was carried out by cutting to smaller pieces of approximately 100 mm × 100 mm. Disintegration of waste particle boards glued with UF adhesives was carried out on a wet (soaking in water/cooking) basis employing a process provided by our workplace (Ihnát et al., 2017). Samples of 100 × 100 mm particle boards bonded with UF glues without surface foils on either side were dipped/soaked and cooked in water and weighed to determine the water absorbance. The samples were soaked for 48 hours in cold water and subsequently cooked for 180 minutes under stirring. The samples were disintegrated freely into individual particles after 180 minutes of cooking. Thus prepared samples were disintegrated and dried at 105 °C and particles obtained were sieved to fractions. Distribution of the prepared particles was determined by the laboratory sieving after drying at 105 °C, whereas the prepared particles were dried and sieved at pilot plants.

Preparation of wood fibre from waste MDF boards

Waste MDF based on UF resins was obtained from old furniture based on MDF boards. It was destructed to parts with edges of not more than 5 cm and fibre was prepared according to the process described in our previous paper (Ihnát et al., 2018). Particles of MDF were cooked at constant stirring in water for 3 minutes until the relative humidity of at least 45 % was achieved. The particles were hydro-mechanically defibered by wet milling on the Sprout Waldron (Sprout, Waldron & Co., Inc., USA) at the minimum temperature of 80 °C.

Steam explosion

The prepared samples of recycled fibreboards and particle boards were impregnated with fresh water so that the final moisture content of samples before the steam explosion was at least 85 % w/w. That is the amount of water in which a sample was soaked prior to its pretreatment and which was calculated to be 15 % w/w of the used lignocellulosic material.

The samples were soaked in water at 20 °C for at least 1 hour prior to steam explosion pretreatment. Quick determination of dry matter in the samples was performed on a moisture analyser Denver IR35 that uses infrared sample heating. The samples (100 g o.d.) were finally pretreated in a 2 L stainless steel batch reactor for steam explosion (Amar Equipments Pvt. Ltd., India). The reactor was used for steam reactions at three different temperatures (185 °C, 205 °C and 235 °C). Retention time of each thermo-hydro-mechanical experiment with the recycled lignocellulosic materials (steam explosion – STEX) was 10 minutes.

Enzymatic hydrolysis

Enzymatic hydrolysis (EH) of original particles and those pretreated with Cellic Ctec3 at a dose of 15 % w/w (g of Cellic Ctec3/100 g of cellulose) was carried out at 50 °C, pH = 5.0 for 96 hours and 12.5 % w/w of particles. The pH value was adjusted continuously during the process using 0.1 N sulphuric acid and 0.1 N sodium hydroxide. The hydrolysate samples were collected after 24, 48, 72 and 96 hours. The procedure of cellulose decomposition is well described (Whistler and Smart, 1953) by the chemical equations scheme represented by Eq. (1).

$$\begin{aligned}\text{natural cellulose} \rightarrow \text{linear cellulose} \rightarrow \\ \rightarrow \text{cellobiose} \rightarrow \text{glucose}\end{aligned} \qquad (1)$$

HPLC analysis

Concentration of monosaccharides was determined using the procedure of the National Renewable Energy Laboratory (NREL 2008; Sluiter et al., 2011). Monosaccharides (glucose, xylose and arabinose) were determined in hydrolysates by the HPLC (High Performance Liquid Chromatography) method using a Rezex ROA (organic acid) H^+ column. The mobile phase was 0.005 N sulphuric acid at the flow of 0.5 $mL \cdot min^{-1}$ and the temperature was set to 30 °C. Chromatography data were processed by the software Clarity version 5.3.0.180 (DataApex Ltd., Czech Republic).

Results and Discussion

Recycled fibreboards and particle boards as perspective substrates in 2G bioethanol production

A good model for dendromass behaviour in partial processes of biofuel production can be obtained using of recycled fibreboards and particle boards due to their high holocellulose content. The mentioned substrates are based mostly on spruce and, in lower extent, also on beech; holocellulose content in these natural materials ranges from 71 % (Kurth and Ritter, 1934; Bodîrlău et al., 2012) to 85 % (Gawron et al., 2011). Among the recycled fibreboards, MDF boards are very often used in furniture industry. However, these contain also resin and other additives that are blended with the fibres (Piekarski et al., 2014). There are no reliable literary sources referring to 2G bioethanol produced from fibreboards and particle boards and this work has the ambitions to change this.

Steam explosion of recycled fibreboards and particle boards as a pretreatment method and its evaluation

Various methods of pretreatment and their evaluation have been described in our previous papers as well as in other scientific papers (Pažitný et al., 2019a, 2019b; Kokta and Ahmed, 1998; Simangunsong et al., 2018). In this work, steam explosion of recycled fibreboards and particle boards at 185 °C, 205 °C and 235 °C was studied. Samples prepared for the steam explosion experiment were soaked in water at 20 °C for at least 1 hour and then they were subjected to steam explosion at appropriate temperatures. The corresponding severity factors are listed in Table 1.

Tab. 1. Effect of pretreatment process temperature on the severity factor at constant retention time of 10 minutes.

Steam explosion temperature (°C)	Retention time (minutes)	Severity factor
185	10	3.50
205	10	4.09
235	10	4.97

The severity factor computation for corresponding temperatures and constant retention time was based on the integral form of the equation for severity factor determination (Eq. (2)) introduced in other scientific papers (Hashemi et al., 2019; Batista et al., 2019).

$$R_O = \int_0^t exp\left[\frac{T_r - T_b}{14.75}\right] dt \qquad (2)$$

where R_O is the severity factor, T_r reaction temperature (°C), T_b base temperature (100 °C), t retention time in biomass hydrothermal reaction (minutes), 14.75 is an empirical temperature value based on the conventional activation energy assuming first order kinetics ($kJ \cdot mol^{-1}$). Eq. (2) can be written in a simplified form (Pažitný et al., 2019a) and it quantifies as a reaction coordinate for steam explosion. Table 1 clearly shows the increasing trend of the severity factor depending on the temperature increase.

Tab. 2. Availability of samples obtained from enzymatic hydrolysis of particles prepared by steam explosion.

Sample type	**Steam explosion temperature (°C)**	**Availability of samples from enzymatic hydrolysis**
Particle boards	Without steam explosion	Available
Fibreboards	Without steam explosion	Unavailable
Particle boards	185	Available
Fibreboards	185	Unavailable
Particle boards	205	Unavailable
Fibreboards	205	Available
Particle boards	235	Unavailable
Fibreboards	235	Available

Several enzymatic hydrolysis experiments with samples obtained from steam explosion were excluded from the analysis due to the difficult removal of hydrolysates and problems with torrefaction of the lignocellulosic material at the steam explosion temperature of 235 °C, mainly in case of particles obtained from particle boards. The most common material for particle boards and fibreboards production in our region is spruce wood which can be torrefied at temperatures ranging from 230 °C to 290 °C (Manouchehrinejad and Mani, 2018). However, steam explosion of particles based on fibreboards at 235 °C was successful and enzymatic hydrolysis was performed with removable hydrolysate. Availability of samples obtained from enzymatic hydrolysis is shown in Table 2.

Elution time of all monosaccharides (Table 3) was equal for each sample and at all times of hydrolysates sampling (Fig. 1 a) – d)).

Tab. 3. Retention time of analysed monosaccharides obtained from enzymatic hydrolysis.

Analysed component	**Elution time (minutes)**
Glucose	11.80 ± 0.01
Xylose	12.60 ± 0.02
Arabinose	13.85 ± 0.02

Figure 1 a) shows an HPLC chromatogram overlay of hydrolysates obtained from the particles without steam explosion pretreatment. It confirms

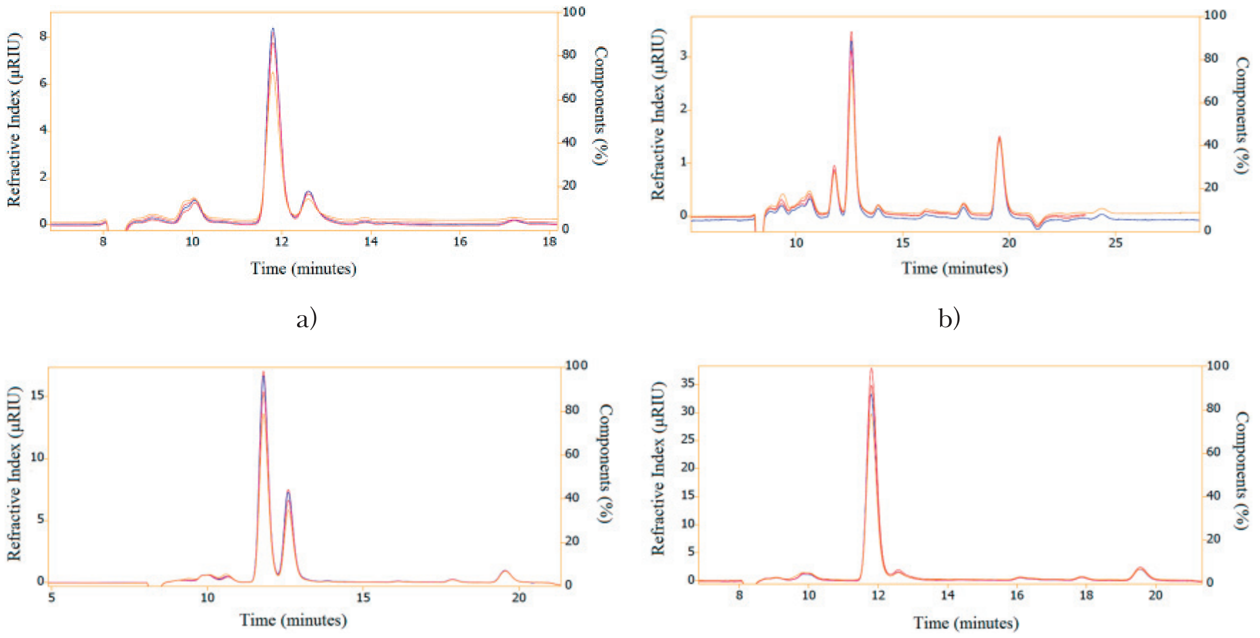

a)

b)

c)

d)

Fig. 1. HPLC chromatogram overlays of hydrolysates obtained from particles without steam explosion pretreatment *(a) particle boards* and pretreated by steam explosion at different temperatures, *b) particle boards, 185 °C, c) fibreboards, 205 °C, d) fibreboards, 235 °C)*, elution time of analysed monosaccharides is shown in Table 3 *(EH 24 hours – orange, EH 48 hours – red, EH 72 hours – blue, EH 96 – light red).*

the characteristic presence of glucose and lower concentration of xylose and arabinose expected based on lower holocellulose accessibility without pretreatment (Pažitný et al., 2019b). Figure 1 b) — d) shows HPLC chromatograms of hydrolysates obtained from the particle boards or fibreboards pretreated by steam explosion. In Figure 1 a), c) and d), the most significant peak belongs to the glucose monomer which indicates high content of accessible cellulose. It was found that hydrolysate obtained from fibreboards pretreated by steam explosion at 235 °C contains the highest proportion of the glucose monomer based on the highest signal (Fig. 1 d)). Thus, the best splitting of recalcitrant structure and the most accessible fibreboard cellulose are at the highest used temperature of steam explosion which is very close to the torrefaction temperature (Manouchehrinejad and Mani, 2018). Additionally, Figure 1 b) shows higher signal for the xylose monomer compared to that for the glucose monomer which is probably caused by the lower pretreatment temperature. The holocellulose decomposition mechanism during thermo-hydro-mechanical refining processes is known. The rate of this decomposition is higher for hemicelluloses, much lower for cellulose and the lowest for lignin (Sandberg et al., 2013). This implies that the cellulose decomposition requires higher temperatures.

It should be noted that Figure 1 a) — d) gives qualitative analysis of monosaccharides in hydrolysates — glucose, xylose and arabinose monomers. However, the recorded chromatograms show several smaller peaks that are difficult to analyse due to their overlap. As expected, the concentration of monosaccharides recovered in the liquid phase is very low for non-pretreated samples and it increases as shown by leaps and bounds for pretreated samples, which is in accordance with our previous results (Pažitný et al., 2019a). It is also clear that steam explosion temperature of 185 °C is insufficient to achieve splitting of recalcitrant structure of the lignocellulosic material used as the signal for the refractive index for glucose is relatively low (approximately 3 µRIU).

Figure 2 a) — b) gives information about the concentration of individual monosaccharides in hydrolysates. It is shown that the highest concentration of

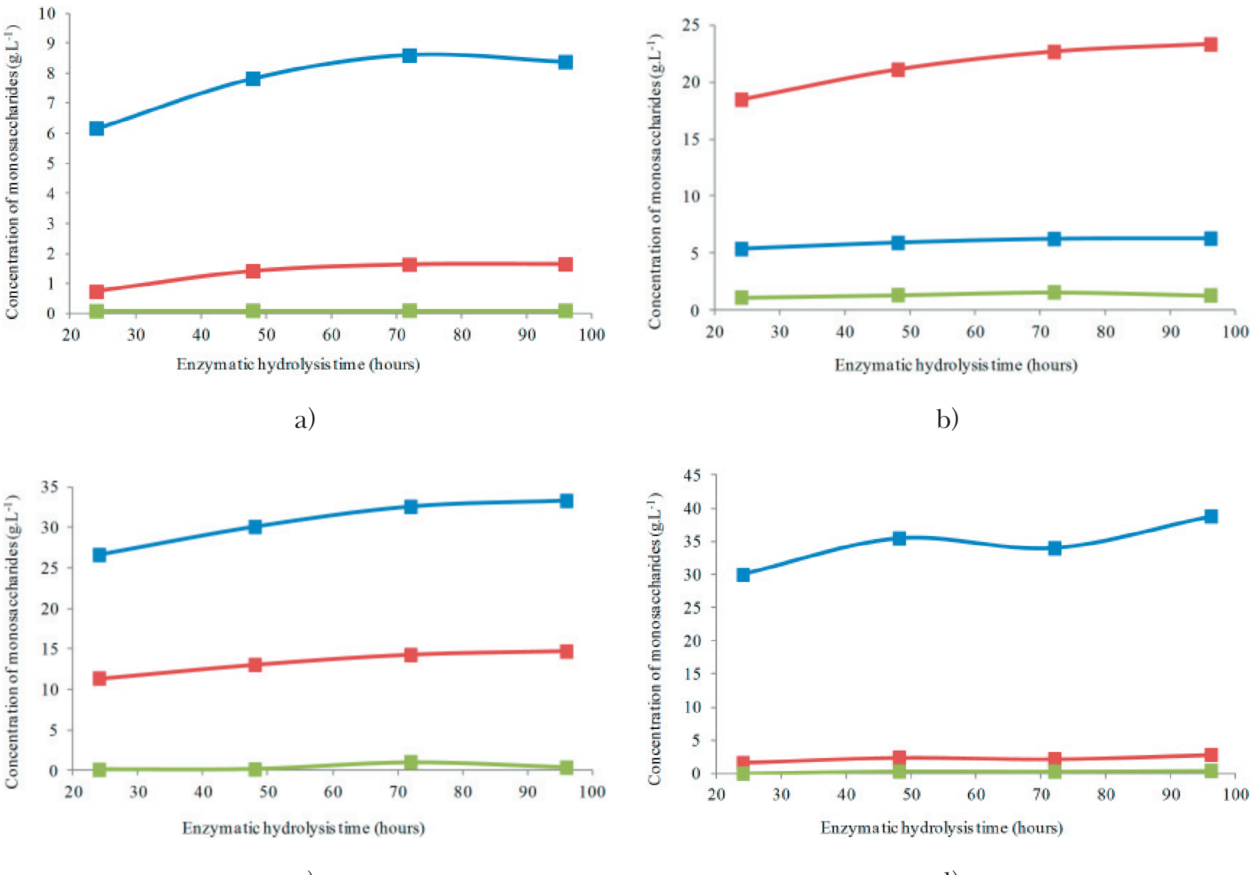

a)

b)

c)

d)

Fig. 2. Time-dependence of monosaccharides concentration *(glucose – blue, xylose – red, arabinose – green)* for hydrolysates obtained from particles without steam explosion pretreatment *(a) particle boards)* and pretreated by steam explosion at different temperatures *(b) particle boards, 185 °C, c) fibreboards, 205 °C, d) fibreboards, 235 °C).*

glucose (38.8 g·L^{-1}) results in steam explosion of fibreboard particles at 235 °C. However, the highest total concentration of monosaccharides (42 g·L^{-1}) is provided by steam explosion of fibreboard particles at 205 °C. It should be added that this pretreatment temperature of lignocellulosic material based on wood was identified as the optimum because higher pretreatment temperatures enhance the production of fermentation inhibitors (Stankovská et al., 2018) which are not suitable for further treatment in second generation biofuel production. As mentioned above, analogically to chromatograms evaluation, the highest concentration of identified pentose – xylose and arabinose was found for steam explosion pretreatment of particle boards at 185 °C. The maximum concentration of xylose (23.3 g·L^{-1}) and arabinose (1.58 g·L^{-1}) was achieved after 96 hours and after 72 hours of enzymatic hydrolysis, respectively.

The obtained results on hydrolysates composition can help to formulate input mixture of raw materials suitable for the production of second generation liquid biofuels. Based on these results, fibreboard seems to be a more suitable lignocellulosic material with relatively low severity factor R_O = 4.09 (pretreatment temperature of 205 °C, retention time of 10 minutes).

Conclusions

HPLC analysis was used to characterise hydrolysed lignocellulosic materials based on dendromass, the materials were subjected to mechanical, hydro-mechanical and thermo-hydro-mechanical refining processes. Dramatic changes in the basic composition of particles based on fibreboard and particle boards were observed when thermo-hydro-mechanical pretreatment – steam explosion, was used. Enzymatic hydrolysis was used as an indirect control of the pretreatment process.

Analysis of hydrolysates from enzymatic hydrolysis showed that the optimum pretreatment process was achieved by steam explosion of fibreboard particles at 205 °C, which corresponds to the severity factor (R_O) of 4.09 (pretreatment temperature of 205 °C, retention time of 10 minutes). For this temperature, the highest concentration of total monosaccharides (42 g·L^{-1}) with relatively high proportion of glucose (38.8 g·L^{-1}) was obtained. Significantly higher pretreatment temperatures enhance the concentration of fermentation inhibitors resulting from reduced concentration of monosaccharides at the pretreatment temperature of 235 °C. This temperature is also very close or even corresponds to the torrefaction temperature of the lignocellulosic materials studied. However, this pretreatment temperature provided the highest concentration of glucose in case of steam explosion of particles based on fibreboards. In contrast, the concentrations of xylose and arabinose were reduced. The maximum concentration of xylose (23.3 g·L^{-1}) and arabinose (1.58 g·L^{-1}) were obtained in case of steam explosion pretreatment of particle boards at 185 °C after 96 hours and after 72 hours of enzymatic hydrolysis, respectively.

The hydrolysates composition results can help in the formulation of the input mixture of raw materials suitable for the production of second generation liquid biofuels as well as in the field of enzymology and wood processing industry.

Acknowledgements

This work was supported by the Slovak Research and Development Agency under the Contract no. APVV-18-0240.

References

Alvira P, Tomás-Pejó E, Ballesteros M, Negro MJ (2010) Bioresource Technology 101: 4851–4861.

Arévalo R, Peijs T (2016) Composites: Part A 83: 38–46.

Batista G, Souza RBA, Pratto B, Santos-Rocha MSRD, Cruz AJG (2019) Bioresource Technology 275: 321–327.

Bodîrlău R, Teacă CA, Resmeriţă AM, Spiridon I (2012) Cellulose Chemistry and Technology 46: 381–387.

Erbreich M (2004) Dissertation, Universität Hamburg.

Gawron J, Grześkiewicz M, Zawadzki J, Zielenkiewicz T, Radomski A (2011) Wood Research 56: 213–220.

Gigac J, Fišerová M, Stankovská M, Pažitný A (2017) Wood Research 62: 919–930.

Hashemi SS, Karimi K, Mirmohamadsadeghi S (2019) Energy 175: 545–554.

Ihnát V, Borůvka V, Babiak M, Lübke H, Schwartz J (2015) Wood Research 60: 441–450.

Ihnát V, Lübke H, Russ A, Borůvka V (2017) Wood Research 62: 45–56.

Ihnát V, Lübke H, Russ A, Pažitný A, Borůvka V (2018) Wood Research 63: 431–442.

Irle M, Barbu MC (2010) In: Thoemen H, Irle M, Sernek M (Ed) Wood-Based Panels. An Introduction for Specialist, Brunel University Press, London.

Kokta BV, Ahmed A (1998) In: Young RA, Akhtar M (Ed) Environmentally friendly technologies for the pulp and paper industry (pp 191–214). John Wiley & Sons, Inc., New York.

Kurth EF, Ritter GJ (1934) Journal of the American Chemical Society 56: 2720–2723.

Liu X, Pang Y, Cui T, Li Y, Xi E, Liu X, Li Q, Wan H, Mao A (2019) American Journal of Agriculture and Forestry 7: 146–150.

Lühr C, Pecenka R, Budde J, Hoffmann T, Gusovius HJ (2018) Industrial Crops & Products 118: 81–94.

Manouchehrinejad M, Mani S (2018) Biomass and Bioenergy 118: 93–104.

Moskalik T, Gendek A (2019) Forests 10: 1–14.

National Renewable Energy Laboratory (NREL) (2008) Chemical analysis and testing laboratory analytical procedures: LAP-002, LAP-003, LAP-004. NREL, Golden, Colorado, USA.

Patel H, Chapla D, Shah A (2017) Renewable Energy 109: 323–331.

Pažitný A, Russ A, Boháček Š, Stankovská M, Ihnát V, Šutý Š (2019a) Wood Research 64: 437–448.

Pažitný A, Russ A, Boháček Š, Stankovská M, Šutý Š (2019b) Wood Research 64: 13–24.

Petráš R, Mecko J, Krupová D, Slamka M, Pažitný A (2019) Wood Research 64: 205–212.

Piekarski CM, Francisco ACD, Luz LMD, Alvarenga THDP, Bittencourt JVM (2014) Cerne 20: 409–418.

Risholm-Sundman M, Vestin E (2005) Holz als Roh- und Werkstoff 63: 179–185.

Sánchez OJ, Cardona CA (2008) Bioresource Technology 99: 5270–5295.

Sandberg D, Haller P, Navi P (2013) Wood Material Science and Engineering 8: 64–88.

Simangunsong E, Ziegler-Devin I, Chrusciel L, Girods P, Wistara NJ, Brosse N (2018) Waste and Biomass Valorization (articles not assigned to an issue): 1–9.

Sluiter A, Hames B, Ruiz R, Scarlata C, Sluiter J, Templeton D, Crocker D (2011) Technical Report NREL/TP-540-42618. National Renewable Energy Laboratory (NREL), Golden, Colorado, USA.

Stankovská M, Fišerová M, Gigac J, Pažitný A (2018) Cellulose Chemistry and Technology 52: 815–822.

Whistler RL, Smart CL (1953) Journal of American Chemical Society 75: 1916–1918.

Xing C, Wang S, Pharr GM, Groom LH (2008) Holzforschung 62: 230–236.

Yin S, Wang S, Rials TG, Kit KM, Hansen MG (2007) Wood and Fiber Science 39: 95–108.

sciendo

Application of milk thistle (*Silybum marianum*) in functional biscuits formulation

Veronika Bortlíková, Lukáš Kolarič,
Peter Šimko[*]

Slovak University of Technology in Bratislava, Faculty of Chemical and Food Technology,
Institute of Food Science and Nutrition, Radlinského 9, 812 37 Bratislava, Slovak Republic
[*]*qsimko@stuba.sk*

Abstract: Due to the substantial protective effects of milk thistle to liver against various chemical compounds, a new healthy cereal product replacing wheat flour with milk thistle seed flour in the range of 5; 10; 15; 20; 25 and 30 % has been studied. As it has been found, milk thistle seed flour is a good source of total dietary fibre, proteins, mineral compounds and fats. During the experiments, effects of wheat flour replacement on technological properties of the dough were studied using Mixolab characteristics. From the results it can be stated that milk thistle seed flour replacement led to a decrease in water absorption and stability of dough. After baking, physical, mechanical, colour and sensorial properties of the biscuits were studied. The results have shown that even a 10 % replacement results in a significant difference at $p < 0.05$ in measured parameters compared to ones. However, it has been calculated that statistically insignificant replacement of wheat flour with milk thistle seed flour is up to 9.3 % with quality and sensorial parameters of the biscuits equal to those prepared from 100 % wheat flour. Thus, production of functional biscuits at these conditions is fully possible.

Keywords: biscuits, functional foods, milk thistle, Mixolab, sensory analysis, silymarin, texture

Introduction

Over the last decades, research has proved that diets rich in fruits and vegetables are protective against the risk of some types of cancer. Several medicinal herbs have received great attention due to their wide range of pharmacological effects and also for their cancer chemopreventive activity (Ramasamy and Agarwal, 2008). Liver cancer is considered as the sixth most common cancer and the second leading cause of cancer deaths around the world (Mohammadian et al., 2018). Over 840,000 new cases of liver cancer were reported in 2018 and it was the most frequently diagnosed type of cancer in 13 countries, especially in Mongolia, Egypt or Gambia (Bray et al., 2018). Thus, there is no doubt about the increasing occurrence of liver cancer in the world. From the viewpoint of food technology, functional foods are of great interest due to their positive effects on consumer health. Functional foods are foods and their components with health benefits beyond basic nutrition; they help in maintaining health and thereby reducing the risk of diseases. Also evidence proving an association between functional foods and cancer has been reported. Flavonoids have several important biological roles associated to cancer risk. *In vitro* and animal model systems indicated that flavonoids influence signal transduction pathways, stimulate apoptosis and prevent inflammation and proliferation in human cancer cell lines (Aghajanpour et al., 2017).

Milk thistle (*Silybum marianum*) seeds (MTS) have been used for more than 2000 years as an effective medicament for liver and biliary disorders (e.g. cirrhosis, chronic hepatitis, environmental contaminants exposure) and it is one of the most common botanical supplements in the world used for therapeutic purposes (Albassam et al., 2017). According to Karkanis et al. (2011) milk thistle is an important medicinal crop in Europe especially in Poland, a significant European producer of MTS and medicines derived from it. MTS has recently become more significant in North America. According to El-haak et al. (2015), MTS contains beneficial compounds such as proteins, saccharides (especially crude fibre), minerals and some phytochemicals – mainly flavonolignans, summarily called silymarin. The main roles of this compound are liver protection, improvement of hepatocytes rearrangement, prevention of lipid peroxidation, detoxification of liver, and antioxidant activity (Tabari et al., 2019). Dried extract of MTS contains approximately 60 % of silymarin (Radjabian et al., 2008). Moreover, MTS proteins have a high content of essential amino acids such as lysine, isoleucine, leucine, valine, and threonine, which are not present in wheat flour (WF) (Apostol et al., 2017a). Therefore, the application of milk thistle seed flour (MTSF) in cereal products could be beneficial due to its nutritional and health effects on consumer organism. In spite of these healthy properties, there is a lack of any information regarding the

Acta Chimica Slovaca, Vol. 12, No. 2, 2019, pp. 192–199, DOI: 10.2478/acs-2019-0027

application of MTS in biscuits. Shahat Mohamed et al. (2016) studied replacing WF with MTSF at levels of 3, 6 and 9 %. According to their results, the use of MTSF at 9 % did not influence the sensory properties, and therefore it is a promising way to produce low price functional bread. Apostol et al. (2017a) studied partially defatted MTSF and found that a 5 %, 10 % or even 15 % replacement of WF with MTSF did not negatively affect the rheological parameters of dough used for the production of superior bakery products.

The purpose of this research is to offer new functional food which may reduce the risk of cancer, especially liver cancer. Thus, the aim of this article was to study the effects of WF replacement with 5, 10, 15, 20, 25 and 30 % of MTSF on technological characteristics of dough and on organoleptic properties of the final product.

Materials and methods

Materials

WF (Good Mills Czech Republic s.r.o., type T530), saccharose (Korunný cukor, Slovakia), shortening (Palma a.s., Slovakia), sodium bicarbonate (Dr. Oetker s.r.o, Slovakia) and table salt (K+S Czech Republic a.s.) were purchased in a local market. MTS (Fytopharma a.s., Slovakia) was purchased in a local pharmacy. MTSF was obtained by grinding MTS using a grinder (Bosch, Germany). To obtain a uniform particle size, the MTSF was passed through a sieve with the particle size of 250 μm and stored at 4 °C in dark until usage.

Chemical composition of flours

Moisture content was determined by a modified method described by Oladunmoye et al. (2014). Temperature in the air oven was maintained at 130 °C for 60 min. Ash content was determined by Riley et al. (2006). Crude fat content was determined by a method described by Pereira et al., (2013). Protein content was set as total nitrogen content by the Kjeldahl procedure; a factor of 6.25 was used for nitrogen conversion to crude protein in MTSF and of 5.70 in WF (Apostol et al., 2017b). Total dietary fibre (TDF) content was determined using the Megazyme International TDF assay (Sun-Waterhouse et al., 2010). Reducing saccharides content was determined by the Luff-Schoorl method according to Marrubini et al. (2017). Total starch content was determined using the Ewers method measuring optical rotation (Kennedy et al., 1989).

Rheological properties of dough

Rheological behaviour of dough was monitored using Mixolab 2 (Chopin Technologies, France) applying the "Chopin+" protocol, in which Mixolab recorded changes of torque in five defined points as follows: C_1 — water absorption; C_2 — weakening of the protein based on mechanical stress at increasing temperature; C_3 — rate of starch gelatinization; C_4 — stability of the formed gel; C_5 — starch retrogradation during the cooling period (Švec and Hrušková, 2015). By application of the "Chopin S" protocol in Mixolab, three farinographic characteristics were measured (Kaur et al., 2016):

- dough development time (DDT); time between the first addition of water and the development of the dough's maximum consistency;
- dough stability (DS); difference in time between the point at which a top of the curve first intercepts 1.1 N · m and the point at which the top of the curves leaves the 1.1 N · m region;
- degree of softening (DoS); difference (expressed in Farinographic units — FU), between the height of the centre of the curve at the peak and the centre of the curve after 12 min.

Biscuits formulation

Biscuits were prepared according to Kohajdová et al. (2011). The basic biscuits recipe was: 200 g of fine WF, 106 g of saccharose, 53 g of shortening, 2.2 g of sodium bicarbonate, 1.78 g of table salt, and 24 cm^3 of water. This product was used as a reference for comparison purposes. Then, WF was replaced with MTSF at levels of 5, 10, 15, 20, 25 and 30 %. The cookies were round in shape and they were baked in an electric oven (Mora, Slovak Republic) at 180 °C for 8 min.

Physical properties of biscuits

Five random biscuits were taken after baking to measure their weight [g], thickness [mm], width [mm] and volume [cm^3]. The weight of the biscuits before and after baking was used to calculate weight loss (Ho and Abdul Latif, 2016). Spread ratio was calculated from the ratio of spread to thickness (Sindhuja et al., 2005). The volume was determined by the displacement method of millet seeds and specific volume [cm^3/100 g] was calculated as the ratio of volume to weight (Freitas et al., 2014).

Mechanical properties of biscuits

Texture analysis of the biscuits was carried on a TA.TX.plus Texture Analyzer (Stable Micro Systems, Godalming, Surrey, U.K.). The biscuits were fractured using the three-point bending rig probe (HDP/3PB) with a 5 kg load cell. Experimental conditions were as follows: pre-test speed — 1.0 mm/s, test speed — 3.0 mm/s, post-test speed — 10 mm/s, distance between supports — 30 mm and trigger force — 50 g. The mean maximum value was recorded as hardness [g] and the mean distance compressed before breaking value as fracturability [mm].

Analysis of colour

Colour of the flour mixture formulations and the upper surface colour of the biscuits were measured using a UV-VIS spectrophotometer Cary 300 (Agilent Technologies, USA); the colour itself was evaluated using the CIELAB coordinate system. The parameters measured were: L^* (lightness factor, 0 = black, 100 = white), a^* ($-a^*$ = green, $+a^*$ = red) and b^* ($-b^*$ = blue, $+b^*$ = yellow). The total colour difference (ΔE) between the reference and the flour mixtures was calculated by Apostol et al. (2017a):

$$\Delta E^*_{ab} = \sqrt{(\Delta L^*)^2 + (\Delta a^*)^2 + (\Delta b^*)^2} \tag{1}$$

Sensory evaluation

The biscuits were subjected to sensory evaluation using nine trained panellists, men and women between the age of 22—24 years from the University community. The biscuits were analysed for their taste, aroma, crispiness, colour, hardness and overall visual acceptability on a hedonic scale going from 0 (dislike extremely) to 10 points (like extremely) (Pagès et al., 2007; Chauhan et al., 2016). Overall acceptability was expressed in percentages in the range of 0—100 %.

Statistical analysis

All measurements were performed in triplicate at the minimum sample amount and expressed as an average ±standard deviation. The data were subjected to the Student's test using Microsoft Office Excel 365. The obtained values were significantly different at $p < 0.05$. Using the Microsoft Office Excel 365, a correlation analysis was performed to determine the connection between rheological properties of dough and technological properties of supplemented biscuits, which was expressed through the Pearson correlation coefficient (*r*). The p value of highest statistically insignificant replacement in terms of overall acceptability, i.e. statistically insignificant ideal replacement, was determined by comparison.

Tab. 1. Chemical composition of WF and MTSF [%].

Chemical component	WF	MTSF
Moisture	8.9 ±0.10	6.0 ±0.10
Fat	2.0 ±0.00	32.9 ±0.10
Total dietary fibre	2.5 ±0.10	42.1 ±0.50
Starch	67.7 ±0.00	3.1 ±0.10
Reducing saccharides	0.4 ±0.00	1.8 ±0.10
Ash	0.5 ±0.00	5.5 ±0.20
Protein	12.4 ±0.40	20.1 ±0.90

All values are expressed as mean ±SD, n = 3; WF — wheat flour, MTSF — milk thistle seed flour.

Results and Discussion

Chemical composition of flours

Chemical composition of both flours is shown in Table 1.

The results confirmed that MTSF is a valuable source of fat, protein, and dietary fibre. In comparison to WF, MTSF contains a higher level of

Tab. 2. Rheology characteristics of dough composed of WF alone (column 1) and MTSF/ WF blends in range of 5, 10, 15, 20, 25, and 30 % (columns 2, 3, 4, 5, 6, 7).

Rheology parameters	1	2	3	4	5	6	7
WA [%]	57.3 ±0.17	56.3 ±0.00*	55.7 ±0.08*	54.0 ±0.41*	53.1 ±0.05*	51.6 ±0.17*	51.2 ±0.08*
C_1 [N·m]	1.12 ±0.00	1.09 ±0.01*	1.07 ±0.00*	1.07 ±0.00*	1.13 ±0.01	1.09 ±0.02	1.11 ±0.04
C_2 [N·m]	0.55 ±0.01	0.45 ±0.01*	0.31 ±0.01*	0.25 ±0.01*	0.30 ±0.01*	0.28 ±0.01*	0.28 ±0.01*
C_3 [N·m]	2.00 ±0.04	1.66 ±0.02*	1.50 ±0.01*	1.41 ±0.03*	1.46 ±0.02*	1.35 ±0.02*	1.37 ±0.02*
C_4 [N·m]	1.99 ±0.04	1.54 ±0.02*	1.48 ±0.02*	1.44 ±0.05*	1.55 ±0.02*	1.44 ±0.01*	1.31 ±0.02*
C_5 [N·m]	3.15 ±0.06	2.59 ±0.04*	2.59 ±0.06*	2.54 ±0.05*	2.76 ±0.03*	2.69 ±0.04*	2.58 ±0.01*
DDT [min]	4.33 ±0.24	5.50 ±0.00*	6.00 ±0.00*	5.67 ±0.24*	6.33 ±0.24*	6.67 ±0.24*	5.83 ±0.48*
DS [min]	18.00 ±0.41	11.50 ±0.00*	8.83 ±1.93*	5.17 ±0.62*	5.50 ±0.41*	4.83 ±0.24*	4.50 ±1.41*
DoS [FU]	17.67 ±3.68	14.67 ±3.30	49.00 ±7.26*	72.67 ±1.25*	69.33 ±5.25*	76.67 ±8.96*	88.33 ±6.24*

All values are expressed as mean ±SD, n = 3, * indicates a statistically significant difference ($p < 0.05$).

WF — wheat flour, MTSF — milk thistle seed flour, WA — water absorption; C_1 — initial maximum consistence during mixing; C_2 — minimum value of torsion during mixing and initial heating; C_3 — maximum value (peak) of torsion during heating stage; C_4 — stability of hot starch paste; C_5 — difference between maximum torsion after the cooling period at 50 °C; DDT — dough development time; DS — dough stability; DoS — degree of softening fat, protein as well as TDF. However, Apostol et al. (2017b) determined the TDF content in partially defatted MTSF to be 27.2 % which is significantly lower than our results. According to El-haak et al. (2015), the contents of protein, lipids and total saccharides in the seeds are in the range of 19.1–30.0 %, 20.0–30.0 %, and 24.2–26.3 %, while the starch content is only 3.1 % and reducing saccharides content only 1.8 %, which means that TDF forms the biggest part of total saccharide content in MTSF. Also, ash content in MTSF is considerably higher compared to WF. From the results of chemical composition, it can therefore be stated that MTSF is a good source of TDF in biscuits.

Rheological properties of dough

Rheological properties of dough are provided in Table 2.

Monitoring of rheological properties of dough is very important for the overall technology to estimate mechanical properties of dough and to imitate its behaviour during its processing or even to anticipate the quality of the final product (Hadnađev et al., 2014). From the obtained data it can be clearly seen that increasing addition of MTSF decreased the absorption of water (WA) in dough. These results are in contrast with those of Shahat Mohamed et al. (2016), where WA level increased with the addition of MTSF; however, they are similar to those of Apostol et al. (2017a), where WA level decreased from 60.0 % (reference sample) to 58.1 % (15 % MTSF). As noted by Okuda et al. (2016), lower water content increases the dough kneading time. As it follows from Table 2, a 30 % replacement significantly decreased WA, thus it can be assumed that a larger volume of water will be needed to develop dough with the same properties in comparison with the reference. C_2 values, representing the weakening of protein network, decreased from 0.55 N·m to 0.25 N·m (15 % MTSF) and then remained at approximately constant value of 0.30 N·m indicating certain compatibility level of gluten and MTSF proteins during dough formation. C_3 values are connected to starch gelatinization. As shown in Table 1, MTSF is not a rich source of starch, therefore C_3 values tend to decrease during the replacement of WF. From this point of view, limiting replacement of WF with MTSF is approximately 10 % since C_4 and C_5 were not considerably affected by the WF replacement.

From Table 2, DDT of reference dough was 4.33 min while a 5 % MTSF addition increased this value to 5.50 min. At higher replacements, this time even reached 6 min. In general, the increase of DDT indicates that higher fibre content slows down the rate of hydration and the development of gluten (Kohajdová et al., 2011). These results correspond to the study of Shahat Mohamed et al. (2016), in which DDT of reference dough was 4.5 min and of the dough with a MTSF addition of 3, 6 and 9 % it was 6, 5 and 5.5 min, respectively.

As it follows from Table 2, DS values significantly decreased with the increase of MTSF addition. At large, stability of dough is attributed to protein poor in sulfhydryl groups, which normally causes dough softening or even degradation (Shahat Mohamed et al., 2016). The gluten network with is stronger and has higher resistance to shear stress at higher protein content (Kaur et al., 2016). Although MTSF contains high level of protein, higher level of fibre may weaken the gluten network. DoS increased almost five times due to WF replacement due to high fibre and fat content in MTSF, which can weaken the dough (Shahat Mohamed et al., 2016).

Physical properties of biscuits

Table 3 summarizes physical properties (weight, thickness, diameter, spread ratio, volume, speci-

Tab. 3. Physical properties of biscuits prepared from WF and WF/MTFS blends.

Level of MTSF addition	Weight after baking [g]	Thickness [mm]	Width [mm]	Volume [cm^3]	Specific volume [cm^3/100g]	Weight loss [%]	Spread ratio
0 %	7.61 ±0.35	7.62 ±0.30	47.88 ±0.47	10.60 ±0.49	139.31 ±4.97	13.27 ±0.53	6.29 ±0.24
5 %	7.39 ±0.37	8.10* ±0.21	47.13* ±0.31	10.60 ±0.49	143.53 ±5.71	13.05 ±0.33	5.82 ±0.17
10 %	7.47 ±0.30	7.05* ±0.11	47.75 ±0.78	11.20* ±0.40	150.16 ±6.75	13.64 ±0.67	6.77* ±0.18
15 %	7.07 ±0.34	7.34 ±0.30	48.08 ±0.11	11.80* ±0.40	167.15* ±7.39	13.77 ±0.51	6.56 ±0.25
20 %	6.86* ±0.10	6.69* ±0.25	47.62 ±0.69	11.80* ±0.40	172.17* ±6.82	14.52* ±0.58	7.12* ±0.19
25 %	6.61* ±0.30	8.85* ±0.33	47.72 ±1.73	11.80* ±0.40	178.76* ±7.70	14.76* ±0.38	5.40* ±0.28
30 %	6.68* ±0.32	7.47 ±0.26	49.05* ±0.50	12.20* ±0.40	182.85* ±6.07	15.72* ±0.02	6.57* ±0.25

All values are expressed as mean ±SD, n = 5, * indicates a statistically significant difference ($p < 0.05$).

WF – wheat flour, MTSF – milk thistle seed flour fic volume, and weight loss) of the prepared biscuits.

A significant difference ($p < 0.05$) between each sample in terms of thickness, weight, volume, specific volume, weight loss, and spread ratio was observed. Average thickness of the reference sample was 7.62 mm while in biscuits with the addition of MTSF it varied from 8.10 to 7.47 mm. No significant trend in thickness and width values was found, though Ho and Abdul Latif (2016) found that thickness was positively affected by the increasing level of pitaya peel flour incorporation. According to Chauhan et al. (2016), thickness and width are related to dough viscosity; lower dough viscosity causes cookies spreading at a faster rate. As found, cookies with higher spread ratio are considered to be the most desirable (Chauhan et al., 2016). In this study, the highest spread ratio was observed in biscuits with 20 % of MTSF. The spread ratio of biscuits is also influenced by the water absorption value. Higher water absorption causes less water to be available for sugar dissolution and thus the initial viscosity is higher and the cookies spread less during baking (Ho and Abdul Latif, 2016). In our experiments, water absorption of biscuits increased at 25 and 30 % MTSF supplementation, so the spread ratio decreased compared to a 20 % MTSF addition. It was noticed that specific volume and weight loss increased with the increasing level of MTSF. The specific volume varied from 139.31 $cm^3/100$ g (reference sample) to 182.85 $cm^3/100$ g (30 % of MTSF). According to Kohajdová et al. (2011), specific volume is influenced by the interaction between gluten and dietary fibre. In their research, the addition of apple fibre caused significant decrease of the specific volume of biscuits. Apple fibre contains almost similar level of dietary fibre (46.1 %) as MTSF but mostly from soluble components such as pectins. According to results shown in Table 1 it can be stated that MTSF consists mostly of insoluble fibre and thus the specific volume of biscuits increases. Weight loss increased from 13.27 % (reference sample) to 15.72 % (30 % WF replacement). However, MTSF had lower water holding capacity than WF, thus more water was evaporated during baking.

Mechanical properties of biscuits

Texture results are shown in Figure 1.

Average hardness of the reference sample was 6013 g and it first decreased to 4108 g (20 % MTSF) and then increased to 5583 g (30 % MTSF) with the addition of MTSF. The early decrease in hardness can be attributed to the changes in gluten structure as MTSF considerably affects the formation of gluten matrix. On the other hand, hardness tends to increase with the fibre content. Similar findings have been reported by Singh et al. (2015). In their research, hardness of the high fibre and high protein biscuits varied between 1545.14 and 2298.14 g due to the incorporation of spirulina and sorghum flours. According to Galla et al. (2017), breaking strength of biscuits enriched with higher levels spinach powder was comparable with that of the control, which supports our findings. Hardness is also connected to fracturability, referring to the force with which the material breaks (Singh et al., 2015). Fracturability values differ in all samples but not so significantly than hardness values, 20.43 mm for the reference and 21.31 mm for 30 % WF addition, however, all values were almost similar.

Colour analysis

Colour is one of the main organoleptic parameters influencing the overall acceptability of food products. The effect of MTSF on flour mixtures colour is shown in Table 4.

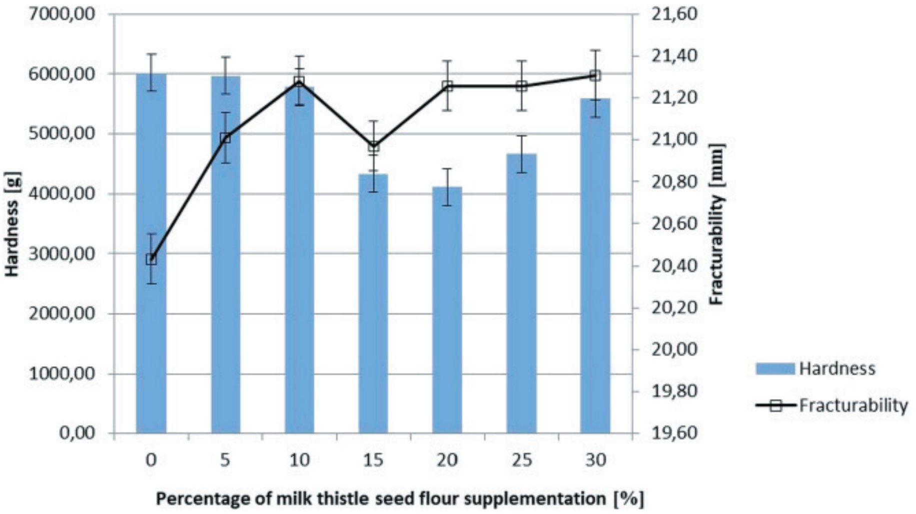

Fig. 1. Texture analysis of biscuits prepared from blends of wheat flour and milk thistle seed flour.

Tab. 4. Colour characteristics of flour mixtures.

Colour parameter	100 WF	95 WF + + 5 MTSF	90 WF + + 10 MTSF	85 WF + + 15 MTSF	80 WF + + 20 MTSF	75 WF + + 25 MTSF	70 WF + + 30 MTSF	100 MTSF
L^*	84.09 ±0.28	84.70* ±0.16	81.35* ±0.73	79.73* ±0.63	77.85* ±0.57	77.46* ±0.66	76.02* ±0.13	58.90* ±0.34
a^*	0.81 ±0.01	0.81 ±0.03	0.93* ±0.05	0.97* ±0.04	1.18* ±0.02	1.26* ±0.02	1.43* ±0.01	2.93* ±0.05
b^*	8.71 ±0.06	8.25* ±0.07	8.17* ±0.05	7.76* ±0.15	8.02* ±0.03	8.32* ±0.07	8.60* ±0.07	9.16* ±0.09
ΔE^*_{ab}	-	0.83 ±0.24	2.79 ±0.72	4.47 ±0.51	6.28 ±0.66	6.65 ±0.86	8.09 ±0.29	25.28 ±0.53

All values are expressed as mean ±SD, n = 5, * indicates a statistically significant differences ($p < 0.05$).
WF – wheat flour, MTSF – milk thistle seed flour, L^* – lightness, a^* – redness, b^* – yellowness, ΔE^*_{ab} – colour differences

From the comparison of wheat flour and MTSF it is evident that MTSF has lower lightness parameter ($L^* = 58.90$) and higher redness parameter ($a^* = 2.93$). Yellowness parameter ($b^* = 9.16$) is not so different from pure WF ($b^* = 8.71$). Therefore, mixtures of wheat flour with MTSF have lower L^* values and higher a^* values. From the analysis of the total colour difference (ΔE^*_{ab}) it results that 5 % and 10 % blends are not so different from pure wheat flour with $\Delta E^*_{ab} = 0.83$ and 2.79, respectively. Other blends showed ΔE^*_{ab} above 3. All values differ significantly ($p < 0.05$). Apostol et al. (2017a) obtained the same results as the highest percentage of added MTSF resulted in higher redness values and lower lightness values. The colour parameters for baked products are listed in Fig. 2.

L^* values in baked biscuits showed the same trend, i.e. the more MTSF was added, the lower lightness was observed. However, redness values were varied significantly. At first, a^* values decreased from 3.64 (reference) to 1.87 (10 % of MTSF), probably due to melanoidin pigments formed during the Maillard reaction. Then, the effect of MTSF redness manifested and the a^* parameter increased up to 5.00 (30 % MTSF). According to Chauhan et al. (2016), protein content is negatively correlated with the lightness of cookies, indicating that the Maillard reaction plays a major role in colour formation. The total colour difference was the lowest in biscuits with 5 % of MTSF ($\Delta E^*_{ab} = 3.76$) at ΔE^*_{ab} of above 4, so the colour changes were easily observed visually. Thus, biscuits enriched with MTSF do not have the same colour parameters as the reference and the replacement above 5 % is not be applicable.

Sensory evaluation

The effects of WF replacement with MTSF on the sensory characteristics of biscuits are shown in Figure 3.

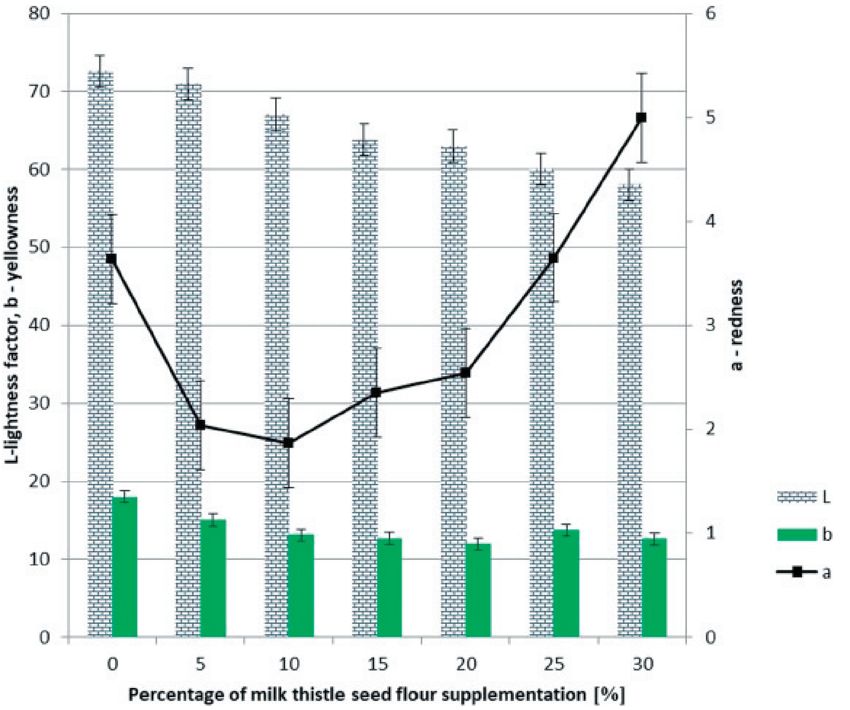

Fig. 2. Colour analysis of biscuits prepared from blends of wheat flour and milk thistle seed flour.

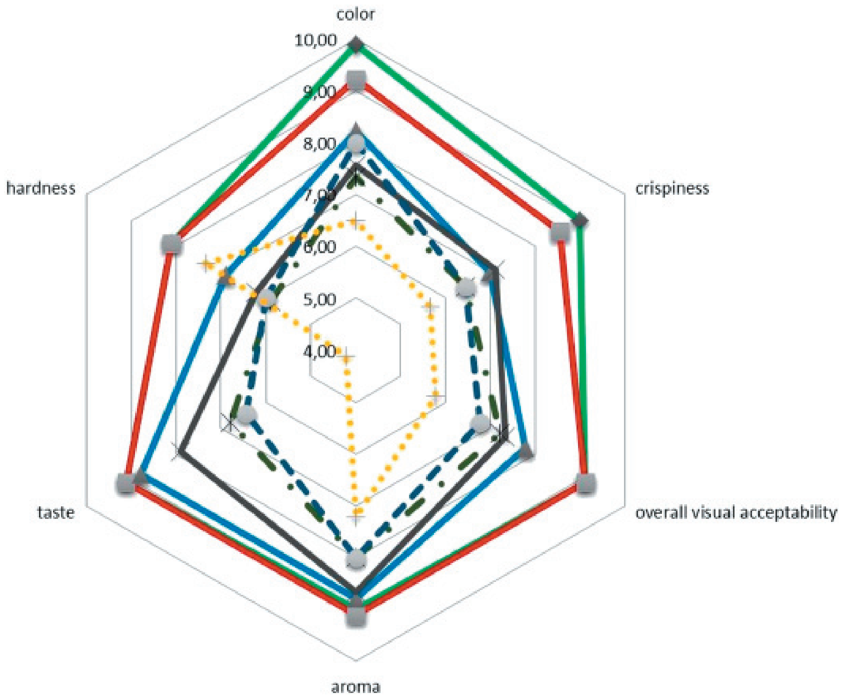

Fig. 3. Sensory evaluation of biscuits prepared from wheat flour and milk thistle seed flour blends.

A significant difference ($p < 0.05$) was observed between each sample in terms of colour, crispiness, overall visual acceptability, taste and hardness while aroma showed statistically lowest difference, so this parameter is not significantly influenced by MTSF addition. All other parameters were slowly decreasing with the increasing MTFS content. According to the panellists, taste was evaluated the worst and the score dropped under 4 in biscuits with 30 % MTSF. They described the products as too bitter with unnatural taste. This corresponds to higher TDF content in biscuits with the increasing MTSF content. According to Shahat Mohamed et al. (2016), changes in taste may be related to the presence of MTS seed coats which contain a high proportion of fibre (lignin). Surprisingly, the drop in colour was not so pronounced even in biscuits with 25 % of MTSF; it is possible that some assessors did not consider darker colour as an issue. The sensory results of hardness corresponded with those found for the mechanical properties; they first gently decreased and then increased again. Almost similar findings were reported by Galla et al. (2017) when biscuits with 5 % of spinach powder content were evaluated similarly as the control samples in all attributes. As it follows from Table 5, biscuits with a 5 % replacement of WF with MTSF were the most acceptable also in these experiments since the obtained data were closest to the reference sample data.

Tab. 5. Overall acceptability of biscuits prepared from WF and WF/MTFS blends.

Level of MTSF addition	Overall acceptability [%]
0 %	92.6 ±9.01
5 %	91.2 ±5.16
10 %	83.3 ±6.24*
15 %	78.3 ±7.45*
20 %	78.9 ±10.09*
25 %	67.2 ±13.14*
30 %	54.4 ±23.00*

All values are expressed as mean ±SD, n = 9, * indicates a statistically significant difference ($p < 0.05$).

WF – wheat flour, MTSF – milk thistle seed flour

These findings have also been confirmed by the Student's test, determining a 5 % replacement as not significant at $p < 0.05$, while a 10 % replacement showed significant difference. Therefore, statistically insignificant replacement in terms of overall acceptability was calculated to be up to the 9.3 % WF replacement.

Correlation analysis

WA of dough was significantly positively correlated with the weight of biscuits (r = 0.98) and negatively with the weight loss (r = –0.93) and specific volume (r = –0.99). DoS was on the other hand positively correlated with weight loss (r = 0.87) and specific volume (r = 0.96). Fracturability of biscuits obtained by texture analysis was negatively correlated with the Mixolab parameters C_2 (r = –0.82), C_3 (r = –0.90), C_4 (r = –0.89),

C_5 (r = –0.79) and DS (r = –0.86); however, positive correlation was found for DDT (r = 0.91). It was found that ΔE^{*}_{ab} values can be directly connected with specific volume (r = 0.96) and weight loss (r = 0.98).

Conclusion

Summarising the results and findings of this study, the following conclusions can be postulated:

4.1. MTSF is a good source of TDF, proteins, mineral compounds and fats and therefore it can be used for human nutrition. Moreover, due to the high content of flavonolignans, summarily called silymarin, and their positive effects on liver, it is also suitable for the production of functional foods.

4.2. Suitability of WF replacement with MTSF in the range of 0–30 % was studied for the preparation of biscuits as healthy bakery products.

4.3. During the experiments, effects of the WF replacement on technological properties of the dough were determined using Mixolab characteristics. Results showed that WA gradually decreased with the increasing amount of TDF. The most influenced parameters were DS and DoS.

4.4. It has been found that WF replacement with 5 % of MTSF is not significant at $p < 0.05$ while 10 % shows a significant difference. Therefore, statistically insignificant replacement of WF with MTSF based on measured parameters was calculated as to be equal to 9.3 %.

4.5. Hence, the production of healthy biscuits on basis of partial WF replacement with MTSF is possible providing a new article in functional bakery products on the market.

Conflict of interest

The authors declare that they do not have any conflict of interest.

Acknowledgements

This research is the result of the project implementation "Building Infrastructure for Modern Research of Civilization's Diseases" (ITMS 26230120009), grant VEGA 1/0487/16, STU Grant scheme for Support of Young Researchers 1610 and APVV-18-0061.

References

Aghajanpour M, Nazer MR, Obeidavi Z, Akbari M, Ezati P, Kor NM (2017) American Journal of Cancer Research 7: 740–769.

Albassam AA, Frye RF, Markowitz JS (2017) Chemico-Biological Interactions, 271: 24–29.

Apostol L, Iorga S, Mosoiu C, Racovita RC, Niculae OM (2017a) Journal of International Scientific Publications 5: 74–84.

Apostol L, Iorga CS, Moşoiu C, Mustăţea G, Cucu Ş (2017b) Scientific Bulletin. Series F. Biotechnologies 21: 165–169.

Bray F, Ferlay J, Soerjomataram I, Siegel RL, Torre LA, Jemal A (2018) Cancer Journal for Clinicians 68: 394–424.

Chauhan A, Saxena DC, Singh S (2016) Cogent Food & Agriculture, 2: 1–8.

El-haak MA, Atta BM, Abd Rabo FF (2015) The Egyptian Society of Experimental Biology 11: 141–146.

Freitas CJ, Valente DR, Cruz SP (2014) Food, Nutrition & Health, 9: 1003–1018.

Galla NR, Pamidighantam PR, Karakala B, Gurusiddaiah MR, Akula S (2017) International Journal of Gastronomy and Food Science 7: 20–26.

Hadnađev TD, Dokić L, Pojić M, Hadnađev M, Torbica A, Rakita S (2014) Hemijska Industrija 68: 99–106.

Ho LH, Abdul Latif NW (2016) Cogent Food & Agriculture 2: 1–10.

Pereira, D, Correia PMR, Raquel PF, Guiné RPF (2013) Acta Chimica Slovaca 6: 269–280.

Karkanis A, Bilalis D, Efthimiadou A (2011) Industrial Crops and Products 34: 825–830.

Kaur A, Shevkani K, Katyal M, Singh N, Ahlawat AK, Singh, AM (2016) Journal of Food Science and Technology 53: 2127–2138.

Kennedy JF, Stevenson DL, White CA (1989) Starch/Stärke 41: 215–221.

Kohajdová Z, Karovičová J, Jurasová M, Kukurová K (2011) Acta Chimica Slovaca 4: 88–97.

Marrubini G, Papetti A, Genorini E, Ulrici A (2017) Food Analytical Methods, 10, 1556–1567.

Mohammadian M, Mahdavifar N, Mohammadian-Hafshejani A, Salehiniya H (2018) World Cancer Research Journal 5: 1–7.

Okuda R, Tabara A, Okusu H, Masaharu S (2016) Food Science and Technology Research 22: 841–846.

Oladunmoye OO, Aworh OC, Maziya-Dixon B, Erukainure OL, Elemo GN (2014) Food Science & Nutrition 2: 132–138.

Pagès J, Bertrand C, Ali R, Husson F, Lè S (2007) Journal of Sensory Studies 22: 665–686.

Radjabian T, Rezazadeh SH, Fallah Huseini H (2008) Iranian Journal of Science & Technology 32: 141–146.

Ramasamy K, Agarwal R (2008) Cancer Letters 269: 352–362.

Riley CK, Wheatley AO, Asemota HN (2006) African Journal of Biotechnology 5: 1528–1536.

Shahat Mohamed S, Hussein Ahmed S, Hady Essam A (2016) Middle East Journal of Applied Sciences, 6: 531–540.

Sindhuja A, Sudha ML, Rahim A (2005) European Food Research Technology 221: 597–601.

Singh P, Singh R, Jha A, Rasane P, Gautam AK (2015) Journal of Food Science and Technology 52: 1394–1403.

Sun-Waterhouse D, Teoh A, Massarotto C, Wibisono R, Wadhwa S (2010) Food Chemistry 119, 1369–1379.

Švec I, Hrušková M (2015) LWT-Food Science and Technology 60: 623–629.

Tabari SA, Carpi S, Polini B, Nieri P, Esfahani ML, Moghadamnia AA, Ghorbani H, Ranaei M, Kazemi S (2019) South African Journal of Botany 124: 494–498.

sciendo

Selected *in vitro* methods to determine antioxidant activity of hydrophilic/lipophilic substances

Aneta Ácsová, Silvia Martiniaková, Jarmila Hojerová

Slovak University of Technology in Bratislava, Faculty of Chemical and Food Technology,
Institute of Food Science and Nutrition, Department of Food Technology,
Radlinského 9, 812 37 Bratislava, Slovakia
aneta.acsova@stuba.sk

Abstract: The topic of free radicals and related antioxidants is greatly discussed nowadays. Antioxidants help to neutralize free radicals before damaging cells. In the absence of antioxidants, a phenomenon called oxidative stress occurs. Oxidative stress can cause many diseases e.g. Alzheimer's disease and cardiovascular diseases. Therefore, antioxidant activity of various compounds and the mechanism of their action have to be studied. Antioxidant activity and capacity are measured by *in vitro* and *in vivo* methods; *in vitro* methods are divided into two groups according to chemical reactions between free radicals and antioxidants. The first group is based on the transfer of hydrogen atoms (HAT), the second one on the transfer of electrons (ET). The most frequently used methods in the field of antioxidant power measurement are discussed in this work in terms of their principle, mechanism, methodology, the way of results evaluation and possible pitfalls.

Keywords: ET methods; HAT methods; *in vitro*; oxidative stress; total antioxidant activity

Introduction

Oxidation process is an important part of the metabolic processes in the human body that produce energy to maintain some essential functions. However, it also has side effects as excessive production of free radicals leads to oxidative changes in the body (Nijhawan and Arora, 2019). Natural defense mechanisms of the human body can eliminate/terminate free radicals. When the production of free radicals prevails over their elimination, they can interact with biological macromolecules (proteins, lipids, carbohydrates) and DNA. The formation of free radicals is initiated by different types of radiation, unbalanced diet, stress, smoking, unhealthy lifestyle, etc. (Klaunig and Wang, 2018). Increased concentration of free radicals in the body can cause skin aging but it can also lead to more serious diseases such as cardiovascular diseases, progressive neurological diseases like Alzheimer's disease, Parkinson's disease, ulcerative colitis and atherosclerosis (Kimáková and Baranovičová, 2015; Yan et al., 2002; Li et al., 2012; Chiavaroli et al., 2011). An antioxidant is generally defined as any substance in low concentration that inhibits or stops the proceeding oxidative damage to important molecules (Yadav et al., 2016). Enzymatic and non-enzymatic antioxidants naturally occur in the human body and counteract the harmful impacts of free radicals (Lobo et al., 2010). An organism can obtain antioxidants from external sources, either in natural form such as from fruits or vegetables, or in synthetic form, for example from nutritional supplements and cosmetics. Vitamin C, coenzyme Q10, beta-carotene, lycopene, uric acid, α-tocopherol, selenium, flavonoids and polyphenols are the best-known natural antioxidants (Farajzadeh, 2016).

In order to compare the effects of individual antioxidants to use them more appropriately, it is necessary to know their antioxidant capacity. Antioxidant capacity of substances is determined by *in vivo* or *in vitro* methods (Joseph et al., 2018). The present work is focused on the methods of *in vitro* determination of antioxidant activity of both hydrophilic and lipophilic samples. *In vitro* methods can be categorized according to a few criteria depending on the kind of radical (peroxyl radicals, hydroxyl, alkoxy and other) they act, according to the chemical reaction or physical and chemical property of the analyzed substance, etc. (Moukette et al., 2015).

Hydrogen Atom Transfer (HAT) methods

DPPH (1,1-Diphenyl-2-picrylhydrazyl) assay

DPPH assay is one of the easiest and most frequently used methods. It has been developed to measure the antioxidant capacity mainly in plants and food extracts (Alshaal et al., 2019). This method uses a commercially available organic compound – 2,2-diphenyl-1-picrylhydrazyl, with the acronym DPPH, generated just before applying the test to a sample. DPPH is a stable chromogen radical caused by electron delocalization in all molecules. This electron delocalization manifests itself in vio-

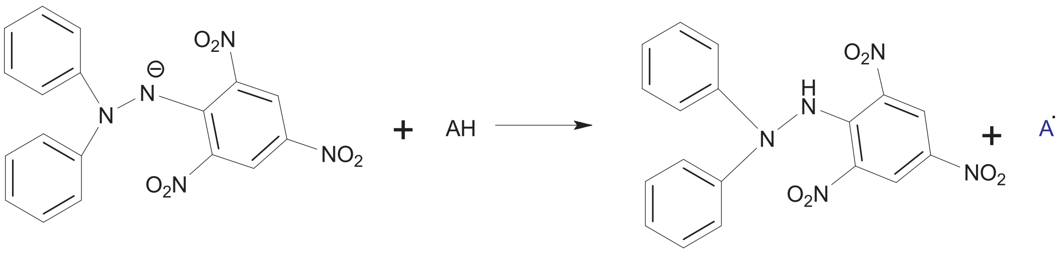

Fig. 1. Reaction of DPPH radical with hydrogen atom donors (Alam et al. 2013).

let in ethanolic/methanolic solution which absorbs radiation with the same wavelength as DPPH radical emits (517 nm) (Pisochi and Negulescu, 2011; Shekhar and Anju, 2014). The DPPH scavenging assay is based on donating a hydrogen atom of antioxidants to 2,2-diphenyl-1-picrylhydrazyl radical to transform it into non-radical form (Fig. 1). The reaction is associated with discoloration of a blue-colored solution to pale yellow as a sign of the potential antioxidant activity of the sample (Alam et al., 2013).

According to Alam et al., 2013, the sample is diluted with a solvent depending on the character of the sample and then mixed with the DPPH solution. Such prepared mixture is first incubated for 30 min at 25 °C and after an aliquot of the incubated solution is added to the spectrophotometer, the absorbance at 517 nm is measured (Moran-Palacio et al., 2014). The percentage of DPPH radical scavenging (ESC = experimental scavenging capacity) is calculated using Eq. 1:

$$ESC = \frac{A_{br} - A_{ar}}{A_{br}} \times 100\ \% \qquad (1)$$

where A_{br} is the absorbance measured before the reaction and A_{ar} after the reaction. The antioxidant activity is then expressed as the amount of antioxidant sample needed to decrease the synthetic DPPH radical's concentration to 50 % (also known as EC_{50}) (Pisochi and Negulescu, 2011). In addition, the power of the antiradical potential can also be characterized by the µM Trolox equivalent for the initial amount of fresh mass (µM/g FM).

Although the DPPH method is simple, it is very sensitive and easily influenced by various factors such as the presence and concentration of hydrogen atom, amount of used solvent, presence of catalytically acting metal ions and freshness of the DPPH solvent (Zhong and Shahidi, 2015). What makes the DPPH radical reactive is the presence of nitrogen atom with an unpaired electron in the center of the DPPH molecule (Yeo and Shahidi, 2019). However, this presents a steric limitation for large molecules as they cannot inhibit the radical portion of the DPPH radical located in the center (Holtz, 2009). Smaller molecules able to effectively overrun the steric barrier in the DPPH molecule include ascorbic acid and simple phenols. The reaction between phenol and the radical can be slowed down if side chains or acid groups are connected on the aromatic rings of phenols (Schaich et al., 1985). Yeo et al. (2019) studied limitations of the DPPH scavenging ability of pigments and dyes from plant extracts. The limiting factor was that dyes and pigments reached their absorption maximum at the same wavelength as DPPH radicals. To overcome this limitation, different equipment and a different antioxidant activity of dyes determination method, such as electron paramagnetic resonance (EPR) spectroscopy, was used. Values obtained by the EPR spectroscopy differ by more than 16 % from those obtained by the standard spectrophotometric DPPH method.

TRAP (Total peroxyl radical-TRapping Antioxidant Potential) assay

TRAP method proposed by Wayner et al. in 1985 was used to quantify the antioxidant capacity in human blood plasma. Since then it has undergone some modifications but its principles have been preserved. The effect of either free radicals or the presence of antioxidants on the fluorescence generated by the fluorescent molecule is monitored. This method monitors the amount of consumed oxygen during lipid peroxidation caused by the thermal brake down of substances such as ABAP (2,2´-Azobis(2-amidinopropane) (Figure 2) or AAPH (2,2´-azobis(2-methylpropionamidine) dihydrochloride) into simpler matters (Martín et al., 2017).

The TRAP test is often applicable in the determination of the antioxidant activity of biological samples as human plasma or natural samples as plant extracts (Denardin et al., 2015). The TRAP method is sensitive to temperature and pH changes (Martín et al., 2017). Denardin et al. (2015) studied fruit extracts for their non-enzymatic antioxidant capacity using this antioxidant method. The peroxy radical was generated by mixing a solution of AAPH with Luminol to enhance chemiluminescence. A sample was added to the peroxy radical and the absorbance after 30 minutes of incubation was measured.

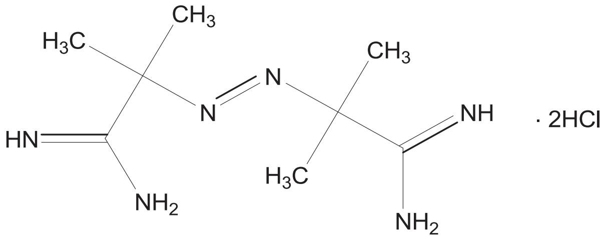

Fig. 2. Chemical structure of ABAP.

They concluded that fruits with higher content of phenols also have higher antioxidant activity. Moreover, although Brazilian plant called *Butía* had high content of the well-known antioxidant – ascorbic acid, its power to fluorescence quenching was lower than in other plants. This assay is very suitable for biological samples such as plasma, urine and others because they are able to perfectly react and combine with peroxy radicals (Munialo et al., 2019).

ORAC (Oxygen Radical Absorbance Capacity) assay

Advantages of the ORAC test include high adaptability to antioxidants, biological samples and foods and the capability of assaying antioxidant potential of non-protein samples using a wide range of extraction agents (Prior, 2015). The reaction is conceptually simple but difficult in practice. The reactions start with heating of azide compounds to release nitrogen gas and generate two radicals ($R^\bullet$) (equation 2). During the radical generation, it is very important to keep the optimal heating temperature to ensure total azide decomposition. If the required temperature is not maintained, unclear and incomparable results are obtained (Mellado-Ortega et al., 2017).

The interaction between $R^\bullet$ and sufficient oxygen leads to the formation of peroxy radicals, $ROO^\bullet$ (equation 3) which can either attack near colored or fluorescent molecules (equation 4) or react with antioxidants (equations 5, 6). Fluorescence is lost when a fluorescent molecule is attacked by peroxyl radicals. The less antioxidant participates in the reaction, the higher the decomposition of the fluorescent molecule and the higher the fluorescence signal loss (Schaich et al., 2015).

$$R{-}N{=}N{-}R \overset{\Delta t}{\rightarrow} N_2 + 2R^\bullet \tag{2}$$

$$O_2 + 2R^\bullet \rightarrow ROO^\bullet \tag{3}$$

$$ROO^\bullet + \text{target molecule} \rightarrow \\ \rightarrow ROOH + \text{oxidized molecule} \tag{4}$$

$$ROO^\bullet + AH \rightarrow ROOH + A^\bullet \tag{5}$$

$$ROO^\bullet + A^\bullet \rightarrow ROO{-}A \tag{6}$$

Fluorescence intensity over time is monitored via the antioxidant activity evaluation. Trolox is used as a standard for evaluation where its different concentrations are used to obtain a fluorescence intensity time-curve and compared with the test samples. Thus, quantification of the ORAC test is based on the evaluation of the area under the time-curve (AUC) (Schaich et al., 2015).

CB (Crocin Bleaching) assay

Crocin bleaching assay is suitable for the antioxidant potential determination of both lipophilic and hydrophilic samples (Yeum et al., 2004). This method uses crocin (Figure 3) as a substance competing with the added antioxidant and AMVN (2,2´-azobis-2,4-dimethylvaleronitrile) or AAPH (2.2´-azobis-2-amidinopropane: R–N=N–R) as the source of free radicals. AAPH is generally used for cuvette spectrophotometer, while AMVN is more frequently used for a microplate spectrophotometer. The degree of crocin whitening by a potential antioxidant is measured at 450 nm (Prieto et al., 2015; Sotto et al., 2018).

Interaction between free radicals and crocin polyene structure results in disruption of the conjugated system, which corresponds to crocin bleaching. The disruption of the crocin polyene structure depends on the form of the radical with which it reacts. Conversely, hydroxyl type of radicals cannot be used here due to their high reactivity with other organic substances (Ordoudi and Tsimidou, 2006).

Peroxyl radicals are formed in two steps; the first one is thermal degradation of the initiator (equation 7) and the second one is the reaction with oxygen to generate peroxyl radicals (equation 8).

$$NR{=}NR \overset{\Delta t}{\rightarrow} 2R^\bullet + N_2 \tag{7}$$

$$R^\bullet + O_2 \leftrightarrow ROO^\bullet \tag{8}$$

$$ROO^\bullet + \text{crocin} \rightarrow ROOH + \text{crocin}^\bullet \tag{9}$$

$$ROO^\bullet + AH \rightarrow ROOH + A^\bullet \tag{10}$$

$$A^\bullet + \text{crocin} \rightarrow AH + \text{crocin}^\bullet \tag{11}$$

Subsequently, radicals cause crocin bleaching (equation 9) leading to the solution color loss. More mechanisms of reaction of the resulting radical with an antioxidant can be considered depending on the type of antioxidant. In case of β-carotene or other carotenoid antioxidants, very common mechanism is hydrogen atom abstraction (equation 10). Other radicals are also formed as intermediates which are further bound to the crocin structure and the bleaching process begins to cycle (Ordoudi

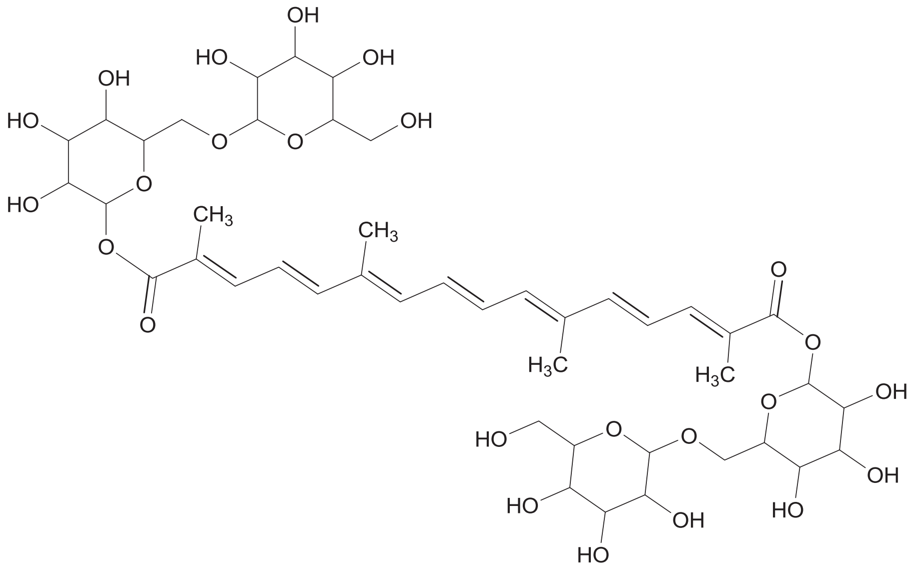

Fig. 3. Chemical structure of crocin.

and Tsimidou, 2006). Bleaching reaction rates of antioxidant and sample without antioxidant were calculated simultaneously by monitoring the decrease in absorbance at 450 nm and a suitable temperature. Trolox, synthetic analogue of vitamin E, can be used as a reference at the same conditions as the analyzed samples. Then, the overall concentration ratio (result) of crocin bleaching calculated as crocin inhibition in percentage or as relative constant of bleaching process rate (Bortolomeazzi et al., 2007).

Disadvantages of this method include the low reproducibility, sample preparation by pre-heating and strict compliance of working temperature and pH, differences in reagent preparation and problematic quantification of results (Prior, 2015).

TOSC (Total Oxyradical Acavenging Capacity) assay

The research groups of Regoli and Winston (1998) were the first ones interested in quantification of total oxyradical scavenging capacity by antioxidants (Franzoni et al., 2017). The TOSC method has a wide application as it can be used for one-component antioxidants but also in complexes such as tissues or biological fluids in the body. Moreover, large deviations of both hydrophilic and lipophilic substances cannot be observed despite their sometimes lower concentration range (Lichtenthäler et al., 2003). The TOSC test is based on the reaction between free radicals, especially oxyradicals (peroxyl, hydroxyl, and peroxynitrite radicals) (Ojha et al., 2018), and α-keto-γ-methiolbutyric acid (KMBA) to form the simplest organic compound known as ethene (equation 12). Each radical is obtained in a different way. While generation of peroxyl radicals and peroxynitrite requires heat processing of 2,2´-azobis(2-methylpropionamidine) dichloride (ABAP) and 3-morpholinosydnonimine N-ethylcarbamide, respectively, the formation of hydroxyl radicals runs through the Fenton reaction (Garrett et al., 2010).

$$CH_3S—CH_2—CH_2—CO—COOH + O^{\bullet}OH(R) \rightarrow$$
$$\rightarrow \tfrac{1}{2}(CH_3S)_2 + RHOO^- + CO_2 + CH_2{=}CH_2 \qquad (12)$$

As mentioned above, when radicals interact with KMBA, ethene in gaseous state is formed and its formation can be monitored by gas chromatography. The potential antioxidant is as strong as it can prevent oxidative decomposition of the acid in the presence of oxyradicals (Regoli, 2000).

DMPD (N1,N1-DiMethyl-1,4-PhenyleneDiamine) assay

Also in case of DMPD assay, oxidants in the samples are reduced and the color change is evaluated spectrophotometrically (equation 14). First, the $DMPD^{\bullet+}$ radical is formed by mixing a solution of DMPD (Figure 4) in acetate buffer and ferric chloride $FeCl_3$ (equation 13) (Jiang et al., 2019). The prepared red colored solution of the DMPD cation is allowed to stand at laboratory temperature for 12 hours before being used to assess antioxidant activity of the sample (Askin, 2018). Oxidative status of the substance with $DMPD^{\bullet+}$ is readable at 515 nm (Kamer et al., 2019; Goosen, 2018).

$$DMPD_{(colorless)} + oxidant(Fe^{3+}) + H^+ \rightarrow$$
$$\rightarrow DMPD^{\bullet+}_{(purple)} \qquad (13)$$

$$DMPD^{\bullet+}_{(purple)} + AOH \rightarrow DMPD^{+}_{(colorless)} + AO \qquad (14)$$

Advantages of this method include short reaction time, long life time of the chemical reaction and low financial costs. These advantages are the most important criteria for compatible global assays (Rodriguez-Nogales et al., 2011). Each method has its advantages and disadvantages; for example, lower applicability for hydrophobic substances as the reproducibility of the method decreases with the increasing hydrophobicity. Another serious disadvantage is in the compatibility of several solvents. The choice of methanol as a solvent for DMPD is not very suitable (Singh and Singh, 2008).

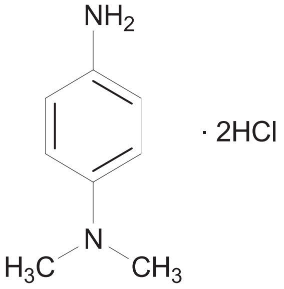

Fig. 4. Chemical structure of DMPD.

Single Electron Transfer (SET) methods

ABTS (2,2´-azinobis(3-ethylbenzothiazol-6-sulphonate)) assay

The first method based on single electron transfer described in this work is an ABTS decolorization test. The application of this method is wide due to its numerous modifications and it can be applied in antioxidant activity determination in both pure lipophilic and hydrophilic antioxidants, including carotenoids, flavonoids (Granato et al., 2018) and food samples, beverages and plasma antioxidants (Ferrante et al., 2019), because this radical is soluble in water but also in several organic solvents (Re et al., 1999).

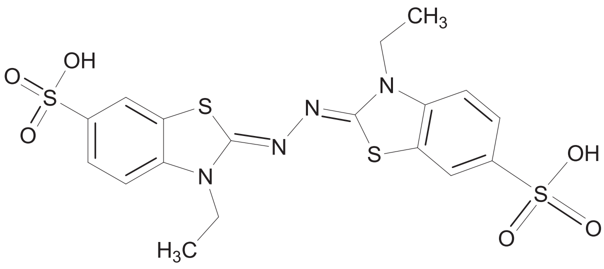

Fig. 5. Chemical structure of ABTS.

The $ABTS^{•+}$ (2,2´-azinobis-(3-ethylbenzothiazoline-6-sulfonic acid)) radical can be generated in several different ways: less often electrochemically, enzymatically in case of biologic samples and chemically used potassium persulfate (Figure 6) or peroxide radicals. The original blue-green solution is decolorized while the decolorization is adequate to the power of the substance antioxidant activity (Floegel et al., 2011). An advantage of this method is that it has a short analysis time and synthetic $ABTS^{•+}$ radical has a characteristic absorption spectrum with maximum peaks in the range of 414 to 815 nm, which is an advantage in case of colored compounds (Lim et al., 2019; Wan et al., 2018).

Mixture of potassium persulfate with ABTS substance in the ratio 0.5:1 has to be maintained for at least 6 hours. A shorter interaction may result in partial oxidation, leading to unstable $ABTS^{•+}$. The radical is stable for up to two days when stored in a container without light and oxygen at room temperature. As with previous methods, it is impor-

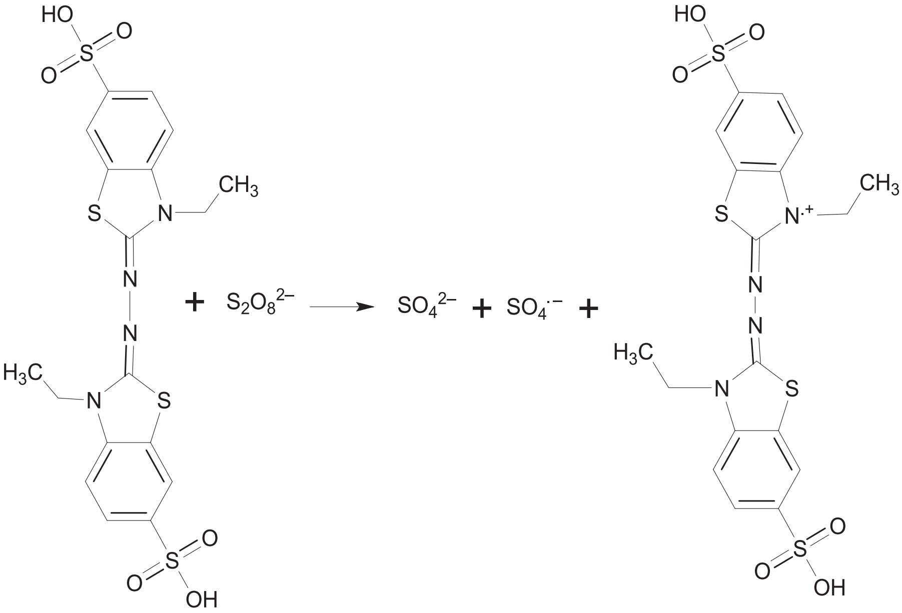

Fig. 6. Generation of ABTS cation radical (Zou et al. 2019; custom modification).

tant to differentiate the reaction time intervals at which ABTS$^{•+}$ and the analyzed sample react (Re et al., 1999); which is 6 minutes according to Re et al. (1999), Pérez-Jiménez et al. (2008) and Van den Berg et al. (1999) while Alam et al. (2013) considered only a 5 min interval when determining the antioxidant activity of plant extracts. Pérez-Jiménez et al. (2008) determined polyphenols (Coffee acid, Ferulic acid, Gallic acid, Quercetin and Rutin) in extracts of white and red grape, which represents an excellent source of antioxidants. Re et al. (1999) investigated anthocyanins and flavonoids. Van den Berg et al. (1999) investigated α-tocopherol, β-carotene and Vitamin C and their combinations.

Determination of antioxidant activity such as DPPH but also ABTS methods are usually performed using a spectrophotometer. A disadvantage is that it is not possible to separate the antioxidants present in the samples as complex matrices (Alam et al., 2013). Ma et al. (2019) proposed using liquid chromatography or capillary electrophoresis as a complementary method for online DPPH or ABTS assays to make these spectrophotometric methods full-fledged and more informative (Koleva et al., 2000; Murauer et al., 2017).

TEAC (Trolox Equivalent Antioxidant Capacity) assay

TEAC is a commonly used assay to assess the amount of radicals that can be scavenged by antioxidants able to offer their electrons. The TEAC method is very closely related to the ABTS method (Zablocka et al., 2019). The name of the method indicates that the main component is Trolox with a chemical identifier as 6-hydroxy-2,5,7,8-tetramethylchroman-2-carboxylic acid (Figure 7). It is easy to convert absorbances obtained from a spectrophotometer into the antioxidant activity of Trolox and thus it is used as the comparing standard substance for measurements. Trolox is a chromanol, which means that it is a member of the phenols group and a monocarboxylic acid. For pure substances, TEAC is defined as the millimolar concentration of Trolox corresponding to the antioxidant activity of the test sample at the concentration of 1 mmol/L. In case of mixtures and complex samples, the Trolox substance amount corresponds to antioxidant activity of 1 g or 1 mL of the sample (Obón et al., 2005).

This method was developed by Miller et al. (1993) and it can be used spectrophotometrically with both synthetic radicals of DPPH and ABTS. The colored complex of radicals in the presence of a sample containing substances with a potential antioxidant, is discolored. Depending on the rate of solution discoloration, it is possible to determine the sample activity at a suitable wavelength. TEAC assay can also be adapted and automated to flow injection and microplates techniques (Zhong and Shahidi, 2015).

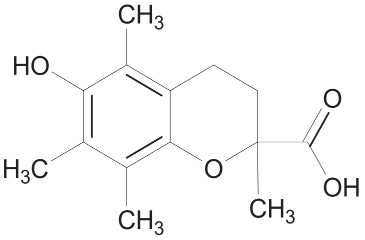

Fig. 7 Chemical structure of Trolox.

This method has many modifications. For example, Pérez-Burillo et al. (2018) introduced two types of the TEAC method – TEACOH, and TEACAAPH. TEACOH determines the quenching effect of hydroxyl radicals (OH$^•$) with foodstuffs, while TEACAAPH analyzes the quenching effect of AAPH$^•$ radicals with beverages and different foods (Obón et al., 2005).

FRAP (Ferric Reducing Ability of Plasma) assay

Ferric reducing/antioxidant activity is a primary method for assessing the total antioxidant capacity. The FRAP method is sensitive, cheap and fast (Choy et al., 2000). Ferric ion of TPTZ (2,4,6-Tri(2-pyridyl)-1,3,5-triazine) reduction by an antioxidant (Figure 8) in the presence of acetate buffer causes the formation of a blue colored ferrous-tripyridyltriazine com-

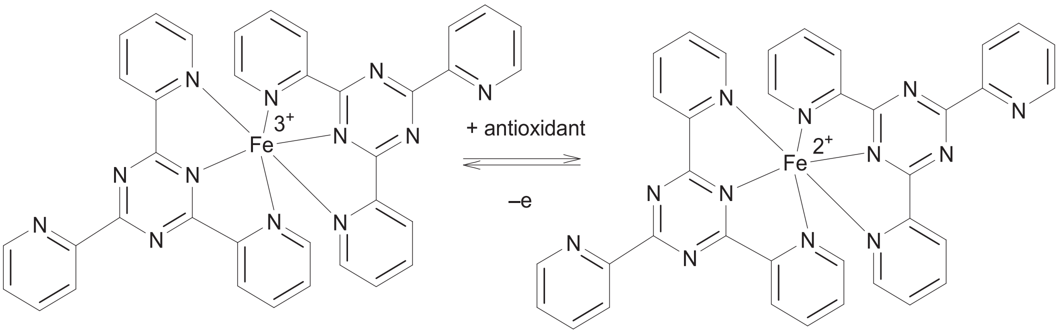

Fig. 8. Chemical reaction of TPTZ and antioxidant (Shalaby, 2013).

plex. The reduction is indicated by the formation of intense blue color with an absorption maximum at 593 nm (Benzie and Strain, 1999; Seesom et al., 2018). Basically, the FRAP value is evaluated as the reduction power of Fe(III) to Fe(II) (Haida and Hakiman, 2019; Ononamadu et al., 2019). Another evaluation method employs equivalent concentration of Trolox to the initial sample amount (Lachowicz et al., 2018). The FRAP working solution is made under heating (37 °C) when acetate buffer, TPTZ and $FeCl_3 \cdot 6H_2O$ are mixed together in the ratio of 10:1:1 (Benzie and Strain, 1999). Ideally, the solution is yellow if there is no reduction of ferric ions. Fresh frap working solution should be used in each experiment. Subsequently, optimal amount of the working solution is mixed with an aliquot and the change in absorbance can be seen at 593 nm after a 30 minutes interaction of the FRAP reagent with the sample (Oribayo et al., 2018).

Torre et al. (2015) introduced a modified microplate-based FRAP method (mFRAP) which leads to improved sample throughput compared to the manual FRAP assay. The main difference is that microplates are used instead of glass cuvettes and smaller volumes of samples are needed to determine the antioxidant activity. Burnaz and coworkers found that online or offline association of FRAP antioxidant evaluation with chromatographic separation methods represents a significant improvement in the awareness of antioxidant contributions of individual compounds of the complex samples. The HPLC method is one of the most used pre-treatment methods for the samples further determined by the FRAP method. The lengthy pre-treatment processes sometimes last for days, which is a big disadvantage. Shi et al. (2019) eliminated the pre-treatment by introducing of a microcolumn packed with a very small amount of solid sample, also the system of antioxidant evaluation is faster.

CUPRAC (CUPRic Antioxidant Capacity) assay

Another method for antioxidant capacity *in vitro* determination is the CUPRAC method, where the redox properties of copper are the guiding principle. It is used to determine both water- and oil-soluble substances in the physiological pH range (Sundararajan and Ilengesan, 2018; Drouet et al., 2018), providing a great advantage over FRAP, where acetate buffer is used to prepare the chemical reagent causing an acidic environment (Gupta, 2015).

In this method, neocuproine is used as the chelating agent which, when reacted with an antioxidant, yields a CUPRAC chromophore. CUPRAC chromophore is maximally detectable at 490 nm. The chelating agent has to be prepared in the correct ratio of neocuproine:copper(II)chloride:ammonium acetate and protected from unacceptable environmental factors as air and daylight (Celik, 2019).

The reaction most often proceeds at pH 7 for 30 minutes. In case of antioxidants which react slower and harder, these need to be heated at the temperature of ~50 °C for 20 min to improve their color visualization (Apak et al., 2008). The resulting color is orange-yellow. The antioxidant capacity of compounds is most often expressed as Trolox equivalents (TEAC values) (Alam et al., 2013).

The CUPRAC method is used to measure the antioxidant level of total phenolics, separately flavonoids, vitamins, but also synthetic antioxidants to compare them (Gupta, 2015). As in many other methods, a spectrophotometer is required for the measurement, which is one of the disadvantages. Results obtained by combination of CUPRAC and TEAC assay modified by Akar et al. (2019) were differentiated with the original spectrophotometrically obtained TEAC values. Another modification may be the use of a drip of the reaction sample for TLC chromatography in combination with CUPRAC and subsequent subtraction of probes in the image program.

FC (Folin-Ciocaltueau) assay

The Folin-Ciocalteu method was originally developed for the determination of protein complexes, specifically for tyrosine which contains a phenolic group in the FC reagent molecule.

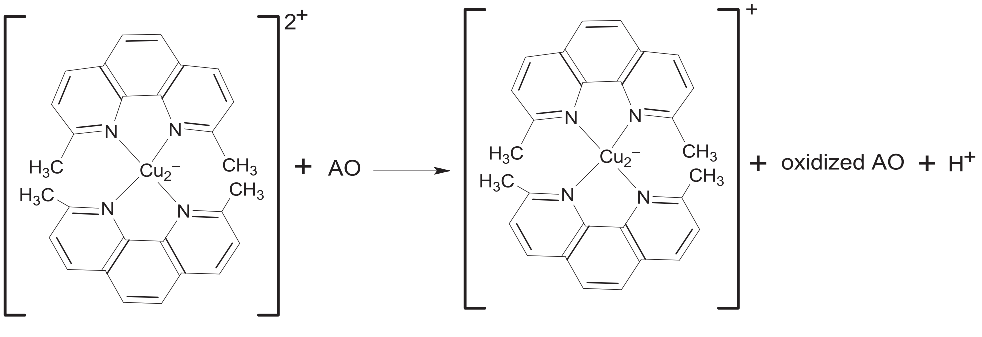

Fig. 9. Reaction scheme for the CUPRAC assay.

Thanks to Singleton et al. (1999), the FC method has evolved to determine total phenols in other sample matrices, especially in wine (Everette et al., 2010). However, it has been shown that the reaction of an antioxidant with the FC reagent results in an increased electron transfer from the antioxidant compared to the hydrogen atoms, contributing to the degree of antioxidant activity evaluation of potential antioxidants (Abramovič et al., 2018). The principle of this method is reducing the FC reagent composed of a mixture of phosphotungstic acid and phosphomolybdenic acid to a mixture of blue tungsten oxides and molybdenum oxides by oxidizing phenols present in the sample. The blue color is a result of Mo(VI) reduction to Mo(V) and it shows maximum light absorption in the wavelength range of 750–760 nm (Figure 10) (Ainsworth and Gillespie, 2007). The FC chromophore, namely molybdo-tungsto-phosphate polyanion ($PMoW_{11}O_40_4^-$), shows affinity for hydrophilic greater extent as its negative charges are able to interact with molecules of water in a much more than with organic solvents. That is why the conventional FC test is mainly used in hydrophilic phases and it is not suitable for lipophilic substances determination in a modified form. Determination of lipophilic substances can be adapted by a modification of the original FC method – in isobutylalcohol (Berker et al., 2013). The difference between a conventional FC test and this modified one is that the FC reagent is prepared in isobutanol (Minussi et al., 2003) and the test is realized in the presence of NaOH, thereby inducing suitable conditions for both types of substances (Wong et al., 2006).

The FC reagent is prepared by dissolving sodium molybdate ($Na_2MoO_4 \cdot 2H_2O$) and sodium tungstate ($Na_2WO_4 \cdot 2H_2O$) in deionized water. The mixture is then acidified with concentrated HCl and 85 % phosphoric acid. Such prepared acidified solution is boiled for 10 hours and $Li_2SO_4 \cdot 4H_2O$ is then added at room temperature. The resulting solution can be yellow (Huang et al., 2005). In this case, the reducing agent is molybdate which should have stronger redox properties than tungsten (equation 15). In the reaction with an antioxidant, blue color exhibits maximum light absorption in the wavelength range of 750–760 nm and its intensity is directly proportional to the total amount of phenols initially present in the sample (Sánchez-Rangel et al., 2013).

$$\begin{gathered}\mathrm{Mo}^{\mathrm{VI}} + \mathrm{e}^- \text{ (from phenolic} \\ \text{or another reduced substance)} \rightarrow \mathrm{Mo}^{\mathrm{V}} \end{gathered} \tag{15}$$

The Folin-Ciocalteu assay has been widely used to determine the absolute phenolic content and antioxidant potential of plant-derived food and biological samples (Huda-Faujan et al., 2009; Al-Farsi et al., 2018; Shalaby, 2013). The *in vivo* results showed a strong indirect correlation between the phenol content and the prevention of serious diseases such as neurological or cardiovascular disease and DNA damage (Lamuela-Raventós, 2018).

ESR (Electron Spin Resonance)

Nowadays, methods allowing immediate monitoring of free radicals alone and in reaction with a complex system (for example cells and tissues) are very important and widely used (Burlaka et al., 2018; Bukhari et al., 2018; Borbat et al., 2001). These methods mainly include ESR and electromagnetic spin resonance, also called electron paramagnetic resonance spectroscopy, EPR. Not only most complex food samples (Gardner et al., 1999) but also cosmetics or biological pharmaceutical samples are analyzed by ESR (Yamaguchi et al., 1999; Zang et al., 2017). This method is specific to the detection of unpaired electron species and it has an incomparably higher detection sensitivity than the previous spectrophotometric methods (Davies, 2016; Li et al., 2016; Yu and Cheng, 2008).

ESR uses microwave spectroscopy to detect spin state changes in substances containing unpaired electron spins (paramagnetic substrate). Spin state changes can be induced by microwaves with several milliwatts of energy when the substrate is placed in a magnetic field with 3480 gausses at the frequency of 9.5 GHz (Figure 11) (Behzadnezhad et al., 2018). The resonance conditions directly depend on parameters such as the Planck's constant (h), frequency (ν) and the type of magnetic field (H) and on the Bohr magneton (β, equation 16) (Kleschyov et al., 2007).

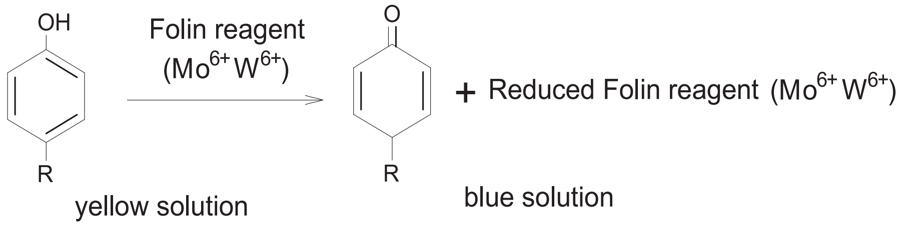

Fig. 10. Reaction of FC reagent with sample containing a hydroxyl group.

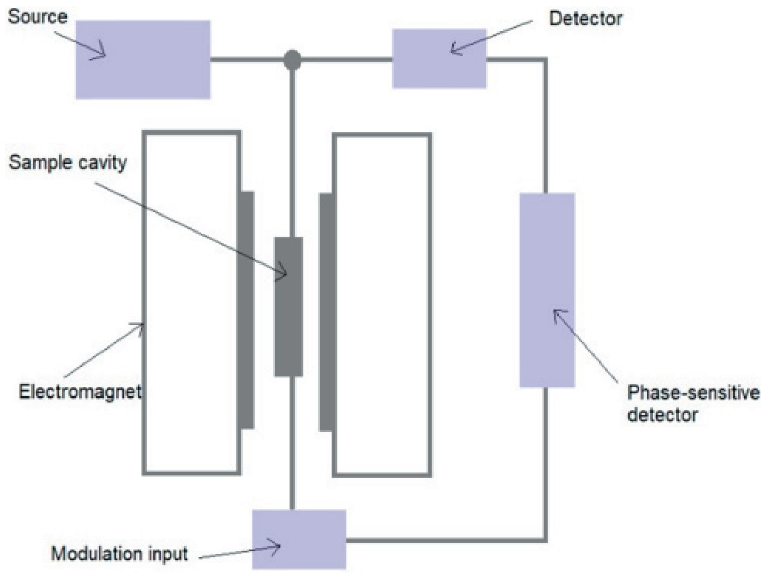

Fig. 11. Electron Spin Resonance apparatus.

$$h\nu = g\beta H \quad (16)$$

Detection runs only with paramagnetic particles. Moreover, the presence of genetically active nuclei can also be observed in the spectrum (Davies, 2016).

At present, EPR spectroscopy has become a trend in antiradical activity determination in organosulfur compounds containing a sulfur-hydrogen bond (Jiang et al., 2018), phenolic compounds (Gardner et al., 1999; Okazaki and Takeshita, 2018), metal ions or tocopherol analogues (Sakurai et al., 2019). In case of thiol-containing compounds, several assays can be used, such as TEAC (more detailed in the text above) or frequent assays for the reduction of Cu^{2+} ions to Cu^{+} by thiol compounds. In case of phenolic compounds, Okazaki et al. (2018) associated ESR with DMPO (5,5-dimethyl-1-pyrroline N-oxide) trapping and degradation by UV radiation while its adducts are quenched with phenols such as catechol, hydroquinone and resorcinol dissolved in a polar solvent (Okazaki and Takeshita, 2018).

Discussion

Antioxidant activity of substances can be studied by electron or hydrogen transfer methods. Determination of antioxidant activity should not be evaluated only by one test only because every method is relatively specific and it characterizes the antioxidant activity of pure substances and mixtures by its own mechanism of action; e.g. by scavenging of synthetic radicals, donation/acceptance of electrons or hydrogen atoms between antioxidants and oxidants or through the redox properties of substances or mixtures that are determined.

In the radical scavenging methods, reaction time of an antioxidant with a radical or with reagent varies considerably in various studies but it is usually in minutes (ABTS – 6 min, DPPH – 30 min, etc.). Reactivity depends on the structure of substrate molecules (inducing effects of substitutes and active groups present, steric hindrances), but also on solvent polarity, applied temperature and pH during the working assay and characteristics of reactive species. The fastest, simplest and cheapest method compared to others is the DPPH method (Alam et al., 2013). It has a widespread application in measuring antioxidant potential of beverages of fruit and vegetable origin, wheat grains, brans, edible vegetable seed oils, ascorbic acid, tocopherol and polyhydroxyaromatic compounds. This method is suitable for the analysis of substances dissolved in polar as well as non-polar solvents since the synthetic radical is dissolved in ethanol or methanol (Kedare and Singh, 2011). Other methods applicable to lipophilic and hydrophilic substances include the CB, TOSC and ABTS methods. The DMPD method is specific for potential lipophilic antioxidants testing and FC method for hydrophilic potential antioxidants (Apak et al., 2018).

Methods mentioned in the previous paragraph (DPPH, CB, ABTS, FC) belong to the spectrophotometric assays because they measure the absorbance of samples. In this work, methods based on the redox properties are also described. First, DMPD assay in which DMPD color is reduced. Second assay is FRAP in which ferric ions are reduced to ferrous ions and CUPRAC method using the reduction of copper from the oxidation number +2 to +1 (Gupta, 2015).

Each method has its advantages and disadvantages and they can be modified for better application;

however, these modifications represent an increase in either operating or equipment costs. Currently preferred methods applicable to hydrophilic and lipophilic antioxidants include DPPH, CB, TOSC and ABTS assay. In 2017, 0.17 % of all manuscripts published in journals (Scimago Journal & Country Rank) contained keywords DPPH, Folin-Ciocalteu assay or ABTS in the abstracts. According to Thaipong et al. (2006), it is very important to pay attention to the time and cost of assay necessary to determine the required parameters. A disadvantage of the ORAC method is its expensive work mechanism, whereas in the FRAP, ABTS and DPPH assays commonly available optical instruments are applied for measuring of light intensity relative to wavelength. Extra advantage of ABTS and FRAP assay is the rapid reaction of reagents with the sample to be analyzed; while the reaction in DPPH and ORAC methods are much slower. The FRAP test is characterized by its high ability to reproduce and repeat. TOSC and ORAC assays can be used for complex biological samples such as fluids and tissues. According to the study of Franzoni et al. (2017), the TOSC method is unique as it enables evaluating antioxidant potential of substances in the range of μM.

Conclusions

The review of relevant assays for antioxidant activity determination in various substances from 1985 to the present is provided. Classification and characteristics of antioxidant assays were included. Each assay has its own mechanism of action such as color change during the reaction (DMPD, CB, ABTS, FC, DPPH, FRAP, CUPRAC), disappearance of luminescence (TRAP, ORAC), formation of ethylene (TOSC) or absorption of electromagnetic radiation (ESR). Then, the advantages and disadvantages of various antioxidant assays were compared by summarizing various characteristics of their application methods.

Reproduction of the results in different laboratories is crucial. It is most preferred to combine several methods for antioxidant activity determination. Thus, the range of methods for analyzing the properties of potential antioxidants can be expanded leading not only to the development of improved methods but also to more successful implementation of different analytical mechanisms in antioxidant substances and mixtures.

Acknowledgements

Support of the National Grant Agency, project No. APVV-16-0088, as well as VEGA 1/0012/19 are greatly acknowledged.

References

Abramovič H, Grobin B, Ulrih NP, Cigić B (2018) Journal of Chemistry 2018: 9 pages.

Ainsworth EA, Gillespie KM (2007) Nature Protocols 2 (4): 875–877.

Akar Z, Burnaz NA (2019) LWT 112: 108212.

Alam MN, Bristi NJ, Rafiquzzaman M (2013) Saudi Pharmaceutical Journal 21 (2): 143–152.

Al-Farsi M, Al-Amri A, Al-Hadhrami A, Al-Belushi S (2018) Heliyon 4 (10): e00874.

Alshaal S, Karabet F, Daghestani M (2019) Analytical and Bioanalytical Chemical Research 6: 97–110.

Apak R, Capanoglu E, Shahidi F (2018) Measurement of Antioxidant Activity and Capacity: Recent Trends and Applications. John Wiley & Sons, USA.

Apak R, Güçlü K, Özyürek M, Celik SE (2008) Microchemica Acta 160 (4): 413–419.

Askin H, Yilmaz B, Gulcin I, Taslimi P, Bulut S, Yildiz M, Kandemir N (2018) Indian Journal of Pharmaceutical Sciences 80 (5): 802–812.

Behzadnezhad B, Behdad N, Mcmillan AB (2017) United States Patent Application Publication 2018/0340999 A1.

Benzie IFF, Strain JJ (1999) Methods in Enzymology 299: 15–27.

Berker KI, Ozdemir Olgun FA, Ozyurt D, Demirata B, Apak R (2013) Journal of Agricultural and Food Chemistry 61 (20): 4783–4791.

Borbat PP, Costa-Filho AJ, Earle KA, Moscicki JK, Freed JH (2001) Science 291: 266–269.

Bortolomeazzi R, Sebastianutto N, Tonioolo R, Pizzariello A (2007) Food Chemistry 100 (4): 1481–1489.

Bukhari MH, Batool S, Raza DY, Bagasra O, Rizvi A, Shah A, Sultan T (2018) Electromagnetic Biology and Medicine 37 (3): 1–6.

Burlaka AP, Vovk AV, Burlaka AA, Gafurov MR, Iskhakova KB, Lukin SN (2018) BioMed Research International: 4848652.

Burnaz NA, Küçük M, Akar Z (2017) Journal of Chromatography B, 1052: 66–72.

Celik SE, Asfoor A, Apak R (2019) Journal of Agricultural and Food Chemistry 67 (29): 8279–8289.

Chiavaroli V, Giannini C, De Marco S, Chiarelli F, Mohn A (2011) Redox Report 16: 101–107.

Choy CKM, Benzie IFF, Cho P (2000) Biochemistry and Molecular Biology 41 (11): 3293–3298.

Davies MJ ((2016) Methods 109: 21–30.

Denardin CC, Hirsch GE, Rocha RF, Vizzotto M, Henriques AT, Moreira JCF, Guma F, Emanueloli T (2015) Journal of Food and Drug Analysis 23 (3): 387–398.

Drouet S, Doussot J, Garros L, Mathiron D, Bassard S, Favre-Réguillon, Molinié R, Lainé Éric, Hano Christophe (2018) Molecules 23 (10): 2594.

Everette JD, Bryant QM, Green AM, Abbey Y, Wangila GW, Walker R (2010) Journal of Agriculture and Food Chemistry 58 (14): 8139–8144.

Farajzadeh M, Abbaspour MA, Mogaddama MRA, Mogaddam A, Alizadeh Nabil AAAN (2016) Analytical and Bioanalytical Chemical Research 3: 239–251.

Ferrante AA, Martins IS, Silva LA, Percário S, Ferreira MES (2019) Australian Journal of Basic and Applied Sciences 13 (3): 19–22.

Floegel A, Kim D, Chung SJ, Koo SI, Chun OK (2011) Journal of Food Composition and Analysis 24: 1043—1048.

Franzoni F, Federighi G, Fusi J, Agosta V, Cerri E, Banducci R, Petrocchi A, Bernardi R, Innocenti A, Pruneti C, Daniele S, Pellegrini S, Martini C, Scuri R, Galetta F (2017) Archives Italiennes de Biologe 155: 1—10.

Gardner PT, McPhail DB, Crozier A, Duthie GG (1999) Journal of Science and Food Agriculture 79: 1011—1014.

Garrett AR, Murray BK, Robison RA, O'Neill KL (2010) Advanced protocols in oxidative stress 2: 251—262.

Goosen NJ, Ooshuizen D, Stander MA, Dabai AI, Pedavoah MM, Usman GO (2018) South African Journal of Botany 119: 11—16.

Granato D, Shahidi F, Wrolstad R, Kilmartin P, Melton LD, Hidalgo FJ, Miyashita K, Camp J, Alasalvar C, Ismail AB, Elmore S, Birch GG, Astley SB, Pegg R, Zhou P, Finglas P (2018) Food Chemistry 264: 471—475.

Gupta D (2015) International Journal of Pharmaceutical Sciences and Research 6 (2): 546—66.

Haida Z, Hakiman M (2019) Food Science & Nutrition 7 (5): 1555—1563.

Holtz RW (2009) Skin Aging Handbook: In Vitro Methods to Screen Materials for Anti-aging Effects. William Andrew, Norwich NY.

Huang D, Ou B, Prior RL (2005) Journal of Agricultural and Food Chemistry 53(6): 1841.

Huda-Faujan N, Norrakiah AS, Babji AS (2009) African Journal of Biotechnology 8 (3): 484—489.

Jiang J, Zang S, Li D, Wang K, Tian S, Yu A, Zhang Z (2018) Talanta 184: 23—28.

Jiang Y, Rakesh KP, Alharbi NS, Vivek HK, Manukumar HM, Mohammed YHE, Qin H (2019) Bioorganic Chemistry 89: 103015.

Joseph NM, Sabharwal M, Shashi A, Mahor A, Rawal S (2018) International Journal of Pharmaceutical Sciences and Research 1: 1—11.

Kamer G, Demirata B, Bayraktar R, Ozyurt D, Apak R (2019) Analytical Methods 14.

Kedare SB, Singh RP (2011) Journal of Food Science and Technology 48 (4): 412—422.

Kimáková T, Baranovičová I (2015) Léčivá síla antioxidantú. Príroda, s.r.o, Bratislava.

Klaunig JE, Wang Z (2018) Current Opinion in Toxicology 7: 116—121.

Kleschyov AL, Wenzel P, Munzel T (2007) Journal of Chromatography B: 851 (1, 2), 12—20.

Koleva II, Niederländer H, Beek TA (2000) Analytical Chemistry 73 (14): 3373—3381.

Lachowicz S, Oszmiański J, Wiśniewski R (2018) European Food Research and Technology 244: 1269—1280.

Lamuela-Raventós RM (2018) Measurement of Antioxidant Activity and Capacity: Recent Trends and Applications. John Wiley & Sons, USA.

Li D, Jiang J, Han D, Yu X, Wang K, Zang S, Lu D, Yu A, Zhang Z (2016) Analytical Chemistry 88: 3885—3890.

Li XY, Wang ZY, Wang L, Walid E, Zhang H (2012) International Journal of Molecular Science 13 (5): 5801—5817.

Lichtenthäler R, Marx F (2003) European Food Research Technology 216: 166—173.

Lim S, Choi A-H, Kwon M, Joung E, Shin T, Lee S, Kim N, Kim H (2019) Food Chemistry 278: 178—184.

Lobo V, Patil A, Chandra N (2010) Pharmacognosy Reviews 4 (8): 118—126.

Ma H, Liu T, Li J, Mingya D, Gao X, Chang Y (2019) Journal of Chromatography A 1593: 147—155.

Martín J, Kuskoski EM, Navas MJ, Asuero AG (2017) Flavonoids — From Biosynthesis to Human Health: Antioxidant Capacity of Anthocyanin Pigments. BoD — Books on Demand, Germany.

Mellado-Ortega E, Zabalgogeazcoa I, Aldana B, Arellano JB (2017) Analytical Biochemistry 519: 27—29.

Minussi RC, Rossi M, Bologna L, Cordi L, Rotilio D, Pastore G, Durán N (2003) Food Chemistry 82 (3): 409—416.

Moran-Palacio EF, Zamora-Álvarez LA, Stephens-Camacho NA, Yánez-Farías GA, Virgen-Ortiz A, Martínez-Cruz O, Rosas-Rodríguez JA (2014) Tropical Journal of Pharmaceutical Research 13 (9): 1487—1493.

Moukette BM, Pieme CA, Njimou JR, Biapa CP, Marco B, Ngogang JY (2015) Biological Research 48(1): 15.

Munialo CD, Naumovski N, Sergi D, Stewart D, Mellor DD (2019) 54 (5): 1448—1459.

Murauer A, Bakry R, Schottenberger H, Huck C, Ganzera M (2017) Analytica Chimica Acta 963: 136—142.

Nijhawan P, Arora S (2019) Obesity Medicine 15: 100—125.

Obón JM, Castellar R, Cascales JA, Fernándey-Lópey JA (2005) Food Research International 38 (8): 843—845.

Ojha K, Dubey S, Chandrakar J, Minj RA, Dehariya R, Dixit AK (2018) Research Journal of Life Sciences, Bioinformatics, Pharmaceutical and Chemical Sciences 4 (6): 707.

Okazaki S, Takeshita K (2018) Applied Magnetic Resonance 49 (8): 881—892.

Ononamadu C, Ihegboro GO, Owolarafe K, Salawu K, Fadilu M, Eyeigwe OC, Oshobu ML, Nwachukwu FC (2019) Analytical and Bioanalytical Chemical Research 6: 431—439.

Ordoudi SA, Tsimidou MZ (2006) Journal of Agricultural and Food Chemistry 54 (5): 1663—1671.

Oribayo OO, Owolabi MA, Ukpo GE, Shode FO (2018) Tropical Journal of Natural Product Research 2 (1): 18—22.

Pérez-Burillo S, Rufián-Henares JA, Pastoriza S (2018) Food Chemistry 239: 1263—1272.

Pérez-Jiménez J, Saura-Calixto F (2008) International Journal of Food Science & Technology 43 (1): 185—191.

Pisoschi AM, Negulescu G (2011) Biochemistry & Analytical Biochemistry 1 (1).

Prieto MA, Vázquez JA, Murado M (2015) Food Chemistry 167 (15): 299—310.

Prior RL (2015) Journal of Functional Foods 18 (B): 797—810.

Re R, Pellegrini N, Proteggente A, Pannala A, Yang M, Rice-Evans C (1999) Free Radical Biology and Medicine 26 (9, 10): 1231—1237.

Regoli F (2000) Aquatic Toxicology 50 (4): 351—361.

Rodriguez-Nogales J, Vila-Crespo J, Gómez M (2011) Food Chemistry 129: 1800—1805.

Sakurai Y, Yamaguchi T, Ando K, Kuwabara K, Nakajima H, Morimoto C, Yoshikawa S, Niwa M, Miyake Y, Kanaori K, Nakajim A, Tajima K (2019) Bulletin of Chemical Society of Japan 92 (7): 1218—1225.

Sánchez-Rangel JC, Benavides J, Heredia JB, Cisneros-Zevallos L, Jacobo-Velázquez (2013) Analytical Methods 5 (21): 5990—5999.

Schaich KM, Tian X, Xie J (2015) Journal of Functional Foods 18 (B): 782–796.

Seesom C, Jumepaeng T, Luthria DL, Chanthai S (2018) Journal of Food Health and Bioenvironmental Science 11 (2): 28–37.

Shalaby A (2013) African Journal of Pharmacy and Pharmacology 7 (10): 528–539.

Shekhar TC, Anju G (2014) American Journal of Ethnomedicine 1 (4): 244–249.

Shi S, Guo K, Tong R, Liu Y, Tong C, Peng M (2019) Food Chemistry 288: 215–220.

Singh S, Singh RP (2008) Food Reviews International 24 (4): 392–415.

Singleton VL, Orthofer R, Lamuela-Raventos RM (1999) Methods Enzymol. 299: 152–178.

Sotto AD, Checcon P, Celestino I, Locatelli M, Carissimi S, Angelis MD, Rossi V, Limongi D, Toniolo Ch, Martinoli L, Giacomo SD, Palamara AT, Nencioni L (2018) Oxidative Medicine and Cellular Longevity 2018: 1–14.

Sundararajan R, Ilengesan R (2018) Free Radicals and Antioxidants 8 (1): 55–61.

Thaipong K, Boonprakob U, Crosby K, Cisneros-Zevallos L, Hawkins Byrne D (2006) Journal of Food Composition and Analysis: 19 (6, 7): 669–675.

Torre A, Henderson T, Nigam PS, Owusu-Apenten RK (2015) Food Chemistry 174: 119–123.

Van Den Berg R, Bast A (1999) Food Chemistry 66 (4): 511–517.

Wan HC, Sultana B, Nigam PS, Owusu-Apenten R (2018) Beverages 4 (3): 58.

Wayner DD, Burton GW, Ingold KU, Locke S (1985) FEBS Lett. 187: 33–37.

Wong C, Li H, Cheng K, Chen F (2006) Food Chemistry 97 (4): 705–711.

Yadav A, Kumari R, Yadav A, Mishra JP, Srivastava S, Prabha S (2016) Research of Environmental and Life Science 9 (11): 1328–1331.

Yamaguchi F, Yoshimura Y, Nakazawa H, Ariga T (1999) Journal of Agricultural and Food Chemistry 47: 2544–2548.

Yan X, Murphy BT, Hammond GB, Vinson JA, Neto CC (2002) Journal of Agriculture and Food Chemistry 50 (20): 5844–5849.

Yeo JD, Shahidi F (2019) Journal of Agricultural and Food Chemistry 67: 7526–7529.

Yeum KJ, Russell RM, Krinsky NI, Aldini G (2004) Archives of Biochemistry and Biophysics 430 (1): 97–103.

Yu LL, Cheng Z (2008) Molecular Nutrition & Food Research 52: 62–78.

Zablocka A, Sokolowska A, Macala J, Bartoszewska M, Mitkiewicz M, Janusz M, Wilusz T, Polanowski A (2019) International Journal of Peptide Research and Therapeutics: 1–10.

Zang S, Tian S, Jiang J, Han D, Yu X, Wang K, Li D, Lu D, Yu A, Zhang Z (2017) Food Chemistry 221: 1221–1225.

Zhong Y, Shahidi F (2015) Food Science, Technology and Nutrition: 287–333.

Zhong Y, Shahidi F (2015) Handbook of antioxidants for food preservation: methods for the assessment of antioxidant activity in foods. Woodhead Publishing, UK.

sciendo

Antioxidant action of phenols: Revisiting theoretical calculations of their thermodynamics

Monika Biela, Bernadeta Pelikánová, Martin Michalík

Department of Chemical Physics, Slovak University of Technology in Bratislava,
Radlinského 9, SK-812 37 Bratislava, Slovakia
monika.biela@stuba.sk

Abstract: Theoretical prediction ability of M06-2X functional was tested for thermodynamics of phenol, 15 *para* and 15 *meta* phenol derivatives. Calculations were done for gas phase as well as for polar and nonpolar solvents. Although predicted values might be shifted from the experimental ones in the framework of the employed DFT functional and basis set, the calculated and experimental data sets correlate well together. Very good linearity was found especially for the correlation of experimental and theoretical proton affinities. Hammett type correlations between the environments considered were compared. The phenolic C—O bond length was also tested as an alternative substituent effect descriptor while the type and position of the functional group on the aromatic ring have a direct effect on the phenolic bond.

Keywords: DFT, Hammett constants, M06-2X functional, reaction enthalpy

Introduction

Phenols are considered as antioxidants providing protection against free radicals and as such are often utilized in forms of various derivatives. Over the last few years, three main mechanisms of radical scavenging action were proposed as shown in Fig. 1. While the final product remains the same in all of them, the number of steps and intermediates as well as the solvent preference differ. Comprehensive description of illustrated reaction paths can be found elsewhere (Rimarčík et al., 2011).

Historically, Bond Dissociation Enthalpy (BDE) is one of the earliest studied quantity in association with antioxidants with straightforward mechanism. On the other hand, the first steps in latter mechanisms are often more interesting in the kinetic studies owing to their rate-determining nature. Specifically, the ionization potential (IP) or anion proton affinity (PA) values are usually higher than those of Proton Dissociation Enthalpy (PDE) or Electron Transfer Enthalpy (ETE).

Although there have been many theoretical studies regarding antioxidant action of substituted phenols, very few of them employ M06-2X functional of the Truhlar group (Zhao et al., 2008) and even fewer of them determine solvent effects. On the other hand, there are many studies using B3LYP functional (Klein et al., 2009; Vagánek et al., 2011; Chen et al., 2015). Some of the studies are focused mainly on the HAT mechanism, correlation between BDEs or C—O bond lengths and Hammett constants (Klein et al., 2006b). Complex thermodynamics of three main mechanisms is included in other studies (Klein et al., 2006a; Chen et al., 2015).

In contrast to popular B3LYP published in 1988, M06-2X is a more recent global hybrid functional with higher (54 %) Hartree-Fock exchange. It is advertised as one of the top performers and

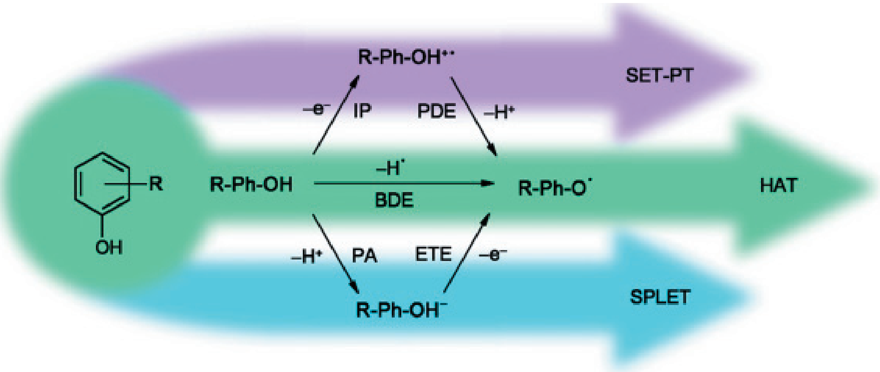

Fig. 1. Main mechanisms of antioxidant action — Sequential Electron Transfer Proton Transfer (SET-PT), Hydrogen Atom Transfer (HAT) and Sequential Proton Loss Electron Transfer (SPLET).

should be optimized for thermodynamics calculations (Zhao and Truhlar, 2008). Numerous validation studies (Huang et al., 2014; Luo et al., 2011) put this Minnesota 06 functional in a position superior to B3LYP. It should also outperform other DFT methods providing better description of medium-range exchange-correlation energies. Nevertheless, it has to be mentioned that the vast majority of benchmark studies perform statistics based on single point energies with so-called reference *theoretical* data (mostly from gas-phase coupled cluster calculations). However, the goal of all computational methods is to provide data as close to the experimental ones as possible. Also, the geometries are usually not optimized employing the DFT functional but rather just taken from MP2 of more precise calculations. In our case of monosubstituted phenols, experimental data on thermodynamics are available and thus a more relevant correlation can be done. Parameters from linear regression can be then employed for reactivity prediction. Therefore, the main goals of this work are: a) to perform geometry optimization of phenol, 15 *para* and 15 *meta* phenol derivatives (see Tables 1—2) using M06-2X functional, b) to investigate the rate determining reaction enthalpies of antioxidant mechanism for the studied compounds, c) to compare the obtained results with experimental data, and d) to find relationships between Hammett constants and reaction enthalpies.

Computational details

All geometry optimizations were performed in the Gaussian 16 program package (Frisch et al., 2016) at DFT level of theory with the M06-2X (Zhao et al., 2008) hybrid functional as implemented in Gaussian. Energy cut-off was 10^{-5} kJ mol^{-1} and final RMS energy gradient was below 0.01 kJ mol^{-1} A^{-1}. For all atoms, triple zeta 6-311++G(d,p) basis sets were employed (Hariharan et al., 1973; Rassolov et al., 1998). The chosen basis sets are assumed to provide reliable molecular geometries and reaction enthalpies and are generally considered to be sufficiently large (Michalík et al., 2014; Škorňa et al., 2014). Influence of the water and benzene solvents was approximated by implicit continuum model SMD (Marenich et al., 2009). The optimized structures were confirmed to be real minima by vibrational analysis (no imaginary frequencies).

Based on optimized structures, thermodynamic quantities for the processes mentioned in Fig. 1, i.e. bond dissociation enthalpies (BDE), ionization potentials (IP), anion proton affinity (PA) were calculated at room temperature as follows

$$\mathrm{BDE} = H(\mathrm{Ph{-}O^{\bullet}}) + H(\mathrm{H^{\bullet}}) - H(\mathrm{Ph{-}OH}) \qquad (1)$$

$$\mathrm{IP} = H(\mathrm{Ph{-}OH^{\bullet+}}) + H(\mathrm{e^{-}}) - H(\mathrm{Ph{-}OH}) \qquad (2)$$

$$\mathrm{PA} = H(\mathrm{Ph{-}O^{-}}) + H(\mathrm{H^{+}}) - H(\mathrm{Ph{-}OH}) \qquad (3)$$

where $H(\mathrm{Ph{-}OH})$ represents the total enthalpy of the phenol derivative, $H(\mathrm{Ph{-}OH^{\bullet+}})$ is the total enthalpy of the phenol radical cation, $H(\mathrm{Ph{-}O^{\bullet}})$ and $H(\mathrm{Ph{-}O^{-}})$ are the total enthalpies of the phenoxy radical and the phenoxide anion, respectively. In water, enthalpy of proton $H(\mathrm{H^{+}})$ is –1049.60 kJ mol^{-1}, in benzene it is –853.71 kJ mol^{-1}. The latter was estimated as the enthalpy of the reaction $C_6H_6(l) + H^{+}(g) \rightarrow (C_6H_6)^{+}(solv)$ in benzene. Enthalpy of hydrogen atom $H(\mathrm{H^{\bullet}})$ in benzene is –1301.02 kJ mol^{-1}, in gas phase it is –1301.81 kJ mol^{-1} and in water it is –1296.26 kJ mol^{-1}. Finally, the calculated enthalpy of electron $H(\mathrm{e^{-}})$ in benzene is –8.20 kJ mol^{-1} while in water it is –74.75 kJ mol^{-1}. All these values were also calculated in this study at the M06-2X/6-311++G** level.

Relevant values from the statistical analysis were rounded and are presented with the corresponding standard deviations of the last digit shown in parenthesis. The goodness of fit of a statistical model is characterized by correlation coefficient R.

Results and Discussion

The main aim of our work was to predict experimental values as best as possible; therefore, the correlation between proton affinities measured on a pulsed ion cyclotron resonance (ICR) mass spectrometer (Fujio et al., 1981) and theoretical gas phase PAs were first investigated. This should proof that the employed DFT functional and basis set provide reliable results. PAs were chosen because, unlike other quantities, as many as 25 various *meta* and *para* phenol derivatives show gas phase acidity measured under the same experimental conditions. Tables 1 and 2 list gas phase and solvent phase values calculated in this study. Significant solvent dependence of proton affinity can be attributed mainly to substantial differences in proton enthalpy. Nevertheless, the correlation of 25 experimental PA(exp) values and the present PA(DFT) in gas phase show excellent linearity ($R = 0.998$) and linear equation:

$$\begin{aligned}\mathrm{PA(exp)/kJ\ mol^{-1}} &= 0.12(2)\cdot 10^{3} + \\ &+ 0.92(2)\cdot \mathrm{PA(DFT)/kJ\ mol^{-1}}\end{aligned} \qquad (4)$$

Prediction for other derivatives can be therefore made with great confidence using this equation. From Equation (4) it is evident that theoretical proton affinities are slightly underestimated with respect to the experimental absolute values. Very similar linearity (R = 0.997) as well as slope of 0.90(2) and intercept of $0.15(3) \cdot 10^3$ were found in a previous study (Klein and Lukeš, 2006a) that employed B3LYP and the same basis set, 6-311++G**.

On the other hand, experimental BDEs tend to vary quite wildly from one method to another (see e.g. the comparison in Klein and Lukeš, 2006b) making any direct comparison and data merging troublesome. Thus, a comparison with electrochemical measurements done by Bordwell et al. (1991) compiling 21 experimental values was applied. M06-2X data correlate fairly well with R = 0.968 with the linear equation of:

$$\mathrm{BDE(exp)/kJ\ mol^{-1}} = \\ = 0.06(2) \cdot 10^3 + 0.83(5) \cdot \mathrm{BDE(DFT)/kJ\ mol^{-1}} \qquad (5)$$

The same correlation, but with B3LYP functional employed, results in the intercept of

Tab. 1. M06-2X/6-311++G** thermodynamic quantities defined by Eqs. (1)–(3) for phenols substituted with *X* in *meta* position in various environments. All values are in kJ mol^{-1}.

X	Water			Benzene			Gas		
	BDE	**PA**	**IP**	**BDE**	**PA**	**IP**	**BDE**	**PA**	**IP**
Br:	385	150	692	374	453	728	374	1414	839
CF_3:	387	149	697	376	449	744	377	1406	866
Cl:	385	150	688	374	453	723	375	1419	838
CN:	390	146	703	379	438	752	380	1394	880
F:	384	151	687	374	457	725	375	1427	848
Me:	373	162	660	366	482	689	368	1456	802
MeCO:	385	154	687	374	464	723	376	1426	838
MeO:	381	158	660	373	479	682	375	1451	792
$MeSO_2$:	391	143	708	379	438	749	381	1391	867
NH_2:	370	163	601	365	483	623	369	1459	742
NMe_2:	370	164	579	365	487	591	369	1459	700
NO_2:	396	145	715	381	430	764	381	1387	891
OH:	376	157	656	368	471	687	369	1443	801
Ph:	378	159	668	369	472	685	370	1437	785
***t*-But:**	376	164	664	367	483	688	369	1452	795

Tab. 2. M06-2X/6-311++G** thermodynamic quantities defined by Eqs. (1)–(3) for phenols substituted with *X* in *para* position in various environments. All values are in kJ mol^{-1}.

X	Water			Benzene			Gas		
	BDE	**PA**	**IP**	**BDE**	**PA**	**IP**	**BDE**	**PA**	**IP**
Br:	379	154	680	367	457	705	367	1419	811
CF_3:	395	148	709	382	438	752	382	1396	871
Cl:	377	154	675	365	459	704	366	1425	814
CN:	395	138	709	381	421	752	380	1376	870
F:	371	159	667	361	470	702	362	1441	819
Me:	364	165	646	358	485	669	361	1459	780
MeCO:	390	140	696	376	437	727	376	1394	837
MeO:	341	162	610	342	490	636	346	1459	740
$MeSO_2$:	400	137	720	383	424	760	386	1372	873
NH_2:	320	171	564	324	496	584	332	1468	696
NMe_2:	315	168	548	319	487	555	327	1455	659
NO_2:	403	122	728	386	401	778	387	1354	900
OH:	350	167	622	344	486	651	347	1461	760
Ph:	367	158	644	359	462	655	361	1426	750
***t*-But:**	366	165	649	359	484	671	362	1453	773
H:	377	160	671	368	477	703	370	1453	818

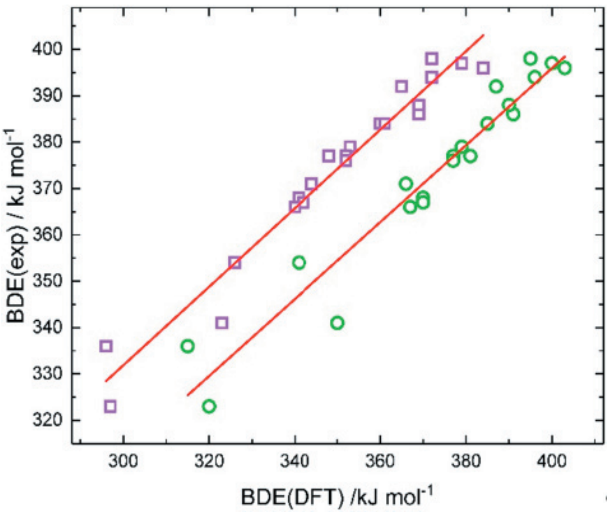

Fig. 2. Correlation between experimental (Bordwell et al., 1991) bond dissociation enthalpies BDE(exp) and theoretical BDE(DFT). Relationship with B3LYP data (Klein and Lukeš, 2006b) is represented by violet squares, green circles represent M06-2X data of this study.

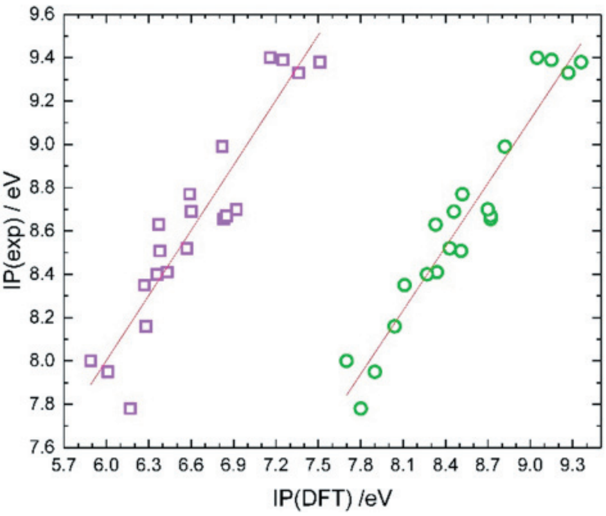

Fig. 3. Correlation between experimental ionization potentials IP(exp) compiled by Klein and Lukeš, 2006c and theoretical IP(DFT). Relationship with B3LYP data is represented by violet squares, green circles represent M06-2X data of this study.

$0.08(2) \cdot 10^3$ kJ mol^{-1}, provided virtually the same slope of 0.85(4) and slightly better correlation coefficient R = 0.978. The linear trends are plotted and compared graphically in Fig. 2.

Gas phase ionization potential measurements are laborious requiring costly apparatus therefore compilations of more than few derivatives are scarce. Experimental data of more than ten works was summarized by Klein and Lukeš, 2006c. The authors found theoretical B3LYP ionization potentials rather shifted from experimental values but substituent induced changes were well predicted. On the other hand, M06-2X values are closer to the experimental ones with relatively good correlation coefficient of R = 0.964. Regression analysis provided the linear equation of:

$$\mathrm{IP(exp)/eV} = \\ = 0.3(6) + 0.98(7) \cdot \mathrm{IP(DFT)/eV} \qquad (6)$$

In analogous correlation with B3LYP data the slope reached 1.00(9) which is still within M06-2X interval. The shift of B3LYP values is best resembled by intercept of 2.0(6) and slightly worse correlation (R = 0.935) shown in Fig. 3.

Hammett type correlations were explored next as an, to some extent, pseudo-validation tool. In the study of benzoic acids ionization, Hammett proposed (Hammett, 1937) substituent-specific constant σ as a reliable substituent effect descriptor. This constant remains popular up to now, finding its use in various correlations including derivatives far beyond benzoic acids. Prediction of equilibrium and rate constants for different types of reactions can be often made with great accuracy. A comprehensive list of Hammett σ constants is available (Hansch et al., 1991) from where the data for the functional groups in this study were taken.

In Tab. 3, linear parameters as well as correlation coefficients R obtained from linear regression can be found for *para* substituted phenols, while analogous results for *meta* substituted derivatives are presented in Tab. 4.

In case of ionization potentials *vs*. Hammett constant dependence, the values for *meta*-amino and *meta*-dimethylamino phenol were significantly off the linear trend and therefore they were omitted. Without neglecting these data, correlation coefficients would be of 0.853 in water, 0.884 in benzene

Tab. 3. Regression parameters for Hammett correlation ($y = a \cdot \sigma_p + b$) in *para* derivatives.

Environment		**Water**			**Benzene**			**Gas**	
y **=**	**BDE**	**PA**	**IP**	**BDE**	**PA**	**IP**	**BDE**	**PA**	**IP**
a/kJ mol^{-1}	53(4)	–26(3)	105(6)	40(3)	–55(6)	125(8)	36(3)	–70(8)	133(9)
b/kJ mol^{-1}	365(2)	156(2)	649(3)	357(2)	465(3)	678(4)	361(2)	1431(4)	788(5)
R	0.968	0.919	0.974	0.967	0.931	0.972	0.967	0.918	0.964

Tab. 4. Regression parameters for Hammett correlation ($y = a \cdot \sigma_m + b$) in *meta* derivatives.

Environment	Water			Benzene			Gas		
y =	BDE	PA	IP	BDE	PA	IP	BDE	PA	IP
a/kJ mol^{-1}	26(2)	−25(2)	74(7)	18(1)	−64(4)	109(11)	15(2)	−86(6)	132(14)
b/kJ mol^{-1}	375,4(6)	160,2(5)	661(3)	367,9(4)	478(2)	686(4)	370,2(6)	1449(3)	794(6)
R	0.981	0.981	0.943*	0.979	0.975	0.940*	0.945	0.970	0.925*

*values for NH_2 and NMe_2 derivatives were omitted

Tab. 5. Optimized (M06-2X/6-311++G**) phenolic C—O bond length in various environments and Hammett substituent constants (Hansch et al., 1991).

X	Meta d(C—O)/Å			Para d(C—O)/Å			σ_m	σ_p
	Water	Benzene	Gas	Water	Benzene	Gas		
Br:	1.3670	1.3570	1.3591	1.3687	1.3582	1.3603	0.39	0.23
CF_3:	1.3664	1.3563	1.3580	1.3629	1.3540	1.3562	0.43	0.54
Cl:	1.3670	1.3571	1.3589	1.3692	1.3588	1.3609	0.37	0.23
CN:	1.3656	1.3553	1.3573	1.3589	1.3515	1.3542	0.56	0.66
F:	1.3668	1.3569	1.3591	1.3729	1.3615	1.3637	0.34	0.06
Me:	1.3735	1.3616	1.3633	1.3757	1.3630	1.3644	−0.07	−0.17
MeCO:	1.3696	1.3585	1.3600	1.3610	1.3540	1.3563	0.38	0.50
MeO:	1.3709	1.3602	1.3618	1.3737	1.3656	1.3673	0.12	−0.27
$MeSO_2$:	1.3640	1.3551	1.3571	1.3582	1.3521	1.3544	0.60	0.72
NH_2:	1.3735	1.3612	1.3630	1.3814	1.3678	1.3690	−0.16	−0.66
NMe_2:	1.3752	1.3627	1.3647	1.3784	1.3657	1.3671	−0.16	−0.83
NO_2:	1.3634	1.3542	1.3562	1.3531	1.3492	1.3522	0.71	0.78
OH:	1.3703	1.3596	1.3613	1.3781	1.3656	1.3671	0.12	−0.37
Ph:	1.3721	1.3608	1.3626	1.3713	1.3601	1.3620	0.06	−0.01
***t*-But:**	1.3748	1.3625	1.3642	1.3749	1.3627	1.3639	−0.10	−0.20
H	1.3727	1.3609	1.3626	1.3727	1.3609	1.3626	0.00	0.00

and 0.901 in gas phase. In case of *para* derivatives and proton affinities, the relationship excluding values for dimethylamino and unsubstituted phenol provided significantly better correlation coefficient of 0.962 in benzene. It should be mentioned that the interval of published σ_p values for the dimethylamino group is one of the largest ones and even a value with a relatively high standard error of −0.6 ±0.2 has been suggested (Jaffé, 1953). Moreover, in case of NMe_2 compared to the vast majority of substituents, an exceptionally large charge transfer with OH group was observed (Nazarparvar, 2012). Apart from these exceptions, our correlations involved all 15 derivatives and the value for unsubstituted phenol. Considering this number of points for statistics, the found correlation coefficients can be regarded as satisfactory.

Alternative descriptor in case of monosubstituted phenols seems to be the length of phenolic C—O bond which was found to be sensitive to the substituent both in *para* and *meta* positions. Also, the higher the value of the Hammett constant, the shorter the C—O bond becomes. These lengths obtained from the optimized geometries are presented in Tab. 5 and potentially can be also obtained from X-ray diffraction experiments.

When the bond length is used for correlations, unlike Hammett constants, the values for *meta* and *para* derivatives lie on a single line. Especially good linearity (R = 0.989) was found for the relationship between 31 values of proton affinities in water and *d*(C—O) bond lengths optimized in water. The linear equation reads:

$$\begin{aligned} &\mathrm{PA/kJ\ mol^{-1}} = \\ &= -2.13(7) \cdot 10^3 + 1.67(5) \cdot d(\mathrm{C{-}O})/\text{Å} \qquad (7) \end{aligned}$$

This equation potentially enables relevant prediction of solvent based PAs. For phenol derivatives, this kind of experimental data is still scarce.

Conclusion

In this paper, results of quantum chemical thermodynamics calculations have supported the viability of the newer hybrid M06-2X functional. Theoretical reaction enthalpies tend to be slightly underestimated with respect to the experimental absolute values, but substituent induced changes are well predicted by the present method. Based on the presented correlations it can be concluded that the DFT/M06-2X method with employed Pople type basis set 6-311++G(d,p) provides thermodynamic values in good agreement with experimental data. No considerable major differences between B3LYP and M06-2X were found in terms of correlation slopes, but the B3LYP functional tends to provide slightly more shifted values. Therefore, the Minnesota 06 hybrid functional which has become widely adopted in recent years seems to be a reasonable alternative to the robust and most popular B3LYP one.

Acknowledgement

We are grateful to the HPC center at the Slovak University of Technology in Bratislava, which is a part of the Slovak Infrastructure of High Performance Computing (SIVVP project, ITMS code 26230120002, funded by the European region development funds, ERDF) for the computational time and resources made available.

References

Becke AD (1988) Phys. Rev. A. 38: 3098.

Bordwell FG, Cheng J (1991) J. Am. Chem. Soc. 113: 1736–1743.

Chen Y, Xiao H, Zheng J, Liang G (2015) PLoS One, 10: e0121276.

Francl MM, Pietro WJ, Hehre WJ, Binkley JS, Gordon MS, DeFrees DJ, Pople JA (1982) J. Chem. Phys. 77: 3654–3665.

Frisch MJ, Trucks GW, Schlegel HB, Scuseria GE, Robb MA, Cheeseman JR, Scalmani G, Barone V, Petersson GA, Nakatsuji H, Li X, Caricato M, Marenich AV, Bloino J, Janesko BG, Gomperts R, Mennucci B, Hratchian HP, Ortiz JV, Izmaylov AF, Sonnenberg JL, Williams-Young D, Ding F, Lipparini F, Egidi F, Goings J, Peng B, Petrone A, Henderson T, Ranasinghe D, Zakrzewski VG, Gao J, Rega N, Zheng G, Liang W, Hada M, Ehara M, Toyota K, Fukuda R, Hasegawa J, Ishida M, Nakajima T, Honda Y, Kitao O, Nakai H, Vreven T, Throssell K, Montgomery JA Jr., Peralta JE, Ogliaro F, Bearpark MJ, Heyd JJ, Brothers EN, Kudin KN, Staroverov VN, Keith TA, Kobayashi R, Normand J, Raghavachari K, Rendell AP, Burant JC, Iyengar SS, Tomasi J, Cossi M, Millam JM, Klene M, Adamo C, Cammi R, Ochterski JW, Martin RL, Morokuma K, Farkas O, Foresman JB and Fox DJ (2016) Gaussian 16, Revision B.01, Gaussian, Inc. Wallingford CT.

Fujio M, McIver Jr RT, Taft RW (1981) J. Am. Chem. Soc. 103: 4017–4029.

Hammett LP (1937) J. Am. Chem. Soc. 59: 96–103.

Hansch C, Leo A, Taft RW (1991) Chem. Rev. 91: 165–195.

Hariharan PC, Pople JA (1973) Theor. Chim. Acta. 28: 213–222.

Huang F, Jiang J, Wen M, Wang ZX (2014) J. Theor. Comput. Chem. 13: 1350074.

Jaffé HH (1953) Chem. Rev. 53: 191–261.

Klein E, Lukeš V (2006a) J. Phys. Chem. A, 110: 12312–12320.

Klein E, Lukeš V (2006b) J. Mol. Struct.(THEOCHEM) 767: 43–50.

Klein E. Lukeš V (2006c) Chem. Phys. 330: 515–525.

Klein E, Rimarcik J, Lukes V (2009) Acta Chim. Slovaca, 2: 37–51.

Lee C, Yang W, Parr RG (1988) Phys. Rev. B. 37: 785.

Luo S, Zhao Y, Truhlar DG (2011) Phys. Chem. Chem. Phys. 13: 13683–13689.

Marenich AV, Cramer CJ, Truhlar DG (2009) J. Phys. Chem. B. 113: 6378–6396.

Michalík M, Vagánek A, Poliak P (2014) Acta Chim. Slovaca. 7: 123–128.

Nazarparvar E, Zahedi M, Klein E (2012) J. Org. Chem. 77: 10093–10104.

Peverati R, Truhlar DG (2011) J. Phys. Chem. Lett. 2: 2810–2817.

Rassolov VA, Pople JA, Ratner MA, Windus TL (1998) J. Chem. Phys. 109: 1223–1229.

Rimarčík J, Lukeš V, Klein E, Rottmannová L (2011) Comp. Theor. Chem. 967: 273–283.

Škorňa P, Lengyel J, Rimarčík J, Klein E (2014) Comput. Theor. Chem. 1038: 26–32.

Vagánek A, Rimarcik J, Lukes V, Rottmannová L, Klein E (2011) Acta Chim. Slovaca 4: 55–71.

Zhao Y, Truhlar DG (2008) Theor. Chem. Acc. 120: 215–241.

sciendo

Neural network based explicit MPC for chemical reactor control

Karol Kiš, Martin Klaučo

Slovak University of Technology in Bratislava,
Radlinského 9, SK-812 37 Bratislava, Slovak Republic
karol.kis@stuba.sk

Abstract: In this paper, implementation of deep neural networks applied in process control is presented. In our approach, training of the neural network is based on model predictive control, which is popular for its ability to be tuned by the weighting matrices and for it respecting the system constraints. A neural network that can approximate the MPC behavior by mimicking the control input trajectory while the constraints on states and control input remain unimpaired by the weighting matrices is introduced. This approach is demonstrated in a simulation case study involving a continuous stirred tank reactor where a multi-component chemical reaction takes place.

Keywords: model predictive control, artificial neural networks, process control, continuous stirred tank reactor

Introduction

Chemical reactors play an essential role in the chemical and petrochemical industry. Their vast presence in the industrial world makes control synthesis very attractive for researchers. In recent years, several new control approaches have emerged mainly from the optimal control theory, as discussed by Smets et al. (2004); Pourdehi and Karimaghaee (2018); Bakošová et al. (2012). The optimal control theory proved to be very promising due to its natural ability to cope with technological constraints and to follow a performance criterion, which defines the overall economy of the production.

Designers of control strategies for chemical reactors must cope with several obstacles, mainly the natural instability of the process, e.g., exothermic reactors, and keeping the process variables in their designed steady state. Alongside which, the controller has to be able to decrease the energy consumption and increase the quality of the product. All control objectives can be incorporated in an optimal control problem (OCP) (Bakošová and Oravec, 2014; Singh et al., 2010; Bakošová et al., 2017). The model predictive control (MPC) technique is often used in such control tasks (Prasath et al., 2010), since its construction is straight-forward (Maciejowski, 2002).

The core concept of MPC is to predict future evolution of the controlled variables based on current measurements. Then, with respect to a quality criterion (usually energy consumption), MPC optimizes the values of the manipulated variables so that the criterion is minimized (Klaučo and Kvasnica, 2019). Even though it seems that MPC is one of the best controllers, it has several drawbacks. Since it is an optimization-based controller, it requires a repeated solution to an optimal control problem. Such an arrangement is virtually impossible to implement in the industry or on the computers responsible for the chemical reactor operation.

Traditional way of coping with this limitation is to consider explicit model predictive control (EMPC), an analytical solution to the optimal control problem (Bemporad et al., 2002). The control law given by the explicit solution is in form of the piecewise affine function (PWA) (Borrelli et al., 2017). Such control law can be easily evaluated at any given time without the need to involve an optimization procedure. In other words, it allows replacing the optimization solver with function evaluation. EMPC, unfortunately, can be constructed only for small-sized systems with short prediction horizons, which is a significant limitation in process industries, where prediction horizons are long.

This paper proposes an alternative to the explicit controller based on neural networks. The neural network is a powerful mathematical concept capable of approximating an arbitrary continuous function (Hornik, 1991). Here, approximation of the explicit control law given by the fullfidelity MPC is proposed. Since the traditional explicit model predictive control resulting in PWA function is not considered, the length of the prediction horizon nor the size of the controlled system are not limiting factors. Similar work has been done by Karg and Lucia (2018) or by Lohr et al. (2019). In this paper, however, we focus on the application in chemical technology, mainly the control of multicomponent chemical reaction.

Theoretical

Firstly, optimal control problem (OCP) that stands for the model predictive controller is presented.

The second part of this section is devoted to the artificial neural network to substitute the model predictive controller.

Model Predictive Control

Standard formulation of the model predictive controller utilizes a linear time-invariant model that captures the dynamics of the controlled process. Specifically, discrete-time dynamics were considered:

$$x(t+T_S) = Ax(t) + Bu(t), \tag{1a}$$

$$y(t) = Cx(t) + Du(t), \tag{1b}$$

where $x \in \mathbb{R}^{nx}$ stands for process state variables, vector $u \in \mathbb{R}^{nu}$ represents manipulated variables and $y \in \mathbb{R}^{nu}$ depicts the output variable. Matrices $A \in \mathbb{R}^{nx \times nx}$, $B \in \mathbb{R}^{nx \times nu}$, $C \in \mathbb{R}^{ny \times nx}$, and $D \in \mathbb{R}^{ny \times nu}$ were obtained from a dynamical model representing an actual controlled process using the first order Taylor expansion. The discrete time linear model (1) was discretized with the sampling period of T_S. The model predictive control was then constructed as follows

$$\min_{u_0,\dots,u_{N-1}} \sum_{k=0}^{N-1} y_k^{\mathrm{T}} Q y_k + \sum_{k=0}^{N-1} u_k^{\mathrm{T}} R u_k, \tag{2a}$$

$$\text{s. t. } x_{k+1} = Ax_k + Bu_k,\ k = 1, \dots, \mathrm{N} - 1, \tag{2b}$$

$$y_k = Cx_k + Du_k,\ k = 1, \dots, \mathrm{N} - 1, \tag{2c}$$

$$x_0 = x(t) \tag{2d}$$

$$y_{\min} \le y_k \le y_{\max},\ k = 1, \dots, \mathrm{N} - 1, \tag{2e}$$

$$u_{\min} \le u_k \le u_{\max},\ k = 1, \dots, \mathrm{N} - 1, \tag{2f}$$

where N denotes the prediction horizon. Cost function (2a) is in form of convex quadratic function with positive definite tuning factors $Q \in \mathrm{R}^{nx \times nx}$ and $R \in \mathrm{R}^{nu \times nu}$. The objective function is posed so that the controlled variables are driven towards the steady-state. Moreover, technological constraints were defined as min-max limits on controlled as well as on manipulated variables, as in (2e) and (2f), respectively. The optimization problem is initialized with the measurement of $x(t)$. MPC is formulated as a quadratic optimization problem with linear constraints. Optimal solution to the MPC in (2) yields an optimal sequence of manipulated variables $[u^*_0, \dots, u^*_{\mathrm{N}-1}]^{\mathrm{T}}$. Since OCP is a convex optimization problem, its solution is a global minimum.

The process is controlled by the model predictive controller using an algorithm called receding horizon policy, presented and proven by Mayne et al. (2000):

1. Measure system process variables $x(t)$ (e.g. temperature or concentration).
2. Initialize MPC in (2) with $x(t)$.
3. Solve quadratic optimization problem.
4. Apply manipulated variable u_0.
5. After T_S continue from step 1.

We refer to this algorithm as to a closed-loop implementation of MPC. The bottleneck of the algorithm is step No. 3, where an optimization problem has to be solved. In average industrial applications, this is an impossible task since there are no machines capable of solving a complex mathematical problem, and the solver imposes additional costs.

In the next section, replacement of such an algorithm with neural network is discussed, in order to substitute the complex procedure of mathematical optimization performed with every sampling.

Artificial Neural Networks

A neural network is a mathematical function that maps inputs $z \in \mathbb{R}^{nz} \to w \in \mathbb{R}^{nw}$ via interconnected monotone functions. Structure of the neural network is visualized in Figure 1, where each green and red dot represents the monotone function, also called as activation functions, and they are given as

$$\varphi(\alpha, z) = \frac{2}{1 + \mathrm{e}^{\alpha z}} - 1, \tag{3}$$

where z denotes an aggregated input to each node while α is a tuning parameter of the activation function. Blue dots stand for linear output layer.

Neural network is capable of approximating any arbitrary continuous functions with a very high confidence number, as discussed by Hornik (1991). Another significant advantage is the explicit nature of the neural net. Once a neural net of suitable properties is constructed, it can be evaluated on moderate hardware and hence no optimization solver is needed. Another main advantage is that the neural net is in no way limited by the length of the prediction horizon or by the size of the system, as it is in explicit model predictive control. The structure of an NN-based controller with α values determines the goodness of the PWA control law approximation. The procedure of getting weights is called training of the neural network and it is performed for a fixed structure of the neural net and thus, only the weights are calculated.

To give the reader an illustration on how the weights are calculated, consider

$$\min_{\alpha} \sum_{k=1}^{n_k} (\tilde{w}_k - \varphi(\alpha, z_k))^2. \tag{4}$$

The optimization problem (4) is a sum-of-squares data fitting problem. Solution to (4) gives opti-

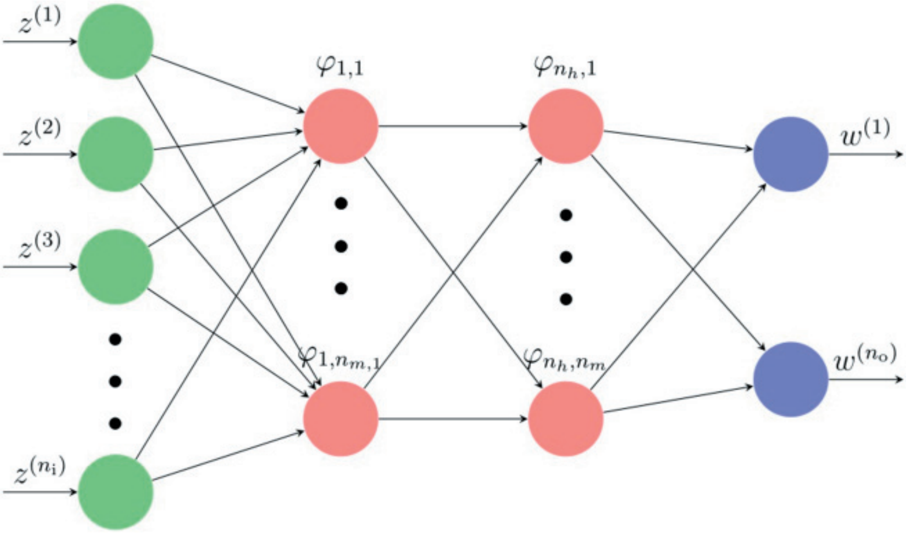

Fig. 1. Example of the neural network structure. Green points represent the input layer, red dots depict hidden layers, and the output layer is blue.

mal values of weight α based on minimizing the squared distance between a target value, $\tilde{w}$, and the evaluated activation function, $\varphi(\alpha, z_k)$, for a given neural network input. Naturally, to increase the goodness of the α value, a sufficient number of data points has to be included in the minimization procedure. Here, n_k denotes the number of these data points.

Since the neural network substitutes the controller, measurements of the process variables $x(t)$ are the input to the training of the NN-based controller, and control inputs, i.e., the manipulated variable $u(t)$, are the training targets. To provide a suitable basis for the training procedure, an initial training set was given as

$$\mathcal{X} = [x_{\mathrm{min}}, \ldots, x_{\mathrm{max}}], \tag{5}$$

where the limits on the process variables with n_k points form an equidistant grid. Subsequently, for each data point in $\mathcal{X}$, a corresponding control action was calculated and a set $\mathcal{U}$ with n_k different manipulated variables was obtained. The corresponding control actions were obtained by solving the MPC problem (2) initialized with x_0 from (2g) equal to one of the points from $\mathcal{X}$. Sets $\mathcal{X}$ and $\mathcal{U}$ together form a learning data set, from which the minimization problem (4) is constructed. Note that problem (4) is presented only for one node in the hidden layer, the overall training procedure consists of an aggregated minimization problem, where all nodes are included.

Numerically, the optimal control actions are obtained using the GUROBI solver, while the training procedure is performed with the *Deep Learning Toolbox* in MATLAB. Furthermore, the model predictive controller is formulated using the YALMIP toolbox (Lofberg, 2004).

Experimental

The theory presented in the Theoretical part of the paper was applied in a case study involving the control of a multi-component chemical reactor. Specifically, we considered benchmark chemical reaction

$$\mathrm{A} \rightleftarrows \mathrm{B} \rightarrow \mathrm{C}, \tag{6}$$

with dynamical behavior given by three differential equations (Fissore, 2008; Bakaráč and Kvasnica, 2018) leading to

$$\dot{c}_A = -k_1 c_{\mathrm{A}} + \frac{F}{V}\left(c_{\mathrm{A,\,feed}} - c_{\mathrm{A}}\right) - k_2 c_{\mathrm{C}}^2, \tag{7a}$$

$$\dot{c}_B = -\frac{F}{V} c_{\mathrm{B}} - k_3 c_{\mathrm{C}}^2, \tag{7b}$$

$$\dot{c}_C = k_1 c_{\mathrm{A}} + \frac{F}{V} c_{\mathrm{C}} - \left(k_2 + k_3\right) c_{\mathrm{C}}^2 + q_{in}. \tag{7c}$$

Process variables are concentrations $x = [c_{\mathrm{A}}, c_{\mathrm{B}}, c_{\mathrm{C}}]^\top$, while the manipulated variables, q_{in}, stands for molar feed of component C. Specific parameters of the benchmark model of chemical reactor are reported in Table 1. Objective of the controller was to keep the concentration, c_B, at a steady state level, which represents the optimal conditions of the reactor operation as introduced by Fissore (2008).

Concretely, the optimal operation of the chemical reactor is given by a set of steady-state values of individual process variables, and they are given as

Tab. 1. Table of model parameters.

Variable	**Value**	**Unit**
k_1	1	$m^3\,mol^{-1}\,s^{-1}$
k_2	3	$m^3\,mol^{-1}\,s^{-1}$
k_3	5	$m^3\,mol^{-1}\,s^{-1}$
F	3	$m^3\,s^{-1}$
V	3	m^3
$c_{A,\,feed}$	2	$mol\,m^{-3}$

$$c_{A,\,S} = 2.18\ \text{mol m}^{-3},\ c_{B,\,S} = 3.93\ \text{mol m}^{-3},\ c_{C,\,S} = 0.87\ \text{mol m}^{-3}, \tag{8}$$

while the steady-state manipulated variables were set to $q_{in,\,S} = 5$ mol s^{-1}.

Next, the model predictive controller was constructed with linearized version of the dynamical mathematical model, sampled with $T_S = 0.1$ s.

Matrices of the discretized state-space model take the form:

$$A = \begin{bmatrix} 0.83 & 0 & 0.24 \\ 0.03 & 0.90 & 0.43 \\ 0.05 & 0 & 0.23 \end{bmatrix}, \quad B = \begin{bmatrix} 0.02 \\ 0.03 \\ 0.05 \end{bmatrix}, \quad C = \begin{bmatrix} 0 & 1 & 0 \end{bmatrix}. \tag{9}$$

MPC was set up with the prediction horizon $N = 50$, while the tuning factors were set to $Q = 10$ and $R = 0.15$. The constraints were again reproduced from the benchmark model where $0 \leq c_A \leq 10$, $0 \leq c_B \leq 14$, and $0 \leq c_C \leq 1.1$. Molar feed-flow of q_{in} was constrained to the interval of $[0, 10]$ mol s^{-1}.

Learning set for the neural network was then constructed. Each interval for the process variables was split into 10000 samples, for which the corresponding optimal value of the manipulated variable was determined. Such a training set was then fed into the *Deep Learning Toolbox*, particularly, the **fitnet** com-

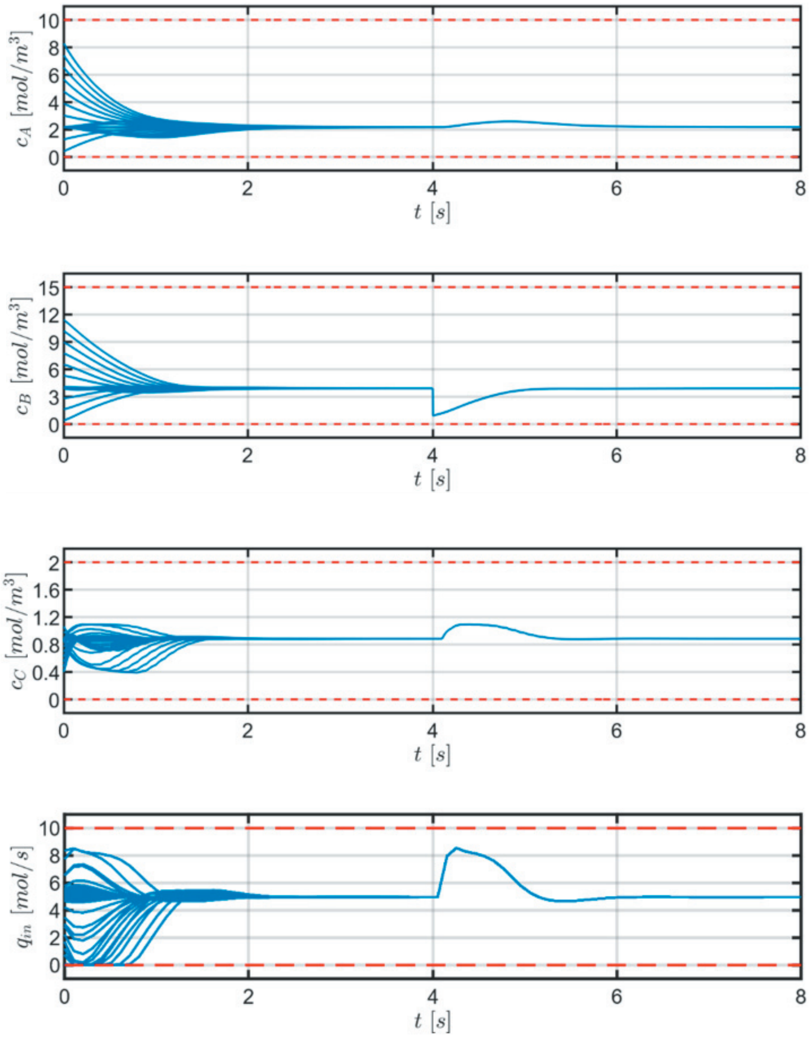

Fig. 2. Control performance of the NN-based controller with various initial conditions.

mand, which trained the neural network. Structure of the NN-based controller consists of three nodes in the input layer (due to three individual measurements of the process variable) and from four hidden layers. Each hidden layer consists of four nodes, each in form of the action function, as in (3). The final output layer has linear structure and consists of one node. Recall that the output from the neural network is the manipulated variable. The training was done offline, and it took 80 s on a personal computer with Core i7, 16 GB of RAM, and Matlab R2019a. The resulting neural network controller takes less than 7 kB of memory and can be evaluated in milli-second range on ARM processors. Such a characteristic is in strong contrast to the optimization procedure required by the MPC strategy. Finally, applicability of the NN-based controller was evaluated and tested. A large scale test scenario was prepared, involving 600 simulations, each starting from a different initial condition. Thus, the performance of the NN-based controller can be easily observed. Furthermore, artificial disturbance to the controller variable was introduced to present that the NN-based controller can also effectively cope with disturbances.

Adherence of the bounds on the process and manipulated variables has to be especially pinpointed. Control scenarios can be seen in Figure 2, but only a subset of the 600 simulations is shown to make the figure readable. Also, all simulations are performed using the full-fidelity non-linear model presented in (7).

Even though the performance of the NN-controller is, in terms of the

$$J = \sum_{t=0}^{t_{\mathrm{sim}}} \left\| x(t) - x_S \right\|_2^2, \tag{10}$$

simulations, satisfactory, a quality criterion of the following form was also evaluated to indicate how far the actual measurement of process variables was from the desired steady-state value. For all 600 simulations, the J value was evaluated and compared with the value of the criterion from the model predictive control performance. The worst decrease in the suboptimality was 2.14 %.

Conclusions

The paper discussed the design of suboptimal control law in form of a neural network. The main advantage of this controller is its explicit form, which was constructed for a large prediction horizon. The neural network was constructed based on data obtained from the optimal solution to a full-fidelity model predictive controller. Applicability of the suboptimal controller was tested on a large-scale simulation case study involving the stabilization of multi-component chemical reaction. Simulation results showed that in 94.5 % of cases, the NN-based explicit controller performed with the optimality decrease below 1 %.

Acknowledgments

The authors gratefully acknowledge the contribution of the Scientific Grant Agency of the Slovak Republic under the grant 1/0585/19. This work was supported by the funding of the Slovak Ministry of Education, Science, Research and Sport under the project STU as the Leader of Digital Coalition 002STU-2-1/2018. M. Klaučo would like to thank for the financial contribution from the STU Grant Scheme for Excellent Research Teams.

References

Bakaráč P, Kvasnica M (2018) Fast nonlinear model predictive control of a chemical reactor: a random shooting approach. Acta Chimica Slovaca, 11(2): 175—181.

Bakošová M, Mészáros A, Klemeš J, Oravec J (2012) Robust and optimal control approach for exothermic reactor stabilization. Theoretical Foundations of Chemical Engineering, (46): 740—746.

Bakošová M, Oravec J, Mészáros A, Vasičkaninová A (2017) Neural-Network-Based and Robust Model-Based Predictive Control of a Tubular Heat Exchanger. Chemical Engineering Transactions, (61): 301—306.

Bakošová M, Oravec J (2014) Robust mpc of an unstable chemical reactor using the nominal system optimization. Acta Chimica Slovaca, 7(2): 87—93.

Bemporad A, Morari M, Dua V, Pistikopoulos EN (2002) The explicit linear quadratic regulator for constrained systems. Automatica, 38(1): 3—20.

Borrelli F, Bemporad A, Morari M (2017) Predictive Control for Linear and Hybrid Systems. Cambridge University Press.

Fissore D (2008) Robust control in presence of parametric uncertainties: observer-based feedback controller design. Chemical Engineering Science, 63(7): 1890—1900.

Hornik K (1991) Approximation capabilities of multilayer feedforward networks. Neural Networks, 4(2): 251—257.

Karg B, Lucia S (2018) Efficient representation and approximation of model predictive control laws via deep learning.

Klaučo M, Kvasnica M (2019) MPC-Based Reference Governors. Springer, 1st edition.

Lofberg J (2004) YALMIP: A Toolbox for Modeling and Optimization in MATLAB. In Proc. of the CACSD Conference, Taipei, Taiwan. Available from http://users.isy.liu.se/johanl/yalmip/.

Lohr Y, Klaučo M, Kalúz M, Monnigmann M (2019) Mimicking predictive control with neural networks in domestic heating systems. In Fikar M and Kvasnica M, editors, Proceedings of the 22nd International Conference on Process Control, pages 19—24, Šrbské Pleso, Slovakia. Slovak University of Technology in Bratislava, Slovak Chemical Library.

Maciejowski JM (2002) Predictive Control with Constraints. PEARSON Prentice-Hall.

Mayne DQ, Rawlings JB, Rao CV, Scokaert POM (2000) Constrained model predictive control: Stability and optimality. Automatica, 36(6): 789–814.

Pourdehi S, Karimaghaee P (2018) Stability analysis and design of model predictive reset control for nonlinear time-delay systems with application to a two-stage chemical reactor system. Journal of Process Control, 71: 103–115.

Prasath G, Recke B, Chidambaram M, Jørgensen J (2010) Application of Soft Constrained MPC to a Cement Mill Circuit. In Proceedings of the 9th International Symposium on Dynamics and Control of Process Systems, Belgium, Leuven.

Singh A, de Villiers P, Rambalee P, Gous G, de Klerk J, Humphries G (2010) A holistic approach to the application of model predictive control to batch reactors. IFAC Proceedings Volumes, 43(9): 127–132. 13th IFAC Symposium on Automation in Mining, Mineral and Metal Processing.

Smets IY, Claes JE, November EJ, Bastin GP, Impe JFV (2004) Optimal adaptive control of (bio)chemical reactors: past, present and future. Journal of Process Control, 14(7): 795–805. Dynamics, Monitoring, Control and Optimization of Biological Systems.

sciendo

Corrigendum to: Thermal inactivation kinetics of *Aspergillus oryzae* β-galactosidase in concentrated lactose solution

Viera Illeová, Milan Polakovič

Department of Chemical and Biochemical Engineering, Institute of Chemical and Environmental Engineering,
Faculty of Chemical and Food Technology, Slovak University of Technology,
Radlinského 9, 812 37 Bratislava, Slovakia
milan.polakovic@stuba.sk

Corrigendum to: Acta Chimica Slovaca, 11(2): 170—174 (2018). DOI: 10.2478/acs-2018-0024

We would like to amend a mistake in our paper (Illeová and Polakovič, 2018) where wrong graphs were assigned to Figures 1 and 2. Corrected figures and captions are provided below.

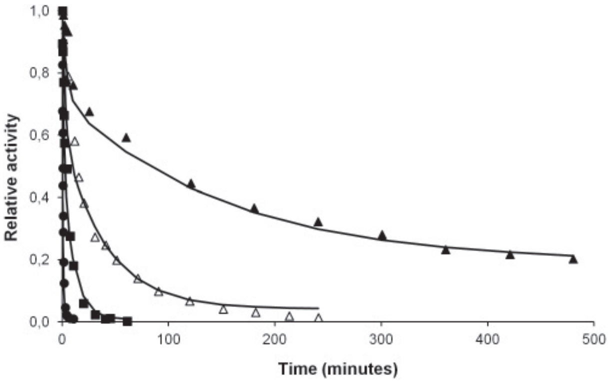

Fig. 1. Thermal inactivation of β-GAL in a reaction medium with the initial lactose concentration of 300 g/L. Symbols represent experimental data at individual temperatures: ● — 75 °C, ■ — 70 °C, △ — 67.5 °C, ▲ — 65 °C. Lines are the fitted activity values using the model specified by Eqs. (1)—(3).

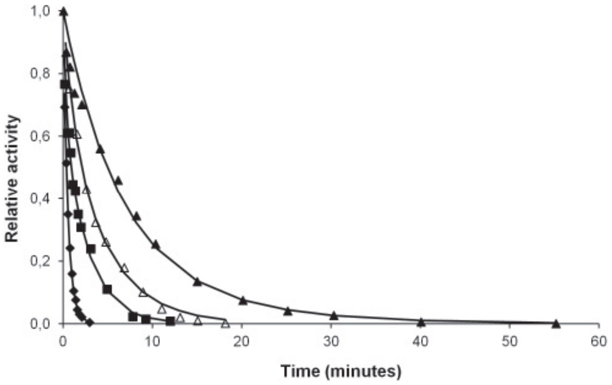

Fig. 2. Thermal inactivation of β-GAL in lactose-free buffer. The meaning of all symbols and lines is the same as in Fig. 1 except for the experimental data at 72.5 °C (♦).

References

Illeová V, Polakovič M (2018) Acta Chim. Slovaca 11(2): 170—174.

sciendo

DFT and *ab initio* calculations of ionization potentials, proton affinities and bond dissociation enthalpies of aromatic compounds

Denisa Cagardová[a], Martin Michalík[a], Erik Klein[a],
Vladimír Lukeš[a], Zoran Marković[b]

[a]*Institute of Physical Chemistry and Chemical Physics, Slovak University of Technology in Bratislava, Radlinského 9, SK-812 37 Bratislava, Slovakia*
[b]*State University of Novi Pazar, Vuka Karadžića bb, 36300 Novi Pazar, Serbia*
denisa.cagardova@stuba.sk

Abstract: Theoretical study of phenol, thiophenol, benzeneselenol, aniline and their *para*-amino and *para*-nitro derivatives is presented. Neutral molecules, their deprotonated forms, neutral radicals, and radical cations were studied using three Density Functional Theory (DFT) functionals as well as combined DFT and *ab initio* G4 method in order to calculate the N—H, O—H, S—H, and Se—H bond dissociation enthalpies (BDE), proton affinities of corresponding anions (PA) and ionization potentials (IP) of studied compounds. These quantities represent fundamental reaction enthalpies related to the radical scavenging action of primary antioxidants. Calculated values were compared with available experimental data to assess applicability of the computational approaches employed. M06-2X/6-311++G(d,p) and G4 methods showed the best agreement with the available experimental gas-phase reaction enthalpies.

Keywords: Antioxidant; radical; anion; electron-donating group; electron-withdrawing group

Introduction

Primary antioxidants represent chemical compounds able to scavenge reactive radical intermediates formed during the oxidative reactions in biological systems, food products, synthetic polymers, and other industrial products. In these processes, hydroxyl ($HO^{\bullet}$), alkoxyl ($RO^{\bullet}$) and peroxyl ($ROO^{\bullet}$) radicals play an important role (Rice-Evans et al., 1996). The primary antioxidants comprise essentially (poly)phenolic compounds and secondary aromatic amines (Wolf and Kaul, 1992). They act usually both through chain transfer and through chain termination (Gugumus, 1990).

Hydrogen atom transfer from the antioxidant molecule is often the first step of radical scavenging by primary antioxidants (Gugumus, 1990). From the thermodynamic point of view, the dissociation of O—H bond in phenols and N—H bond in aromatic amines is described by the bond dissociation enthalpy (BDE)

$$\mathrm{BDE} = H(\mathrm{R}^{\bullet}) + H(\mathrm{H}^{\bullet}) - H(\mathrm{R{-}H}) \qquad (1)$$

where $H(\mathrm{R}^{\bullet})$ is total enthalpy of the formed radical, $H(\mathrm{H}^{\bullet})$ is total enthalpy of the abstracted hydrogen atom, and $H(\mathrm{R{-}H})$ stands for total enthalpy of the molecule. Based on the statistical thermodynamics, total enthalpy (H) at temperature (T) is estimated from the expression

$$H = E_0 + \mathrm{ZPE} + \Delta H_{\mathrm{trans}} + \Delta H_{\mathrm{rot}} + \Delta H_{\mathrm{vib}} + RT \qquad (2)$$

where E_0 is total electronic energy, ZPE denotes the zero-point energy, and $\Delta H_{\mathrm{trans}}$, ΔH_{rot} and ΔH_{vib} are translational, rotational and vibrational contributions to enthalpy, respectively. The last term in Eq. 2 represents PV-work converting energy to enthalpy (Atkins, 1998). Proton affinity (PA) of formed anion represents the reaction enthalpy of molecule deprotonation, i.e. of the heterolytic cleavage of the corresponding bond

$$\mathrm{PA} = H(\mathrm{R}^{-}) + H(\mathrm{H}^{+}) - H(\mathrm{R{-}H}) \qquad (3)$$

where $H(\mathrm{R}^{-})$ is enthalpy of anion and $H(\mathrm{H}^{+})$ is total enthalpy of proton. Another important quantity related to the antioxidant action is the adiabatic ionization potential, IP

$$\mathrm{IP} = H(\mathrm{R{-}H}^{\bullet+}) + H(\mathrm{e}^{-}) - H(\mathrm{R{-}H}) \qquad (4)$$

where $H(\mathrm{R{-}H}^{\bullet+})$ is total enthalpy of the radical cation, and $H(\mathrm{e}^{-})$ is enthalpy of an electron, 3.145 kJ mol^{-1} (Bartmess, 1994). Proton affinity and ionization potential are reaction enthalpies of the first steps in the Sequential Proton-Loss — Electron Transfer (SPLET) and Single-Electron Transfer — Proton Transfer (SET-PT) mechanisms, respectively (Filipović, 2020; Galano and Raúl Alvarez-Idaboy, 2019; Leopoldini et al., 2011).

Experimentally determined BDE, PA and IP values can be obtained using several techniques (Bordwell and Cheng, 1991; Dos Santos and Simoes, 1998; Fujio et al., 1981; Jonsson et al., 1994; Kim et al., 2000; McMahon and Kebarle, 1977; Mulder et al., 2005): electrochemistry, photoacoustic calorimetry, mass spectrometry, photoelectron spectroscopy, etc. BDE measurements are often carried out in solution-phase (e.g. in water, DMSO, benzene, etc.) and gas-phase values are subsequently estimated based on certain assumptions. Therefore, published experimental BDEs may vary in a wide range. For example, published experimental works suggested the gas-phase O—H BDE of phenol to be in the range from 348.5 kJ mol^{-1} to 375.0 kJ mol^{-1} (Dos Santos and Simoes, 1998). In this review, the authors recommend the value of 371.3 ± 2.3 kJ mol^{-1} for the gas-phase O—H BDE of phenol. Using the mass-analyzed threshold ionization technique and literature data, Kim et al. (2000) experimentally determined O—H BDE to be 381 kJ mol^{-1}. Later, Angel and Ervin (2004) used mass spectrometry (threshold collision-induced dissociation method) determining the value of 359 ± 8 kJ mol^{-1}. Mulder et al. (2005) recommended the experimental gas-phase value of 362 ± 3 kJ mol^{-1} using two gas-phase and three solution-phase values.

Accurate estimation of thermochemistry data from quantum chemical calculations is also a challenging task since the employment of high levels of calculations is necessary to consider the effect of both dynamical and non-dynamical parts of the electron correlation. Thirty years ago, semiempirical methods were intensively used due to the very restricted computational resources. Dewar's MNDO (Dewar and Thiel, 1977) and AM1 (Dewar et al., 1985) methods have been widely employed for enthalpies of formation as well as reaction enthalpies of organic compounds calculations. The latest re-parametrized MNDO method, called PM7 method (Stewart, 2013), represents a computationally simple and fast tool for basic thermodynamic characterization of organic compounds. Currently, density functional theory (DFT) calculations are most frequently used due to the lower computational costs in comparison to the *ab initio* methods. Sensitivity of the results to suitable functional and basis set selection represents a disadvantage of the DFT calculations. An alternative, and generally more accurate, computational approach for the thermochemistry data is based on the Gaussian-*n* (G*n*) theories, which employ a set of calculations of different levels of accuracy and various basis sets to obtain exact energetics (Curtiss et al., 2007). In the G1, G2 and G3 approaches, high level correlation calculations, e.g. QCISD(T) and CCSD(T), with moderate size basis set are combined with energies from lower level calculations, e.g. MP4 and MP2, with larger basis sets to approximate the energies of more expensive calculations (Curtiss et al., 1991 and 1998). In addition, several molecule-independent empirical parameters, higher level correction terms, are included to estimate the remaining deficiencies assuming that they are systematic (Curtiss et al., 2007). The use of geometries and zero-point energies from the density functional theory, application of CCSD(T) energies, inclusion of the *ab initio* Hartree-Fock limit energy and the addition of higher-level correction parameters in the G4 method (Curtiss and Redfern, 2007) contribute to the largest improvement over the original G*n* theories. The G4 theory is a useful tool which may provide benchmark quality results (Curtiss et al., 2007).

Basis sets used in the field of theoretical investigation of thermochemistry and reaction kinetics have to reliably describe all relevant species, i.e. molecules, radicals, deprotonated species and radical cations resulting from electron abstraction. Moreover, the basis set should provide reliable description of intramolecular hydrogen bonds that are very frequent mainly in various (poly)phenolic compounds. Pople's basis sets are somewhat outdated as correlation-consistent or polarization-consistent basis sets typically yield better results with similar resources. Some Pople's basis sets show deficiencies that can lead to incorrect results (Moran et al., 2006). For balanced description of investigated species it is necessary to include both diffusion and polarization functions. Among widely used basis sets count also those developed by Dunning and coworkers (Dunning, 1989) for converging Post-Hartree-Fock calculations enabling extrapolation of results to complete basis sets. The added diffuse functions improve the description of anions and long-range interactions such as van der Waals forces and electric field properties. Because of the rigorous construction of these basis sets, extrapolation can be done for almost any energetic property at the *ab initio* level of theory. The Sapporo basis sets are compact segmented basis sets designed to efficiently recover the correlation energy of a system. These basis sets were based on the original NOSeC-*n*ZP sets (*n* = D, T, Q) (Noro et al., 1997) designed to represent the space spanned by atomic natural orbitals as determined by configuration interaction calculations. The *n*ZP sets are based on the primitive sets of Huzinaga and Klobukowski (1993) which were extended by adding higher angular momentum functions for the determination of a set of accurate natural orbitals (Weber et al., 2015). The def2-TZVP basis sets are very appealing because they provide consistent accuracy across the whole periodic table and they are available for all elements up to radon (*Z* = 86) (Weigend and Ahlrichs, 2005), contrary to more commonly used basis sets from the Pople and Dunning groups. These

Karlsruhe basis sets are very appealing because they constitute balanced and economical basis sets of graded quality from partially polarized double zeta to heavily polarized quadruple zeta for all elements up to radon ($Z = 86$). The extension consists of adding a minimal set of diffuse functions to a subset of elements. The minimally augmented (ma) basis set triple zeta is recommended for general-purpose applications of the density functional theory (Zheng et al., 2011).

In this contribution, comparative G4 and DFT investigation of gas-phase BDEs, PAs and IPs of phenol, thiophenol, benzeneselenol and aniline and their two *para*-substituted derivatives (Fig. 1) was performed. The NH_2 substituent is a strong electron-donating group while the NO_2 group is a strong electron-withdrawing group. *Para*-substituted compounds represent a suitable set of model compounds, where the steric effects of a substituent do not influence the studied group homolytic and heterocyclic dissociations. DFT data were calculated using the most frequently employed functionals, i.e. B3LYP, M06-2X, and PBE0, in combination with various basis sets. B3LYP hybrid functional represents the most popular functional for BDE, IP, and PA calculations. The newer M06-2X functional was optimized for the calculations of thermochemistry and kinetics and it should overcome the known imperfections of B3LYP. PBE0 functional belongs to the generalized gradient approximation functionals and is quite popular as it usually provides reliable results. The obtained theoretical results were compared also with calculated semiempirical PM7 data and available experimental values.

The Pople's basis set 6-311++G(d,p) provides reliable molecular geometries and reaction enthalpies for phenols and anilines (Poliak and Vagánek, 2013; Klein and Lukeš, 2006; Škorňa et al., 2016) and it is still widely employed in antioxidant action thermochemistry calculations. The remaining basis sets employed have comparable size but different origins.

Computational details

Quantum chemical calculations were performed using the Gaussian 16 program package (Frisch et al., 2016). M06-2X (Zhao and Truhlar, 2008), B3LYP (Becke's three parameter Lee—Yang—Parr) (Lee et al., 1988; Becke, 1988) and PBE0 (Adamo and Barone, 1999) functionals were employed. The energy cut-off was 10^{-5} kJ mol^{-1} and the final RMS energy gradient was below 0.01 kJ mol^{-1} A^{-1}. For all calculations, 6-311++G(d,p) (Hariharan and Pople, 1973; Rassolov et al., 1998), aug-cc-pVTZ (Kendall et al., 1992; Woon and Dunning, 1993), ma-def2-TZVP (Weigend and Ahlrichs, 2005) and Sapporo (Noro et al., 1997) basis sets were used. Frequency analysis confirmed that the found species are in real energy minima (no imaginary frequencies). All thermodynamic quantities were evaluated for the temperature of 298.15 K. The total gas-phase enthalpies of the hydrogen atom are –1301.81 kJ mol^{-1} for M06-2X, –1324.87 kJ mol^{-1} for B3LYP, and –1324.87 kJ mol^{-1} for the PBE0 functional. In case of the PM7 method, formation enthalpy of the hydrogen atom is –1324.87 kJ mol^{-1} and proton formation enthalpy is 1536.2 kJ mol^{-1} (Atkins, 1998). The G4 enthalpy of hydrogen atom is –1310.3 kJ mol^{-1}. Gas-phase proton and electron total enthalpies are 6.197 kJ mol^{-1} and 3.145 kJ mol^{-1}, respectively. In case of M06-2X calculations, the starting geometries were taken from optimized B3LYP method because of convergence problems with the starting geometries pre-optimized by molecular mechanics.

Results and Discussion

The first part of discussion is focused on the description of optimal geometries of the studied molecules with planar aromatic ring. As it is shown in Fig. 1, φ (φ') represent dihedral angles between hydrogen atom(s) of the functional group, heteroatom and two carbon atoms of the benzene ring. The parent phenol and thiophenol molecules exhibit planar gas-phase geometries due to the planar arrangement of —OH and —SH groups (see Tab. 1). In case of benzeneselenol, —SeH group is twisted only for B3LYP/6-311++G(d,p) with the dihedral angle of 35°. Hydrogen atoms of the —NH_2 group in aniline are uniformly tilted from the ring plane and its plane of symmetry is perpendicular to the molecular aromatic plane (see Fig. 2a). DFT methods predict the values of dihedral angles, φ and φ', to be between ±24° to ±27°. PM7 geometry of aniline is more planar, i.e. φ and φ' reach ±17°. The electron donating amino group leads to perpendicular arrangement of —SH and —SeH groups (see Fig. 2a). On the other hand, the hydroxyl group of substituted phenol is planar and the absolute values of selected dihedral angles for both amino groups in *para*-aminoaniline are slightly higher, by about 3°, in comparison to those for aniline (Tab. 2). In general, radical formation after homolytic O—H, S—H, Se—H and N—H bond cleavage mostly decreases the absolute values of the dihedral angle. Small changes in planarity were observed for *para*-aminobenzeneselenol. The presence of a nitro group in the *para* position is responsible for molecules' planarity (Tab. 3). In case of *para*-nitroaniline, DFT values of dihedral angles φ and φ' lie between ±17° to ±21°. Semiempirical PM7 geometries are planar.

Electron abstraction from parent molecules and *para*-amino derivatives (Tab. 4) planarizes molecular geometry. Significant changes in the structure were observed for anions formed from *para*-aminophenol and aniline when compared to parent molecules. The aromatic ring plane represents the mirror plane of the amino group (see Fig. 2b). For *para*-aminothiophenol and *para*-aminobenzeneselenol, DFT dihedral angle φ and φ' values are in the range from ±30° to ±31°. Here, the mirror plane of the amino group is perpendicularly oriented towards the ring plane. Identical situation was found for electroneutral *para*-amino derivatives (e.g. Fig. 2a).

NO_2 group in the radical cation of *para*-nitrophenol is slightly rotated with respect to the aromatic ring (see Fig. 2c). The maximal dihedral angles, $\Theta = \Theta'$, were found for B3LYP and PBE0 functionals (from 41° to 46°, see Tab. 5), while M06-2X dihedral angles are lower by approximately one half. In case of the remaining nitro derivatives, M06-2X optimal geometries are mostly planar. The anionic forms are planar for PM7 method as well as for all tested DFT functionals.

Tab. 6 summarizes the computed gas-phase O—H, S—H, Se—H and N—H bond dissociation enthalpies. For example, found BDE values of phenol are in the range from 347 kJ mol^{-1} to 352 kJ mol^{-1} for B3LYP, from 370 kJ mol^{-1} to 375 kJ mol^{-1} for M06-2X and from 347 kJ mol^{-1} to 350 kJ mol^{-1} for PBE0. Among all DFT results, M06-2X/6-311++G(d,p) value of 370 kJ mol^{-1} is in best accordance with the last recommended gas-phase value of 362.8 ± 2.9 kJ mol^{-1} (Mulder et al., 2005). G4 BDE = 367 kJ mol^{-1} is closest to the recommended value while PM7 BDE = 313 kJ mol^{-1} is significantly underestimated. Similar trends were obtained also for the remaining non-substituted molecules. However, for aniline, M06-2X/6-311++G(d,p) N—H BDE is closer to experimental data than the G4 one. Nevertheless, the minimal effect of a basis set for individual DFT functionals was found for the largest benzeneselenol molecule (Tab. 6a).

Compared to non-substituted molecules, electron-donating substituents decrease the studied BDEs, whereas electron-withdrawing groups induce an increase in BDE (Tab. 6b, c). In case of nitro-derivatives of thiophenol and benzeneselenol, the DFT functionals predicted negligible substituent effect for all basis sets. Maximum differences in BDE, compared with non-substituted molecules, were 1 kJ mol^{-1}. The reference G4 method gave larger energy differences (up to 6 kJ mol^{-1}).

Electron abstraction from an electroneutral molecule is an endothermic process and the found adiabatic ionization potentials are compiled in Tab. 7. These represent typical values for organic molecules with one aromatic ring. Comparing the few available experimental data, B3LYP and PBE0 functionals tend to underestimate IPs. On the other hand, the M06-2X functional gave reasonable results for all used basis sets. Like BDEs, electron-donating groups induce a drop in IP and electron-withdrawing groups induce a rise in IP.

Gas-phase proton affinities (Eq. 3) are substantially higher than BDEs, i.e. heterolytic cleavage of O—H, S—H, Se—H and N—H bonds in the gas-phase is not energetically favored. Available experimental data were obtained from various mass spectrometry experiments; however, they (Tab. 8) are very scarce. Within the group of non-substituted studied molecules containing chalcogenes, proton affinities are decreasing from phenol to benzeneselenol. In case of aniline, PA is the highest one (e.g. for B3LYP/6-311++G(d,p), PA(aniline) = 1534 kJ mol^{-1}). For all computational approaches, PA of aniline is roughly by 80 kJ mol^{-1} higher than that of phenol. Results in Tab. 8 also show that the PM7 method underestimates PAs which is surprising because PM3 method gives PAs of thiophenols in very good agreement with those of the B3LYP/6-311++G(d,p) method (Pankratov and Shalabai, 2004; Rimarčík et al., 2011).

Electron-donating NH_2 group located in the para position causes a slight increase in PA, whereas electron-withdrawing NO_2 group is responsible for significant drop in PA. DFT methods show ca 100 kJ mol^{-1} decrease in case of phenols and anilines. In thiophenols and benzeneselenols, drop in PA reaches ca 80 kJ mol^{-1}. The G4 method predicts lower differences between non-substituted molecules and *para*-nitro derivatives.

Conclusions

In this article, theoretical study of phenol, thiophenol, benzeneselenol, aniline and their *para*-nitro and *para*-amino derivatives is presented. Structures of the investigated molecules, corresponding radical cations, anions and radicals were studied using DFT functionals, *ab initio* G4 and semiempirical PM7 quantum chemical methods. The obtained total enthalpies enabled calculations of N—H, O—H, S—H and Se—H bond dissociation enthalpies, proton affinities, and ionization potentials which belong to the most important thermodynamic characteristics of antioxidants. Calculated quantities were compared with available experimental values to ascertain the suitability of the used approaches. The best agreement with the experimental values was obtained for M06-2X/6-311++G(d,p) and *ab initio* G4 methods. For phenols, excellent mutual agreement between M06-2X/6-311++G(d,p) and B3LYP/6-311++G(d,p) proton affinities was also found. Semiempirical PM7 method, providing most planar structures of the studied species, tends to underestimate the investigated quantities with exception of ionization potentials, which are overestimated.

Acknowledgment
This work was supported by the Slovak Research and Development Agency under the contract no. SK-SRB-18-0016. We are grateful to the HPC center at the Slovak University of Technology in Bratislava, which is a part of the Slovak Infrastructure of High Performance Computing (SIVVP project, ITMS code 26230120002, funded by the European region development funds, ERDF) for the computational time and resources made available. V.L. and E.K. thank the Ministry of Education, Science, Research and Sport of the Slovak Republic for funding within the scheme "Excellent research teams". D.C. would like to thank for support from the STU Grant scheme for Support of Young Researchers (1619).

References

Adamo C, Barone V (1999) J. Chem. Phys. 110: 6158–6169.
Angel LA, Ervin KM (2004) J. Phys. Chem. A 108: 8346–8352.
Atkins PW (1998) Physical Chemistry, 6th ed., Oxford University Press, Oxford.
Bartmess JE (1994) J. Phys. Chem. 98: 6420–6424.
Bartmess JE, Scott JA, McIver RT Jr (1979) J. Am. Chem. Soc. 101: 6046–6056.
Becke AD (1988) Phys. Rev. A 38: 3098–3100.
Bordwell FG, Cheng J-P (1991) J. Am. Chem. Soc. 113: 1736–1743.
Bordwell FG, Zhang X-M, Cheng J-P (1993) J. Org. Chem. 58: 6410–6414.
Bordwell FG, Zhang X-M, Satish AV, Cheng J-P (1994) J. Am. Chem. Soc. 116: 6605–6610.
Curtiss LA, Raghavachari K, Redfern PC, Rassolov V, Pople JA (1998) J. Chem. Phys. 109: 7764–7776.
Curtiss LA, Raghavachari K, Trucks GW, Pople JA (1991) J. Chem. Phys. 94: 7221–7230.
Curtiss LA, Redfern PC, Raghavachari K (2007) J. Chem. Phys. 126: 084108.
Denisov ET (1995) Polym. Degrad. Stab. 49: 71–75.
Dewar MJS, Thiel W (1977) J. Am. Chem. Soc. 99: 4899–4907.
Dewar MJS, Zoebisch EG, Healy EF, Stewart JJP (1985) J. Am. Chem. Soc. 107: 3902–3909.
Dos Santos RMB, Muralha VSF, Correia CF, Guedes RC, Cabral BJC, Simoes JAM (2002) J. Phys. Chem. A 106: 9883–9889.
Dos Santos RMB, Simoes JAM (1998) J. Phys. Chem. Ref. Data 27: 707–739.
Dunning TH (1989) J. Chem. Phys. 90: 1007–1023.
Faulk JD, Dunbar RC, Lifshitz C (1990) J. Am. Chem. Soc. 112: 7893–7899.
Filipović, N. (2020) Computational Modeling in Bioengineering and Bioinformatics, Academic Press, pp. 211–256. ISBN 978-0-12-819583-3.
Frisch MJ, Trucks GW, Schlegel HB, Scuseria GE, Robb MA, Cheeseman JR, Scalmani G, Barone V, Petersson GA, Nakatsuji H, Li X, Caricato M, Marenich AV, Bloino J, Janesko BG, Gomperts R, Mennucci B, Hratchian HP, Ortiz JV, Izmaylov AF, Sonnenberg JL, Williams-Young D, Ding F, Lipparini F, Egidi F, Goings J, Peng B, Petrone A, Henderson T, Ranasinghe D, Zakrzewski VG, Gao J, Rega N, Zheng G, Liang W, Hada M, Ehara M, Toyota K, Fukuda R, Hasegawa J, Ishida M, Nakajima T, Honda Y, Kitao O, Nakai H, Vreven T, Throssell K, Montgomery JA Jr., Peralta JE, Ogliaro F, Bearpark MJ, Heyd JJ, Brothers EN, Kudin KN, Staroverov VN, Keith TA, Kobayashi R, Normand J, Raghavachari K, Rendell AP, Burant JC, Iyengar SS, Tomasi J, Cossi M, Millam JM, Klene M, Adamo C, Cammi R, Ochterski JW, Martin RL, Morokuma K, Farkas O, Foresman JB, Fox DJ (2016) Gaussian 16, Revision B.01, Gaussian, Inc., Wallingford CT.
Fujio M, McIver RT, Taft RW (1981) J. Am. Chem. Soc. 103: 4017–4029.
Galano A, Raúl Alvarez-Idaboy J (2019) Int. J. Quant. Chem. 119: e25665.
Gugumus F (1990) Oxidation inhibition in organic materials, 1, CRC Press, Boca Raton.
Hariharan PC, Pople JA (1973) Theor. Chim. Acta 28: 213–222.
Huzinaga S, Klobukowski M (1993) Chem. Phys. Lett. 212: 260.
Jonsson M, Lind J, Eriksen TE, Merenyi G (1994) J. Am. Chem. Soc. 116: 1423–1427.
Kendall RA., Dunning Jr. TH, Harrison RJ (1992) J. Chem. Phys. 96: 6796–806.
Kim HT, Green RJ, Qian J, Anderson SL (2000) J. Chem. Phys. 112: 5717–5721.
Klein E, Lukeš V (2006) Chem. Phys. 330: 515–525.
Kobayashi T, Nagakura S (1975) J. Electron. Spectrosc. Relat. Phenom. 6: 421–427.
Lee C, Yang W, Parr RG (1988) Phys. Rev. B 37: 785–789.
Leeck DT, Li R, Chyall LJ, Kenttämaa HI (1996) J. Phys. Chem. 100: 6608–6611.
Leopoldini M, Russo N, Toscano M (2011) Food Chemistry 125: 288–306.
Lind J, Shen X, Eriksen TE, Merenyi G (1990) J. Am. Chem. Soc. 112: 479–482.
Lipert RJ, Colson SD (1990) J. Chem. Phys. 92: 3240–3241.
Luo YR (2007) Comprehensive Handbook of Chemical Bond Energies, CRC Press, Boca Raton, New York.
Mandado M, Graña AM, Mosquera RA (2004) Chem. Phys. Lett. 400: 169–174.
McMahon TB, Kebarle P (1977) J. Am. Chem. Soc. 99: 2222–2230.
Moran D, Simmonett AC, Leach, FE III, Allen WD, Schleyer, PvR, Schaefer, HF (2006) J. Am. Chem. Soc. 128: 9342–9343.
Mulder P, Korth HG, Pratt DA, DiLabio GA, Valgimigli L, Pedulli GF, Ingold KU (2005) J. Phys. Chem. A 109: 2647–2655.
Newcomb M, Manek MB, Glenn AG (1991) J. Am. Chem. Soc. 113: 949–958.
Noro T, Sekiya M, Koga T (1997) Theor. Chem. Acc. 98: 25–32.
Poliak P, Vagánek A (2013) Acta Chimica Slovaca 6: 64–72.

Potapov VK, Kardash IE, Sorokin VV, Sokolov SA, Evlasheva TI (1972) Khim. Vys. Energ. 6: 392.

Pankratov AN, Shalabai AV (2004). J. Struct. Chem. 45: 756–761.

Rassolov V, Pople JA, Ratner M, Windus TL (1998) J. Chem. Phys. 109: 1223–1229.

Rice-Evans CA, Miller NJ, Paganga G (1996) Free Radical Biology and Medicine 20: 933–956.

Rimarčík J, Lukeš V, Klein E, Rottmannová L (2011) Comp. Theor. Chem. 967: 273–283.

Stewart JJP (2013) J. Mol. Model. 19: 1–32.

Škorňa P, Rimarčík J, Poliak P, Lukeš V, Klein E (2016) Comput. Theor. Chem. 1077: 32–38.

Taft R, Bordwell FG (1988) Acc. Chem. Res. 21: 463–469.

Takahashi M, Ozeki H, Kimura K (1992) J. Chem. Phys. 96: 6399–6406.

Venimadhavan S, Amarnath K, Harvey NG, Cheng J-P, Arnett GM (1992) J. Am. Chem. Soc. 114: 221–229.

Wayner DDM, Lusztyk E, Pagé D, Ingold KU, Mulder P, Laarhoven LJJ, Aldrich HS (1995) J. Am. Chem. Soc. 117: 8737–8744.

Weber R, Hovda B, Schoendorff G, Wilson AK (2015). Chem. Phys. Lett. 637: 120–126.

Weigend F, Ahlrichs R (2005) Phys Chem Chem Phys 7: 3297–3305.

Wolf R, Kaul BL (1992) Plastics, Additives. Ullmann's encyclopedia of industrial chemistry, Weinheim: VCH.

Woon DE and Dunning Jr. TH (1993) J. Chem. Phys. 1358–1371.

Wren SW, Vogelhuber KM, Ichino T, Stanton JF, Lineberger WC (2012) J. Phys. Chem. A 116: 3118–3123.

Wright JS, Johnson ER, DiLabio GA (2001) J. Am. Chem. Soc. 123: 1173–1183.

Zhao Y, Truhlar DG (2008) Theor. Chem. Acc. 120: 215–241.

Zheng J, XU X, Truhlar DG (2011) Theor. Chem. Acc. 128: 295–305.

Zhu Q, Zhang XM, Fry AJ (1997) Polym. Degrad. Stab. 57: 43–50.

Tab. 1. Dihedral angles φ (and φ' in aniline, where $\varphi = -\varphi$') in degrees for optimal geometries of electroneutral state of molecules and radicals. Values for radicals are in italics.

Method	Basis set	O—H	S—H	Se—H	N—H
B3LYP	6-311++G(d,p)	0	0	35	±24
		–	*–*	*–*	*0*
	aug-cc-pVTZ	0	0	0	±24
		–	*–*	*–*	*0*
	Sapporo	0	0	0	±24
		–	*–*	*–*	*0*
	ma-TZVP	0	0	0	±24
		–	*–*	*–*	*0*
M06-2X	6-311++G(d,p)	0	4	0	±25
		–	*–*	*–*	*0*
	aug-cc-pVTZ	0	1	0	±25
		–	*–*	*–*	*0*
	Sapporo	0	1	4	±25
		–	*–*	*–*	*0*
	ma-TZVP	0	0	0	±25
		–	*–*	*–*	*0*
PBE0	6-311++G(d,p)	0	0	0	±25
		–	*–*	*–*	*0*
	aug-cc-pVTZ	0	0	0	±24
		–	*–*	*–*	*0*
	Sapporo	0	0	0	±27
		–	*–*	*–*	*0*
	ma-TZVP	0	0	0	±24
		–	*–*	*–*	*0*
PM7		0	0	0	±17
		–	*–*	*–*	*0*
G4		0	0	0	±26
		–	*–*	*–*	*0*

Tab. 2. Dihedral angles φ (and φ' in aniline, where $\varphi = -\varphi$') / Θ, Θ' ($\Theta = -\Theta$' for all cases) in degrees for *para*-amino substituted neutral molecules and radicals. Values for radicals are in italics.

Method	Basis set	O—H / NH$_2$	S—H / NH$_2$	Se—H / NH$_2$	N—H / NH$_2$
B3LYP	6-311++G(d,p)	0 / ±27 *– / ±13*	92 / ±23 *– / ±15*	91 / ±23 *– / ±17*	±27 / ±27 *0 / ±19*
	aug-cc-pVTZ	0 / ±26 *– / ±12*	91 / ±23 *– / ±15*	91 / ±23 *– / ±16*	±27 / ±27 *0 / ±19*
	Sapporo	0 / ±26 *– / ±11*	91 / ±22 *– / ±14*	91 / ±23 *– / ±16*	±27 / ±27 *0 / ±18*
	ma-TZVP	1 / ±26 *– / ±12*	91 / ±22 *– / ±14*	91 / ±22 *– / ±15*	±27 / ±27 *0 / ±18*
M06-2X	6-311++G(d,p)	1 / ±27 *– / ±11*	89 / ±24 *– / ±15*	91 / ±24 *– / ±26*	±28 / ±28 *0 / ±19*
	aug-cc-pVTZ	0 / ±27 *– / ±11*	89 / ±24 *– / ±15*	89 / ±24 *– / ±25*	±28 / ±28 *0 / ±18*
	Sapporo	0 / ±27 *– / ±9*	89 / ±23 *– / ±13*	94 / ±23 *– / ±25*	±27 / ±27 *0 / ±18*
	ma-TZVP	0 / ±27 *– / ±9*	93 / ±23 *– / ±13*	89 / ±23 *– / ±25*	±27 / ±27 *0 / ±17*
PBE0	6-311++G(d,p)	0 / ±27 *– / ±13*	92 / ±23 *– / ±15*	91 / ±23 *– / ±25*	±27 / ±27 *0 / ±20*
	aug-cc-pVTZ	0 / ±27 *– / ±13*	91 / ±23 *– / ±15*	91 / ±23 *– / ±17*	±27 / ±27 *0 / ±19*
	Sapporo	0 / ±27 *– / ±12*	91 / ±23 *– / ±14*	91 / ±23 *– / ±25*	±27 / ±27 *0 / ±19*
	ma-TZVP	1 / ±26 *– / ±12*	92 / ±22 *– / ±14*	91 / ±22 *– / ±24*	±27 / ±27 *0 / ±19*
PM7		1 / 22 *– / 0*	91 / ±10 *– / ±15*	91 / ±14 *– / ±4*	±23 / ±23 *0 / ±8*
G4		0 / ±28 *– / ±17*	91 / ±25 *– / ±17*	91 / ±25 *– / ±18*	±29 / ±29 *0 / ±22*

Tab. 3. Dihedral angles φ (and φ’ in aniline, where $\varphi = -\varphi$’) / Θ, Θ’ ($\Theta = -\Theta$’ for all cases), in degrees for *para*-nitro substituted neutral molecules and radicals. Values for radicals are in italics.

Method	Basis set	O—H / NO_2	S—H / NO_2	Se—H / NO_2	N—H / NO_2
B3LYP	6-311++G(d,p)	0 / 0	0 / 0	0 / 0	±18 / 0
		– / 0	– / 0	– / 0	0 / 0
	aug-cc-pVTZ	0 / 0	0 / 0	0 / 0	±18 / 0
		– / 0	– / 0	– / 0	0 / 0
	Sapporo	0 / 0	0 / 0	0 / 0	±17 / 0
		– / 0	– / 0	– / 0	0 / 0
	ma-TZVP	0 / 0	0 / 0	0 / 0	±17 / 0
		– / 0	– / 0	– / 0	0 / 0
M06-2X	6-311++G(d,p)	0 / 0	2 / 0	0 / 0	±20 / 0
		– / 0	– / 0	– / 0	0 / 0
	aug-cc-pVTZ	0 / 0	0 / 0	2 / 0	±19 / 0
		– / 0	– / 0	– / 0	0 / 0
	Sapporo	0 / 0	0 / 0	3 / 0	±19 / 0
		– / 0	– / 0	– / 0	0 / 0
	ma-TZVP	0 / 0	0 / 0	3 / 0	±19 / 0
		– / 0	– / 0	– / 0	0 / 0
PBE0	6-311++G(d,p)	0 / 0	0 / 0	0 / 0	±18 / 0
		– / 0	– / 0	– / 0	0 / 0
	aug-cc-pVTZ	0 / 0	0 / 0	0 / 0	±18 / 0
		– / 0	– / 0	– / 0	0 / 0
	Sapporo	0 / 0	0 / 0	0 / 0	±17 / 0
		– / 0	– / 0	– / 0	0 / 0
	ma-TZVP	0 / 0	0 / 0	0 / 0	±19 / 0
		– / 0	– / 0	– / 0	0 / 0
PM7		0 / 0	0 / 0	0 / 0	0 / 0
		– / 0	– / 0	– / 0	0 / 0
G4		0 / 0	0 / 0	0 / 0	±21 / 0
		– / 0	– / 0	– / 0	0 / 0

Tab. 4. Dihedral angles φ (and φ' in aniline, where $\varphi = -\varphi'$) / Θ, Θ' ($\Theta = -\Theta'$ in degrees for radical cations and anions (in italics) formed from *para*-amino substituted molecules.

Method	Basis set	O—H / NH_2	S—H / NH_2	Se—H / NH_2	N—H / NH_2
B3LYP	6-311++G(d,p)	0 / 0 – / 59, 121	0 / 0 – / ±31	0 / 0 – / ±31	0 / 0 0 / -60, -120
	aug-cc-pVTZ	0 / 0 – / 42, 104	0 / 0 – / ±31	0 / 0 – / ±30	0 / 0 0 / -59, -121
	Sapporo	0 / 0 – / 81, 143	0 / 0 – / ±31	0 / 0 – / ±30	0 / 0 0 / -59, -121
	ma-TZVP	0 / 0 – / 59, 121	0 / 0 – / ±31	0 / 0 – / ±30	0 / 0 0 / -60, -120
M06-2X	6-311++G(d,p)	0 / 0 – / 59, 121	0 / 0 – / ±31	91 / 0 – / ±31	0 / 0 0 / -59, -121
	aug-cc-pVTZ	0 / 0 – / 59, 121	0 / 0 – / ±31	91 / 0 – / ±31	0 / 0 0 / -59, -121
	Sapporo	0 / 0 – / 59, 121	0 / 0 – / ±31	91 / 0 – / ±30	0 / 0 0 / -59, -121
	ma-TZVP	0 / 0 – / 59, 121	0 / 0 – / ±31	91 / 0 – / ±30	0 / 0 0 / -59, -121
PBE0	6-311++G(d,p)	0 / 0 – / 59, 121	0 / 0 – / ±31	0 / 0 – / ±31	0 / 0 0 / -59, -121
	aug-cc-pVTZ	0 / 0 – / 94, 31	0 / 0 – / ±31	0 / 0 – / ±31	0 / 0 0 / -59, -121
	Sapporo	0 / 0 – / 88, 150	0 / 0 – / ±31	0 / 0 – / ±30	0 / 0 0 / -59, -121
	ma-TZVP	0 / 0 – / 59, 121	0 / 0 – / ±31	0 / 0 – / ±30	0 / 0 0 / -59, -121
PM7		0 / 0 – / ±31	0 / 0 – / ±28	0 / 0 – / ±26	0 / 0 0 / -59, -121
G4		0 / 0 – / -92, 25	0 / 0 – / ±33	0 / 0 – / 32	0 / 0 0 / -57, -123

Tab. 5. Dihedral angles φ (and φ' in aniline, where $\varphi = -\varphi$') / Θ, Θ' ($\Theta = -\Theta$' for all cases) in degrees for radical cations and anions (in italics) formed from *para*-nitro substituted molecules.

Method	Basis set	O—H / NO_2	S—H / NO_2	Se—H / NO_2	N—H / NO_2
B3LYP	6-311++G(d,p)	0 / 46	0 / –37	–1 / 32	0 / –33
		– / 0	– / 0	– / 0	0 / 0
	aug-cc-pVTZ	0 / 44	1 / –34	–1 / 28	0 / –29
		– / 0	– / 0	– / 0	0 / 0
	Sapporo	0 / 45	1 / –34	0 / 39	0 / 30
		– / 0	– / 0	– / 0	0 / 0
	ma-TZVP	0 / 45	1 / –36	–1 / 30	0 / 31
		– / 0	– / 0	– / 0	0 / 0
M06-2X	6-311++G(d,p)	0 / 25	0 / –12	0 / 0	0 / 11
		– / 0	– / 0	– / 0	0 / 0
	aug-cc-pVTZ	0 / 12	0 / 0	0 / 0	0 / 0
		– / 0	– / 0	– / 0	0 / 0
	Sapporo	0 / 13	0 / 0	0 / 0	0 / 0
		– / 0	– / 0	– / 0	0 / 0
	ma-TZVP	0 / 20	0 / 0	0 / 0	0 / 0
		– / 0	– / 0	– / 0	0 / 0
PBE0	6-311++G(d,p)	0 / 43	0 / –32	0 / 24	0 / –27
		– / 0	– / 0	– / 0	0 / 0
	aug-cc-pVTZ	0 / 40	1 / –27	0 / 0	0 / 22
		– / 0	– / 0	– / 0	0 / 0
	Sapporo	0 / 41	1 / –27	0 / 17	0 / 22
		– / 0	– / 0	– / 0	0 / 0
	ma-TZVP	0 / 41	0 / –29	–1 / 21	0 / 25
		– / 0	– / 0	– / 0	0 / 0
PM7		0 / 0	0 / 0	0 / 0	0 / 0
		– / 0	– / 0	– / 0	0 / 0
G4		0 / 38	–1 / 30	–1 / 24	0 / 0
		– / 0	– / 0	– / 0	0 / 0

Tab. 6a. Bond dissociation enthalpies (in kJ mol^{-1}) of non-substituted molecules.

Method	Basis set	Phenol O—H	Thiophenol S—H	Benzeneselenol Se—H	Aniline N—H
B3LYP	6-311++G(d,p)	346.9	355.7	325.5	368.2
	aug-cc-pVTZ	351.3	358.3	326.8	370.4
	Sapporo	352.0	360.7	327.3	370.9
	ma-TZVP	347.4	358.8	326.0	368.6
M06-2X	6-311++G(d,p)	369.7	358.6	312.0	386.5
	aug-cc-pVTZ	374.6	364.7	312.9	389.2
	Sapporo	374.9	366.7	312.4	389.5
	ma-TZVP	371.8	362.5	313.6	388.6
PBE0	6-311++G(d,p)	348.4	353.3	321.9	368.8
	aug-cc-pVTZ	353.2	355.3	322.5	370.8
	Sapporo	353.8	357.6	323.0	371.3
	ma-TZVP	349.5	356.0	321.9	369.2
PM7		312.7	329.6	308.5	328.6
G4		367.4	335.3	306.7	381.6
Experiment		368 (isobutane)[a] 372 (benzene)[a] 376[b], 379[c] 367[d],369[e]	332[b,l] 331.0[j] 349.4[k]	280.3[f] 326.4±16.7[g]	386[c,h] 373[i]

Tab. 6b. Bond dissociation enthalpies (in kJ mol^{-1}) of *para*-amino derivatives.

Method	Basis set	O—H	S—H	Se—H	N—H
B3LYP	6-311++G(d,p)	310.4	295.7	281.6	343.4
	aug-cc-pVTZ	314.8	299.4	283.5	345.1
	Sapporo	315.2	301.7	284.0	345.5
	ma-TZVP	310.5	299.4	282.4	343.1
M06-2X	6-311++G(d,p)	332.0	308.8	318.6	361.4
	aug-cc-pVTZ	336.6	313.2	317.4	363.3
	Sapporo	336.4	314.8	316.6	363.4
	ma-TZVP	332.8	312.7	318.5	362.2
PBE0	6-311++G(d,p)	312.2	295.5	327.7	344.3
	aug-cc-pVTZ	317.1	299.2	281.9	345.9
	Sapporo	317.4	301.5	327.0	346.2
	ma-TZVP	312.9	299.5	326.4	344.0
PM7		282.7	330.5	299.8	306.1
G4		333.8	316.6	294.2	359.7
Experiment		316[m]			360[i]

Tab. 6c. Bond dissociation enthalpies (in kJ mol^{-1}) of *para*-nitro derivatives.

Method	Basis set	O—H	S—H	Se—H	N—H
B3LYP	6-311++G(d,p)	364.5	355.8	325.7	385.8
	aug-cc-pVTZ	368.5	358.5	326.9	387.4
	Sapporo	369.1	360.8	327.4	388.0
	ma-TZVP	364.8	359.1	326.2	386.1
M06-2X	6-311++G(d,p)	387.4	359.4	312.8	403.3
	aug-cc-pVTZ	392.0	362.8	313.4	405.3
	Sapporo	392.2	364.7	312.8	405.7
	ma-TZVP	389.2	363.3	314.0	404.8
PBE0	6-311++G(d,p)	366.2	353.7	322.2	386.7
	aug-cc-pVTZ	370.4	355.5	322.7	387.8
	Sapporo	371.0	357.8	323.1	388.4
	ma-TZVP	366.9	356.4	322.1	386.6
PM7		329.2	321.4	317.7	350.6
G4		378.9	342.8	312.9	416.1
Experiment		393[m]	340.6[b,j]		405[c,h]

[a]Wayner et al., 1995; [b]Bordwell and Cheng, 1991; [c]Zhu et al., 1997; [d]Denisov, 1995; [e]Lind et al., 1990; [f]Newcomb et al., 1991; [g]Leeck et al., 1996; [h]Bordwell et al., 1993; [i]Jonsson et al., 1994; [j]Bordwell et al., 1994; [k]Dos Santos et al., 2002; [l]Venimadhavan et al., 1992; [m]Luo, 2007.

Tab. 7a. Ionization potentials (in kJ mol^{-1}) of non-substituted molecules.

Method	Basis set	Phenol	Thiophenol	Benzeneselenol	Aniline
B3LYP	6-311++G(d,p)	807.1	786.2	775.1	731.3
	aug-cc-pVTZ	804.2	784.4	774.0	730.2
	Sapporo	804.9	783.7	774.5	730.5
	ma-TZVP	804.0	783.0	774.0	729.5
M06-2X	6-311++G(d,p)	824.4	806.7	798.9	748.7
	aug-cc-pVTZ	822.1	807.9	795.8	748.6
	Sapporo	822.1	806.7	794.4	748.1
	ma-TZVP	820.5	803.0	794.9	746.4
PBE0	6-311++G(d,p)	805.4	786.8	774.8	729.1
	aug-cc-pVTZ	802.1	784.4	773.5	727.8
	Sapporo	802.8	783.7	774.0	728.1
	ma-TZVP	802.1	783.1	773.5	727.2
PM7		831.2	790.8	756.2	748.2
G4		825.7	810.7	799.6	750.0
Experiment		821[a]	801[b]		745[c]

Tab. 7b. Ionization potentials (in kJ mol^{-1}) of *para*-amino derivatives.

Method	Basis set	Phenol	Thiophenol	Benzeneselenol	Aniline
B3LYP	6-311++G(d,p)	685.6	687.6	685.7	632.3
	aug-cc-pVTZ	682.8	684.1	683.0	630.4
	Sapporo	683.1	683.6	683.1	630.7
	ma-TZVP	681.8	682.7	682.5	629.1
M06-2X	6-311++G(d,p)	702.7	708.5	831.6	649.4
	aug-cc-pVTZ	700.8	704.9	825.8	648.3
	Sapporo	700.5	703.7	824.0	648.0
	ma-TZVP	698.3	702.5	826.2	645.6
PBE0	6-311++G(d,p)	682.7	686.7	685.1	629.6
	aug-cc-pVTZ	679.3	682.7	681.9	627.4
	Sapporo	679.6	682.2	682.1	627.6
	ma-TZVP	678.5	681.5	681.7	626.3
PM7		719.7	721.1	705.8	665.4
G4		704.6	705.1	708.4	653.1

Tab. 7c. Ionization potentials (in kJ mol^{-1}) of *para*-nitro derivatives.

Method	Basis set	Phenol	Thiophenol	Benzeneselenol	Aniline
B3LYP	6-311++G(d,p)	879.6	853.2	839.1	807.9
	aug-cc-pVTZ	873.8	848.5	835.3	803.6
	Sapporo	874.3	847.7	835.8	804.1
	ma-TZVP	873.7	847.5	835.5	803.6
M06-2X	6-311++G(d,p)	906.8	877.8	863.0	828.2
	aug-cc-pVTZ	901.1	873.1	857.0	824.6
	Sapporo	900.9	871.8	855.4	824.4
	ma-TZVP	899.8	871.2	856.7	823.3
PBE0	6-311++G(d,p)	879.2	854.1	838.5	805.8
	aug-cc-pVTZ	872.9	848.4	834.2	800.8
	Sapporo	873.4	847.8	834.7	801.2
	ma-TZVP	873.1	847.7	834.7	801.1
PM7		906.2	847.9	955.9	824.5
G4		890.9	868.6	853.8	837.1
Experiment		905[d]			805[e]

[a] Lipert and Colson, 1990; [b] Faulk et al., 1990; [c] Takahashi et al., 1992; [d] Kobayashi and Nagakura, 1975; [e] Potapov et al., 1972.

Tab. 8a. Proton affinities (in kJ mol^{-1}) of non-substituted molecules.

Method	Basis set	Phenol	Thiophenol	Benzeneselenol	Aniline
		O—H	S—H	Se—H	N—H
B3LYP	6-311++G(d,p)	1450.1	1412.1	1392.9	1533.6
	aug-cc-pVTZ	1456.9	1419.5	1397.7	1537.0
	Sapporo	1457.4	1422.5	1398.6	1537.4
	ma-TZVP	1452.7	1419.7	1396.1	1535.5
M06-2X	6-311++G(d,p)	1452.9	1403.1	1377.2	1530.7
	aug-cc-pVTZ	1457.1	1413.6	1384.1	1531.9
	Sapporo	1457.6	1415.9	1386.3	1532.5
	ma-TZVP	1455.8	1411.6	1382.3	1533.1
PBE0	6-311++G(d,p)	1454.5	1413.2	1393.6	1538.2
	aug-cc-pVTZ	1461.7	1420.4	1398.2	1541.4
	Sapporo	1462.2	1423.5	1399.1	1541.8
	ma-TZVP	1457.7	1420.8	1396.7	1540.0
PM7		1390.4	1366.3	1347.5	1461.3
G4		1461.3	1421.0	1394.0	1537.8
Experiment		1461[a] 1450[b] 1462[c]	1424[d]		1541[e] 1533[c]

Tab. 8b. Proton affinities (in kJ mol^{-1}) of *para*-amino derivatives.

Method	Basis set	O—H	S—H	Se—H	N—H
B3LYP	6-311++G(d,p)	1466.9	1432.2	1412.9	1549.6
	aug-cc-pVTZ	1475.1	1437.9	1416.5	1553.7
	Sapporo	1457.4	1422.5	1398.6	1537.4
	ma-TZVP	1452.7	1419.7	1396.1	1535.5
M06-2X	6-311++G(d,p)	1467.8	1421.9	1396.8	1545.4
	aug-cc-pVTZ	1474.1	1428.2	1401.8	1548.2
	Sapporo	1474.9	1430.8	1403.9	1549.0
	ma-TZVP	1472.6	1429.7	1400.8	1549.0
PBE0	6-311++G(d,p)	1472.2	1433.5	1414.6	1555.3
	aug-cc-pVTZ	1481.0	1439.5	1417.7	1559.5
	Sapporo	1481.7	1442.9	1418.7	1560.1
	ma-TZVP	1477.5	1440.9	1417.1	1558.5
PM7		1401.4	1381.0	1357.7	1469.6
G4		1476.6	1436.3	1409.5	1552.4
Experiment		1470[a]			

Tab. 8c. Proton affinities (in kJ mol^{-1}) of *para*-nitro derivatives.

Method	Basis set	O—H	S—H	Se—H	N—H
B3LYP	6-311++G(d,p)	1347.2	1328.1	1314.9	1424.0
	aug-cc-pVTZ	1356.1	1337.6	1321.9	1429.6
	Sapporo	1356.6	1340.4	1322.9	1430.1
	ma-TZVP	1351.8	1337.6	1320.3	1428.1
M06-2X	6-311++G(d,p)	1354.3	1326.6	1307.9	1425.8
	aug-cc-pVTZ	1360.4	1336.1	1316.3	1428.9
	Sapporo	1361.3	1338.5	1318.7	1430.1
	ma-TZVP	1359.2	1336.9	1314.9	1430.3
PBE0	6-311++G(d,p)	1354.6	1331.9	1318.6	1431.9
	aug-cc-pVTZ	1364.0	1341.7	1325.5	1437.5
	Sapporo	1364.5	1344.5	1326.5	1438.0
	ma-TZVP	1359.7	1341.7	1323.9	1436.0
PM7		1281.7	1291.7	1290.7	1355.7
G4		1372.4	1353.0	1333.5	1463.6
Experiment		1372[a] 1342[b]	1342[b]		

[a]Fujio et al., 1981; [b]McMahon and Kebarle, 1977; [c]Bartmess et al., 1979; [d]Taft and Bordwell, 1988; [e]Wren et al., 2012.

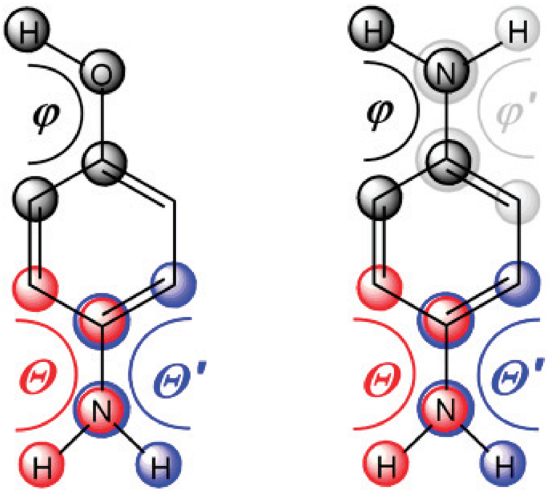

Fig. 1. Notation of dihedral angles Θ/Θ' and φ/φ' in *para*-aminophenol and *para*-aminoaniline molecules. Notation is valid for all studied molecules.

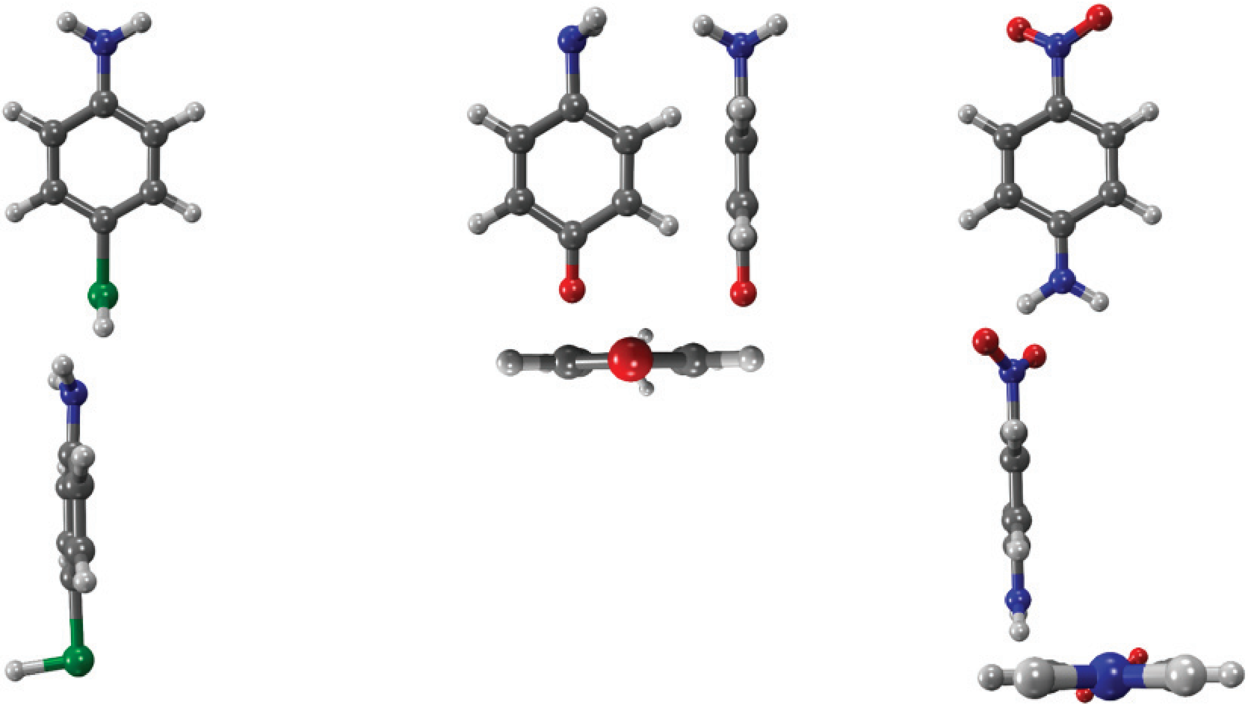

a) b) c)

Fig. 2. Selected optimal B3LYP/6-311++G(d,p) geometries of *para*-aminobenzeneselenol with mirror plane of amino group perpendicular to the benzene ring plane (hydrogens of amino group are tilted from the ring plane) and twisted —SeH group (a), deprotonated *para*-aminophenol with mirror plane of amino group corresponding to the ring plane (b) and *para*-nitroaniline with rotated nitro group (c).